BIODEGRADABLE POLY(HYDROXY BUTYRATE-CO-VALERATE) NANOCOMPOSITES AND BLENDS WITH POLY (BUTYLENE ADIPATE CO-TEREPHTHALATE) FOR SENSOR APPLICATIONS

Shailesh Vidhate, B.E., M.S.

Dissertation Prepared for the Degree of

DOCTOR OF PHILOSOPHY

UNIVERSITY OF NORTH TEXAS

December 2011

APPROVED:

Nandika D'Souza, Major Advisor
Vijay Vaidyanathan, Committee Member
Witold Brostow, Committee Member
Nigel Shepherd, Committee Member
Mohamed El Bouanani, Committee Member
Narendra Dahotre, Chair of the Department of Materials Science and Engineering
Costas Tsatsoulis, Dean of the College of Engineering
James D. Meernik, Acting Dean of the Toulouse Graduate School

Vidhate, Shailesh. Biodegradable Poly(Hydroxy Butyrate-Co-Valerate) Nanocomposites and Blends with Poly(Butylene Adipate-Co-Terephthalate) for Sensor Applications. Doctor of Philosophy (Materials Science and Engineering), December 2011, 197 pp., 69 figures, 19 tables, chapter references.

The utilization of biodegradable polymers is critical for developing “cradle to cradle” mindset with ecological, social and economic consequences. Poly(hydroxy butyrate-co-valerate) (PHBV) shows significant potential for many applications with a polypropylene equivalent mechanical performance. However, it has limitations including high crystallinity, brittleness, small processing window, etc. which need to be overcome before converting them into useful products. Further the development of biodegradable strain sensing polymer sensors for structural health monitoring has been a growing need. In this dissertation we utilize carbon nanotubes as a self sensing dispersed nanofiller. The impact of its addition on PHBV and a blend of PHBV with poly(butylene adipate-co-terephthalate) (PBAT) polymer was examined. Nanocomposites and blends of PHBV, PBAT, and MWCNTs were prepared by melt-blending. The effect of MWCNTs on PHBV crystallinity, crystalline phase, quasi-static and dynamic mechanical property was studied concurrently with piezoresistive response. In PHBV/PBAT blends a rare phenomenon of melting point elevation by the addition of low melting point PBAT was observed. The blends of these two semicrystalline aliphatic and aromatic polyesters were investigated by using differential scanning calorimetry, small angle X-ray scattering, dynamic mechanical analysis, surface energy measurement by contact angle method, polarized optical and scanning electron microscopy, and rheology. The study revealed a transition of immiscible blend compositions to miscible blend compositions

across the 0-100 composition range. PHBV10, 20, and 30 were determined to be miscible blends based on a single T_g and rheological properties. The inter-relation between stress, strain, morphological structure and piezoresistive response of MWCNT filled PHBV and PHBV/PBAT blend system was thoroughly investigated. The outcomes of piezoreistivity study indicated MWCNT filled PHBV and PHBV/PBAT blend system as a viable technology for structural health monitoring. Finally, the compostability of pure polymer, blend system, and MWCNT filled system was studied indicating that PBAT and CNT decreased the biodegradability of PHBV with CNT being a better contributor than PBAT.

Copyright 2011

by

Shailesh Vidhate

ACKNOWLEDGEMENTS

I would like to express my heartfelt gratitude to my major advisor Prof. Nandika D'Souza for accepting me to conduct research in her lab and for her continual guidance, support and encouragement throughout my doctoral program without which this dissertation would not have been possible.

I would like to thank Prof. Vijay Vaidyanathan for his guidance as a committee member. Advice from my committee members Prof. Whitold Brostow, Prof. Nigel Shepherd, and Prof. Mohamed El Bouanani is highly appreciated.

I am grateful to all the help rendered by Sandeep Manandhar and Mangesh Nar whenever I needed. A special thanks to Koffi Dagnon, Ali Shaito, and Mark Pickens for training me on PMRL lab equipments and their frequent guidance. Thanks to Dr. David Diercks, Dr. Nancy Bunce, and Dr. David Garrett of UNT-CART for giving me equipments training and generous assistance in the use of CART equipments. I would like to thank the members of MTSE departmental staff: Joan Jolly, Wendy Agnes, April Porter, and John Sawyer.

I am grateful to all the help and support rendered by Tea Datashvili, Mohammad Maneshian, Sunny Ogbomo, Emmanuel Ogunsona, Dong Le, Dinesh Ramesh and all the students and staffs of Materials Science and Engineering for the good times together.

I am forever indebted to my parents Pandit Vidhate and Padma Vidhate; and my fiancée Gauri Khandekar for their care and support in every aspect of my life.

TABLE OF CONTENTS

LIST OF TABLES

LIST OF FIGURES

CHAPTER 1

DISSERTATION SCOPE AND BACKGROUND

1.1 Introduction

Polymeric materials are now used in all sectors of life as very durable products with tailor-made properties. For thousands of years humans have used natural polymers, such as cotton, jute, silk, wool, etc. provided by plants and animals. In the modern era, due to increased application and population growth, natural polymers have been replaced by cheaply available petroleum based synthetic polymers. During the past decade the intense use of modern plastics, combined with their enormous stability, has created serious problems with plastic waste. The growing awareness about finite petroleum resources, non degradability, and hazardous environmental effects of petroleum based polymers has led to new environmentally friendly biodegradable polymers based on renewable resources.

Today, biopolymers are being used in various applications such as bio-medical therapeutic aids [1], food products [2], packaging [3], coatings [4], commodity applications [5], etc. However, the range of biopolymer applications is still limited due to their weak mechanical properties, thermal stability, slow crystallization rate and low gas barrier properties and high sensitivity to environment variables such as temperature and humidity. The use of biopolymers is limited due to availability of cheap petroleum based polymers. There is a therefore a critical need to evaluate and improve the properties of the biopolymers to make them fully competitive with common non-degradable thermoplastics [6]. The properties of these polymers should be retained during their use and should be able to decompose after their utilization. In this dissertation two main

approaches have been studied to improve the properties of biopolymers: 1) nanocomposites by dispersion of nanoparticles into the host matrix and 2) making blends with other suitable biodegradable polymer.

Nanocomposites not only give the advantage of thermal and mechanical performance but also impart multifunctional properties [7]. Similarly material properties and their behavior can be changed significantly by making polymer blends. In general biopolymer blends and nanocomposites show remarkable mechanical and thermal properties with the advantage of biocompatibility, biodegradability and, in some cases, functional properties provided by either the renewable component or the inorganic moieties blended in.

1.2 Objective

To establish the viability of carbon nanotube dispersed multi-functional, biodegradable PHBV and PHBV/PBAT blend system as piezoresponsive materials for potential use in structural health monitoring.

In pursuing the desired goal PHBV nanocomposites and PHBV/PBAT blends containing multi walled carbon nanotubes (MWCNTs) were studied in this dissertation. The experimental research work and the dissertation were carried out and organized in the following way:

Modification of PHBV by carbon nanotubes

- Review of polymer carbon nanotube nanocomposites
- Study of thermal, mechanical, morphological, and electrical properties of PHBV/CNT nanocomposites.
- Piezoresponsive properties of PHBV modified by carbon notubes

Modification of PHBV by PBAT

- Review of crystalline-crystalline blends
- PHBV/PBAT crystalline/crystalline polymer blend miscibility
- PHBV/PBAT:, mechanical and rheological properties
- CNT filled PHBV/PBAT blends' piezoresistive response in optimum concentration

Finally, both modifiers were investigated for variation in biodegradation potential through a biodegradation study of PHBV, PHBV/PBAT blend, and CNT filled PHBV/PBAT blend. Since the discovery of CNTs by Ijiima in 1991, CNTs have attracted much more attention of researchers due to their unique structural and extraordinary physical properties. These nanoparticles can be effectively utilized to make multifunctional polymer nanocomposites by using various processing techniques. Chapter 2 provides an overview of polymer/CNT nanocomposites, methods to produce nanocomposites, properties of carbon nano structures, and how they impart multifunctionality.

PHBV is a natural biopolymer which is has a high crystallinity and slow crystallization rate. Resultsexplaining the CNTs performance as a nucleating agent, increasing crystallization rate, and reinforcing the PHBV matrix are presented in Chapter 3. Correlation between microstructure and physical properties are conducted using transmission electron microscopy (TEM) of PHBV/CNT nanocomposites.

Chapter 4 describes the piezoresistive response of PHBV/CNT nanocomposites under transient, quasi-static, and cyclic loading. PHBV has good strength but is very brittle and has a small processing window. To solve these problems PHBV/PBAT blends were prepared. PHBV and PBAT are crystalline polymers. The PHBV/PBAT

blends study provides an opportunity to investigate crystalline/crystalline polymer blends which is a less investigated area in polymer blends. This is done in Chapter 5 which contains a detailed literature review of crystalline/crystalline polymer blends. . The wide range of research on PHBV/PBAT blends and the corresponding results of thermal and morphological studies are presented in detail in Chapter 6. Mechanical, dynamic mechanical analysis, and rheological properties of the blends are affected by miscibility behavior of the blends. These are presented in Chapter 7.

After PHBV/PBAT blends research work, PHBV:PBAT 70:30 weight ratio composition was chosen to make composites with CNTs since they were a miscible composition. The piezoresistive and morphological properties of these compositions are described in Chapter 8 keeping a focus on structural health monitoring. Finally, the degradation study of base PHBV, PHBV/PBAT blend and CNT filled PHBV/PBAT blend compositions was done. The biodegradability of plastics provides these materials with novel and additional properties which is also beneficial after their use. The details of this study are presented in Chapter 9. Finally, the summary of conclusions on biodegradable, piezoresistive, and modified polymeric system is presented in Chapter 10.

1.3 References

[1] Hule R, Pochan DJ. MRS Bulletin 2007;32:354.

[2] Heertjef I, Roijers EC, and Hendrickx HA. Lebensmittel-Wissenschaft und-Technologie 1998;31(4):387-396.

[3] Davisa G, SongIndustrial JH. Crops and Products 2006;23(2):147-161.

[4] Schmalzinga D, Christine A. Piggeea CA, Frantisek Foret F, Emanuel Carrilho E, Karger BL. Journal of Chromatography 1993;652(1):149-159.

[5] Gross RA, Kalra B. Science 2002;297(5582):803-807.

[6] Bordes P, Pollet E, Av**é**rous L. Progress in Polym Sci 2009;34:125.

[7] Tuteja A, Duxbury PM, Mackay ME. Macromolecules 2007;40 (26):9427–9434.

CHAPTER 2

POLYMER/CARBON NANOPARTICLE NANOCOMPOSITES

2.1 Introduction

Today, due to increased concern about environmental safety and growing market opportunities, biodegradable polymers have been receiving more attention from scientific and industrial communities. Among various biodegradable polymers, aliphatic polyesters are an important group of biodegradable polymers. Few examples of polymers from this group are: poly(butylene succinate) [1], poly(butylene succinate adipate) copolyester [2], poly(L-lactide) [3], and bacterial poly(3-hydroxybutyric acid) (PHB) [4] and its copolyesters. These polymers show good physical properties and are successfully commercialized by various manufacturers under various trade names [5]. Polyhydroxy alkonates (PHAs) is one of the families of biodegradable polymers which can be obtained from a variety of microorganisms. PHAs get synthesized inside the cells of microorganisms as carbon and energy storage. In controlled conditions of the laboratory, microorganisms can accumulate 70-80% P(3HB) of their cellular dry weight. Among the PHA family, (PHB) is the most studied polymer. The Ralstonia eutropha (formerly Alcaligenes eutrophus) bacteria acting as a bioplastic factory, can produce PHB from glucose up to an efficient yield of 85% by dry weight. Figure 2.1 shows a transmission electron microscopy (TEM) image of an ultrathin section of Azotobacter chroococcum cell containing PHB biopolymer. The resultant PHB has very high steriochemical purity. All the chiral centers in the linear chains possess the R-steriochemical configuration making PHB highly crystalline and therefore highly brittle [6]. PHB possesses a high melting temperatures (170-175 ^{o}C) and thermal degradation

takes place near the melting temperature. This poor processability and high brittleness limits application viability. To resolve this limitation, many researchers developed copolymers of PHB with monomeric units like (R) 3-HB (hydroxyl butyrate), (R)-HV (hydroxyl valerate).

Poly(3- hydroxybutyrate-co-3-hydroxyvalerate) (PHBV)

In the mid 1980s, Imperial Chemical Industries discovered the copolymer PHBV by adding propionate to the fermentation broth. In 1985, ICI first commercialized P(3HB-co-3HV) containing 0-30 mol% of 3HV with the brand name BIOPOL. They realized that the addition of few molar mass of 3-hydroxyvalerate units into the main chain of PHB improved the flexibility of the polymer [7, 8]. Thereafter, PHBV became an attractive biopolymer for research [9-11]. Unfortunately, PHBV still presents some problems to be solved, which are: slow crystallization rate, relatively difficult processing due to low melt viscosity and small processing window, low elongation at break, brittleness, and very high crystallinity [12]. The high brittleness in the PHBV was thought to arise from the large spherulites associated with the crystallization of PHBV. Since the spherulite size is determined by the rate of spherulitic growth and nucleation efficiency, the brittleness in PHBV can be avoided by controlling the crystallization mechanism. Ultimately, blending PHBV with another suitable polymer could be an efficient approach to modify the spherulite structure and change crystallization of PHBV.

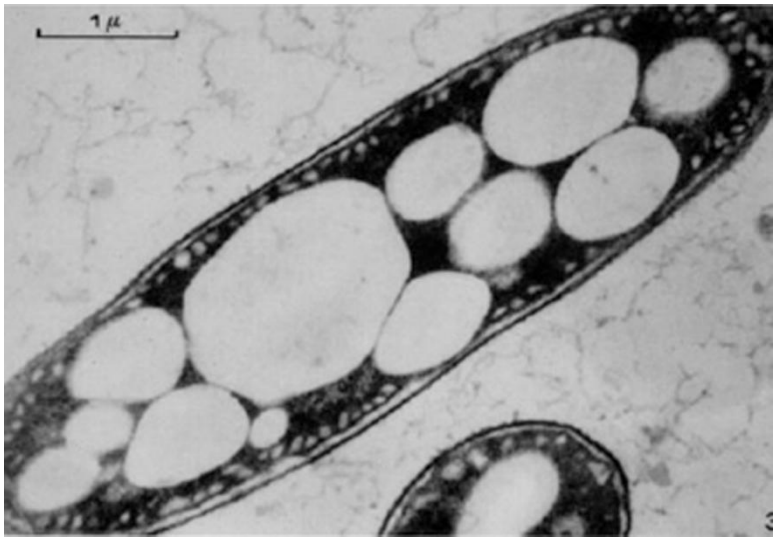

Figure 2.1 TEM of ultrathin section of Azotobactor cell containing PHB biopolymer [13]

As a biobased polyester, PHBV is made by bacteria and can be digested by bacteria and utterly decompose to carbon dioxide, water and biomass in soil or under composting condition. PHBV is also a kind of material with high biological compatibility and is a great barrier to water, gas, and aroma. Tianan PHBV is produced by non-modified bacteria (Ralstonia Entropha) by the fermentation of glucose obtained from non GMO corn starch. This polymer is fully biodegradable in the soil, water, and under standard composting conditions. The physical properties of PHBV are given in Table 2.1.

Table 2.1 Material properties of PHBV

Properties	Test methods	Results
Density, g/cm^3		1.25
Yielding stress*, MPa	ASTM D638	33
Tensile strength, MPa	ASTM D638	33
Elongation at break, %	ASTM D638	15
Tensile modulus, MPa	ASTM D638	1400
Flexural strength, MPa	ASTM D790	61.4
Flexural modulus, MPa	ASTM D790	1400
Impact strenght ,k J/m^2		9.27
Izod impact strength, J/m	GB1843-89	25
Vicat-Temperature, ℃	ASTM	142.9
MFI, g/10 min (2.16Kg,173℃)		3.7
Melting temperature, ℃	DSC	174.5
Crystallization temperature,℃	DSC	108.9
Degree of crystallinity, %	DSC	46
Color		White

*Material properties are adopted from supplier's website

Poly(butylene adipate-co-terephthalate) (PBAT)

The introduction of terephthalate units into the main chains of aliphatic polyesters can improve the physical as well as biodegradable properties of the polymer [13]. It is well known that aromatic polyesters like poly(ethylene terephthalate), poly(propylene terephthalate), poly(butylene terephthalate), etc. generally show better thermal and mechanical properties than aliphatic polyesters. PBAT is one of such aromatic polyester that show excellent thermal and mechanical properties with the added advantage of biocompatibility and biodegradability. PBAT has high flexibility (elongation at break 700%), good mechanical strength, and processability. So to improve the properties of PHBV and to retain biodegradablity, making blends of PHBV and PBAT becomes the

best possible choice. The chemical structure and thermal transition temperatures of these two polymers is shown in Figure 2.2.

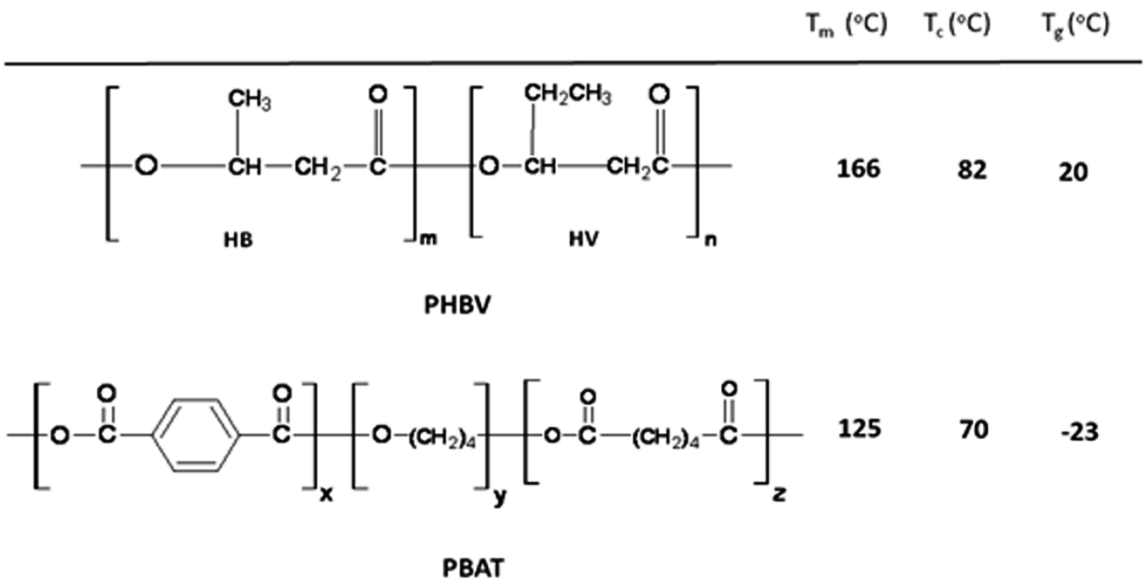

Figure 2.2 Chemical structures and thermal transition temperature of crystalline PHBV and PBAT polymers

PBAT,available under the trade name of Ecoflex® F BX 7011 was supplied by BASF. Ecoflex® is an aliphatic-aromatic copolyester based on terephthalic acid, adipic acid, 1,4- butanediol and modular units. This copolyester contains 44 mol% of BT. The product properties of Ecoflex® are designed to meet the requirements of a biodegradable plastic: ideally, a combination of processability, utilization properties, and biodegrabability. This is achieved by the synthesis of tailor-made molecular structures obtained through modular units by which the statistical copolyester units, including 1,4-butanediol and the dicarbonic acids, adipic acid, and terephthalic acid are linked (Figure 2.2). This modular system involves the incorporation of hydrophilic components of monomers with branching, leading to chain-lengthening, and thereby increasing the molecular weight to yield tailor-made

products with totally different material properties. The properties of the PBAT are summarized in Table 2.2.

Table 2.2 Material prosperities of PBAT*

Property	Unit	Test Method	PBAT Ecoflex®
Mass density	g cm^{-3}	ISO 1183	1.25-1.27
Melt flow rate	mL 10 min^{-1}	ISO 1184	8-Mar
T_m	^oC	DSC	110-115
T_g	^oC	DSC	-30
Shore D hardness	…..	ISO 868	32
Vicat VST A/50	^oC	ISO 869	80
Light Transmittance	%	D-1003	82
Tensile Strength	N/mm^2	ISO 527	34
Ultimate Strength	N/mm^2	ISO 527	34
Failure Energy (Dyna-Test)	J/mm	DIN 53373	24
Ultimate Elongation	%	ISO 527	560
Ultimate Elongation	%	ISO 527	700
Oxygen Permeation Rate	cc/(m2d*bar)	DIN 53380	1,600
Water Permeation Rate	cc/(m2d*bar)	DIN 53122	140

*Material properties are adopted from supplier's website

2.2 Nanocomposites

Nanotechnology is now recognized as one of the most promising technologies of the 21st century. Among various materials research, polymer nanocomposites emerges as a multidisciplinary research activity. Results obtained through the research of polymer nanocomposites can broaden the applications of polymers to a great extent. Multifunctional advanced polymeric nanocomposites can be used for a wide variety of applications in various fields.

Polymer nanocomposites, a multiphase solid material where one of the phases is less than 100 nm in size, are becoming popular. They are increasingly being

manufactured commercially for various applications. In the last twenty five years there has been intensive research on polymer nanocomposites. Simultaneously, growth in computer simulation techniques, scanning electron, and transmission electron microscopy has made the characterization and prediction of the polymer nanocomposites' properties easier. In addition, nanocomposites can be processed using conventional processing techniques and does not need any special or costly processing techniques. Today various types of nanomaterials with various shapes and sizes are being used to prepare polymer nanocomposites. The nanofillers can be in the form of nanoparticles (e.g. carbon, metal powder), nanoplateletes (e.g. silicates), nanowires (e.g. carbon nanotubes, ceramic nanowires), fullerences (e.g. C_{60}), etc. To fulfill the objective of this research, carbon nanotubes were used as nanofillers to make nanocomposites with PHBV polymer. The details about various carbon nanoparticles are discussed in this chapter.

2.2.3 How Nanocomposites Work?

Transition of fillers from macro size to nano size drastically increases the surface area per unit volume of the particles and also causes change in their physical properties [14]. Small size of particles provides large interfacial area between particles and host material. Nanofillers provide higher reinforcing efficiency due to their high aspect ratio. In general, shape and size of the particles have direct effect on properties of the prepared nanocomposites. Along with the individual properties of the host material and fillers, interfacial region shared by both the components affect nanocomposite's properties. Other factors like aspect ratio of the nanoparticles, filler dispersion in the matrix, physical or chemical interaction of nanoparticles with host material affect

properties of nanocomposits. In the early 1990s, Toyota Central R&D Laboratories in Japan pioneered the work on nanocomposites showing considerable improvement in thermal and mechanical properties of Nylon-6 nanocomposite made by addition of small amount of nano fillers [15]. Since then polymer nanocomposites research became a commercially and scientifically attractive topic all over the world.

2.2.4 How to Produce Nanocomposites?

Polymer nanocomposites can be produced using various techniques. The goal of any processing technique to produce nanocomposites, is achieving the maximum possible dispersion of nanofillers in the polymer matrix. Techniques to produce nanocomposites are discussed below.

Melt Mixing

Since the utilization of nanocomposites the melt mixing technique is highly attractive owing to its simplicity [16, 17]. This technique has been widely studied and well explored with polymer clay systems and the generated knowledge with this system can be easily translated for other nanofillers. In this technique the thermoplastic polymer and nanofillers are mixed using conventional melt mixing methods such as extrusion, batch mixing, or injection molding. No solvent is required in this technique and fillers are mixed in the molten matrix using high shear forces. The viscosity of the melt plays an important role in shear mixing of the nanofillers in the polymer melt during processing [18-20]. Compatibilizers can also be used to improve the interfacial adhesion between polymer and fillers. However, organic surface modifications are prone to thermal damage and optimum processing conditions need to be selected. Increased mixing time can improve the dispersion of nanofillers in polymer but long processing time can

degrade the heat sensitive polymers. Elongational flow and orientation of extrudate during extrusion leads to orientation of fillers in the direction of extrusion. Alarge amount of polymer composites can be processed compared to other techniques. Achieving complete exfoliation or dispersion of nanofillers in a polymer matrix with this technique is difficult.

In Situ Polymerization

In this technique a monomer is dissolved or suspended in solvent [21-23]. The nano particles are dispersed or swelled in liquid monomer by ultra sonication or vigorous mechanical stirring. The low viscosity of the monomer improves the dispersion of the nanofillers. The combined solution of monomer and fillers is then polymerized using an initiator at elevated temperature or using radiation. Subsequent polymerization of the monomer leads to uniform intercalation or dispersion of fillers in the polymer matrix. This method is common for thermoset resins as non reacted liquid resin can be crosslinked in between the dispersed nanofillers [24]. This approach has also been successfully used for thermoplastics like nylon [25], polystyrene (PS) [26], poly methyl methacrylate (PMMA) [27], etc. Ogbomo et al. [28] polymerized layered double hydroxide (LDH) dispersed styrene monomer by using a free radical polymerization method with benzoyl peroxide as an initiator to make PS/LDH nanocomposite.

Solution Technique

In this technique the polymer is dissolved in a suitable solvent [29, 30]. Nanofillers which tend to form stacked structures or agglomerates can also be dispersed in the same solvent using sonication or mechanical stirring. The polymer chains get adsorbed on the filler surface or get trapped between nanofillers. When the

solvent is evaporated, the remaining polymer and nanofillers form a nanocomposite. Removal of the solvent is a critical issue in this approach.

2.3 Polymer Carbon Nanoparticle Composites.

Iijima discovered carbon nanotubes in 1991 [31, 32] and after that significant efforts have been made to incorporate carbon nanotubes in various materials. Carbon nanotubes have high aspect ratio, high modulus, and strength and therefore they are promising fillers in polymer composites. Significant enhancement in the tensile modulus and tensile strength has been reported. The estimated mechanical properties of carbon nanotubes are higher than the real values but still represent high potential filler materials for polymer nanocomposites.

The glass transition temperature and thermal degradation temperature is also observed to significantly increase by the addition of carbon nanofillers in polymers. The addition of carbon nanotubes in polymers can impart improved electrical and thermal conductivity [33-41]. Many potential applications have been proposed for carbon nanotubes and carbon nanotubes based systems, including high strength conductive composites, sensors, thermal conductors, energy storage, semiconductor devices and probes, etc.

2.4 Carbon in Various Forms

The structure and properties of various forms of carbon are completely different. Carbon forms various structures like graphite, diamond, carbon fibers, carbon black, bucky balls (C_{60}), carbon nanofibers, carbon nanotubes, etc. In the experimental work of this thesis carbon nanotubes as conductive fillers are used.

2.4.1 Carbon Nanofibers

Carbon nanofibers and carbon nanotubes looks similar under electron microscope but Melechko et al. [42] showed that the planar structures and arrangement of graphen in both structure is different (Figure 2.3). Unlike in nanotubes, in carbon nanofibers the graphene planes are wrapped into truncated conic sections. Anisotropic structures of graphene planes are present in carbon nanofibers so defining intrinsic electrical properties of carbon nanofibers is difficult. Carbon fiber diameter ranges from 100 to 150 nm with several micron lengths.

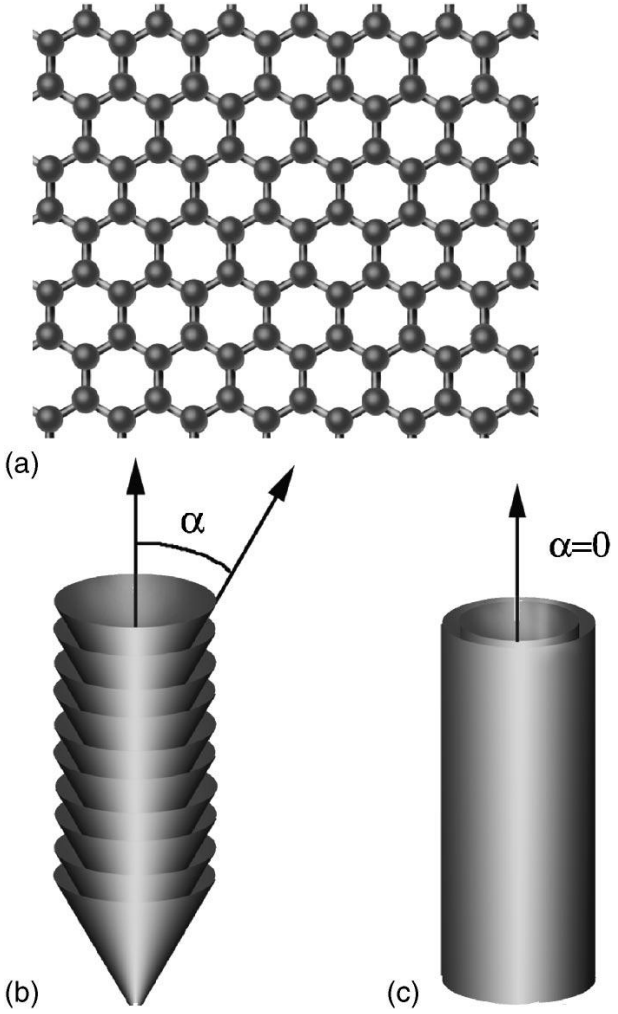

Figure 2.3 Schematic structure of carbon naotubes (a) graphene layer, (b) stacked cone sherringboned nanofiber, and (c) nanotube [31]

2.4.2 Carbon Nanotubes

Carbon nanotubes are the allotropes of carbon, cylindrical in nature and made by rolled graphene sheets. CNTs show incredible thermal, mechanical, and electrical properties. The chemical composition of the carbon nanotubes is simple but shows diverse structure property relationships. Each carbon atom in the nanotube is attached to three neighboring carbon atoms by sp^2 bonding in x-y plane. The presence of sp^2 bonding in carbon nanotubes which forms a hexagonal lattice is stronger than sp^3 bonding which forms a cubic structure in diamond. The theoretical tensile strength of carbon nanotubes is 130-150 GPa and the modulus is over 1000 GPa [43]. In laboratories actual measured values of up to 63 GPa has been reported which is higher than diamond, Kevlar, or spider's silk. Comparison of various materials properties are shown in Table 2.3.

The delocalized pi-electron cloud in the z-direction of the graphene plane gives unique electrical properties to carbon nanotubes [44]. Thermal and electrical conductivity of the carbon nanotubes depends on the chirality or twist of the carbon nanotubes (chirality is the chiral angle between hexagons of carbon nanotubes and the tube axis). Fig. 2.4 shows different structures formed by CNTs due to arrangement of hexagonal lattice structure. Single wall nanotubes can be either conductive or semiconductive according to the structure. However, measuring electrical and thermal properties of single nanotubes is challenging.

Table 2.3 Comparison of various materials' properties

Material	Young's Modulus (GPa)	Tensile Strength (GPa)	Density (g/cm^3)
Single wall nanotube	1054	150	1.4
Multi wall nanotube	1200	150	2.6
Diamond	600	130	3.5
Kevlar	186	3.6	7.8
Steel	208	1	7.8
Wood	16	0.008	0.6

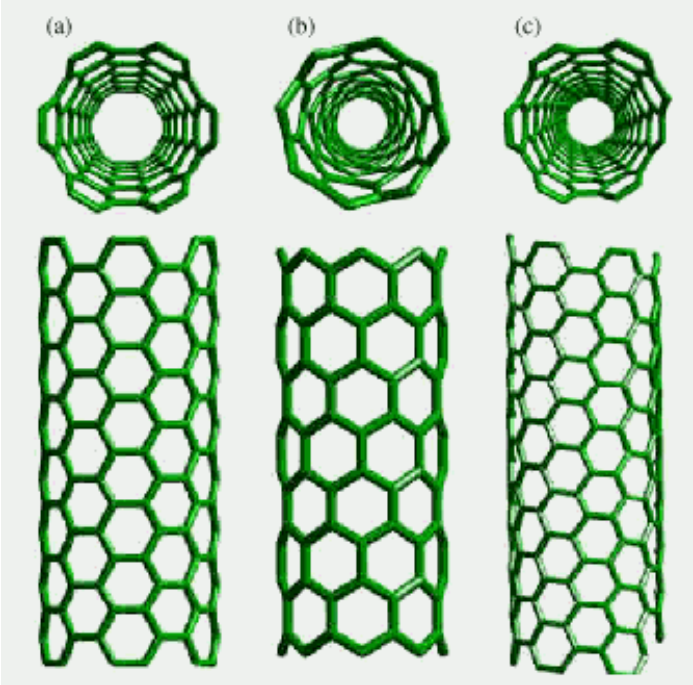

Figure 2.4 Schematic illustrations of the structures of (A) armchair, (B) zigzag, and (C) chiral SWNTs. Projections normal to the tube axis and perspective views along the tube axis are on the top and bottom, respectively [34].

There are two types of carbon nanotubes: 1) Single wall carbon nanotubes (SWNTs) and 2) multi wall carbon nanotubes (MWNTs). MWNT consists of one atom thick single graphene sheet rolled around itself. A diameter of ananometer and length up to 1000 nm has been achieved by many researchers depending on the synthesis process variables. SWNTs show better electrical transport properties than MWNTs. MWNTs consist of many concentrically nested SWNTs [45]. Space between concentric nanotubes is slightly larger than the single graphene sheet because geometrical strains occurr during formation of nanotubes. MWNTs having outer diameter of 4-50 nm, inner nanotube diameter of 2.2 nm, and length up to several microns has been reported by researchers. In this work, I have used MWNTs supplied by Baytubes® and the detail information has been given in Chapter 3 and 4.

2.5 Dispersion of Nanotubes in Polymer Matrix

Due to high polarizability of the pi-electrons there is a strong interaction between adjacent nanotubes through van der Walls' forces and weak interaction between graphene sheets. Attraction between nanotubes to nanotubes leads to formation of agglomerates of nanotubes and that hinders well dispersion of nanotubes in polymer matrix. The dispersion of nanotubes in the polymer matrix can be improved by covalent treatment or non-covalent treatment of carbon nanotubes (CNTs). In covalent treatment attachment of the chemical structure on the surface of the nanotubes or at the end of nanotubes is possible. Covalent treatment causes change in possible hydrogen bonding and results in separation of nanotubes and can be dispersed in a common solvent of polymer and nanotubes [46]. Solvent treatment also improves the interfacial adhesion between CNT and polymer matrix. Functionalized CNTs ensure the reactive coupling of

CNT to polymer matrix. This results in stronger interfaces and efficient load transfer between CNTs and polymer matrix. Covalent treatment of CNT can ensure better mechanical properties of the composite due to better dispersion of CNT in polymer matrix but at the same time covalent treatment adversely affects the intrinsic properties of CNTs. This route causes the change in aspect ratio of the CNTs which generally affects the percolation threshold of the composite. Electrical properties of CNTs can also be hampered due to adverse effects of covalent treatment on the Fermi level and perturbation of the pi-conjugation of CNTs [47]. Covalent treatment also decreases the phonon-scattering length which affects the thermal conductivity of the CNTs [48]. The changes in intrinsic properties of CNTs directly affect the overall properties of polymer/CNT composite.

Non-covalent treatment is effective to disperse the CNTs without disturbing pi-conjugation of the CNTs so that the intrinsic properties of the CNTs can be preserved. S. Bose et al. [49] have shown that the electrical properties of the non-covalently treated CNTs and polymer composites are better than the covalently treated CNTs and polymer composites. The statistics of journal papers reviewed is given in Figure 2.5 showing the strengths and weaknesses of covalent and non-covalent treatments on the composite properties.

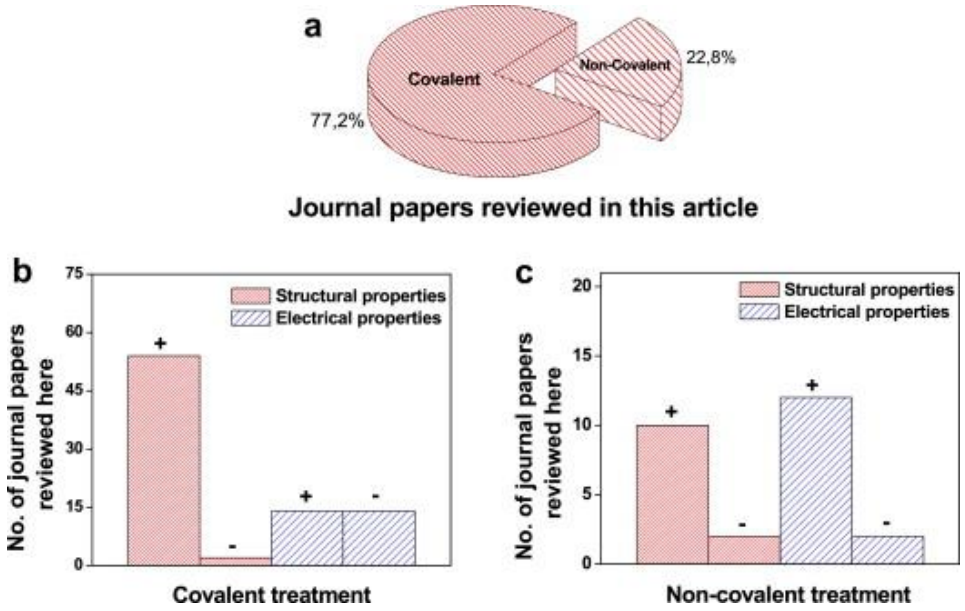

Figure 2.5 (a) Overall statistics of the journal papers reviewed in this article which addresses the influence of various pre-treatment in polymer/CNT composites and compares with respect to pristine CNT; (b) Statistics showing the strengths (+) and weaknesses (-) of covalent and (c) non-covalent types of pre-treatment on the composite properties (statistics also includes paper which report simultaneous improvement in both structural and electrical properties) [38].

Good mechanical and electrical properties can be achieved if good interfacial interaction and better dispersion of CNT in polymer matrix is achieved [50]. CNT dispersion in the polymer matrix is one of the major challenges limiting realization of the advantages of CNT polymer nanocomposites. Better interfacial adhesion between polymer and filler gives better mechanical properties due to effective load transfer from polymer to filler. Also load should get distributed over the supporting filler. Effective load transfer depends upon the shear stress between matrix and filler interface. A high shear stress would transfer load from matrix to filler at shorter distance while low shear stress would transfer the load over long distance. Load transfer between matrix and filler basically occurs by three mechanisms; chemical bonding, weak van der Walls forces,

and physical micro interlocking [51]. Physical micro interlocking is difficult in CNT due an atomically smooth surface.

When CNTs are dispersed randomly in the polymer matrix, thermal, mechanical, or electrical properties are expected to be isotropic. As the filler content in the polymer matrix increases, a gradual transition from predominant polymer matrix properties to filler properties occurs. Above certain concentration of fillers in polymer, overall properties of the composite are dominated by filler properties and that transition point is called as percolation threshold. At the percolation threshold there is a formation of a percolating network of filler in the polymer matrix which helps to transfer electrical, thermal, or mechanical forces from one end to another. The required concentration for percolation threshold reduces with increased dispersion of fillers in matrix [52].

2.6 Percolation Theory

The bulk electrical conductivity of the single atom thick graphene is highly isotropic. Along the graphene planes the electrical conductivity takes place without any scattering while conductivity perpendicular to the graphene plane involves considerable scattering losses. Graphenes in-plane electrical conductivity is 2.1×10^6 S/m and perpendicular to graphene plane is 5×10^2 S/m [53]. Carbon nanotubes are nothing but rolled graphene sheets so at least from an electrical point of view, the intrinsic electrical conductivity of nanotubes is similar to graphene sheets. Bulk electrical conductivity can be different depending on factors like orientation, entanglement, agglomeration, number of walls in nanotubes, etc. In MWNTs ballistic conductivity like superconductivity (electron transfer without any collision losses) is observed by Poncharal et al. [54].

The addition of such highly conductive particles in dielectric materials like polymers can make polymers conductive or semi-conductive. Percolation theory (as illustrated in Figure 2.6) is based on the way these nanoparticles form links to conduct electricity when dispersed in the polymer matrix. Addition of very low amount of conducting particles or highly dispersed particles in polymer matrix cannot impart conductivity. When the addition of conductive particles results in particle to particle contact, they form a conductive path and the whole composite can become conductive. An increase in the concentration of conductive particles in dielectric materials increases the probability of forming conducting paths throughout the dielectric material. In addition, the conductivity of the whole composite depends on the dielectric properties of the polymer matrix. Thus percolation threshold is defined as a critical concentration of conductive particles at which an insulating matrix becomes suddenly conductive.

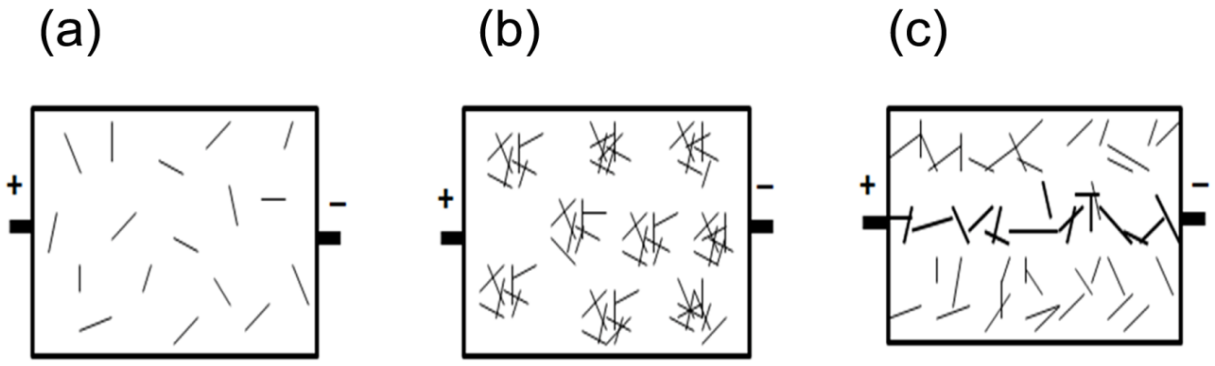

Figure 2.6 Percolation theory: (a) Well dispersed conductive nanofillers: Non conductive composite (b) High concentration of fillers, well distributed but not forming conductive path (c) Filler concentration at percolation threshold forming conductive path.

2.7 Piezoresitivity in CNT Filled Nanocomposites

Piezoresistivity is a phenomenon in which electrical resistance of the material changes with change in applied stress or strain. By the addition of carbon nanofillers, a dielectric polymer matrix can be made electrically conductive. In electrically conductive materials, a change in the electrical resistance can be measured easily. So when applied stress or strain on the material is changed, there is a change in measured electrical resistance of the material. Thus change in the electrical resistance of the material is directly related to the change in the stress or strain of the material. In this way, strain sensing is possible with piezoresistive materials. Polymeric nanocomposite materials are the best suited materials for this application as they can be designed for the required stress or strain. To achieve piezoresistivity in polymeric nanocomposites concentration and loading configurations are important issues that need to be studied and investigated in detail.

In this dissertation poly(hydroxyl butyrate-co-valerate) (PHBV) and poly(butylenes adipate-co-terephthale) (PBAT) were used as a host material and CNTs were used as a conductive nanofillers. CNT filled composites were prepared by non covalent melt blending technique. Various issues like mechanical properties, thermal properties, morphological structure, piezoresistivity under dynamic and transient stress loading conditions, non-linear piezoresistive response, blend miscibility, etc. were studied and discussed elaborately in this dissertation.

2.8 References

[1] Suprakas SR, Kazuaki O, Masami O. Macromolecules 2003;36:2355–2367.

[2] Ishioka R, Kitakuni E, Ichikawa Y. Biopolymers, volume 4, In: Doi Y, Steinbuchel A, editors. Polyesters III: applications and commercial products. Weinheim: Germany: Wiley-VCH Verlag GmbH; 2002. p. 275.

[3] Gruber P, O'Brien M. Biopolymers, volume 4. In: Doi Y, Steinbu chel A, editors. olyesters III: applications and commercial products. Weinheim: Germany: Wiley-VCH Verlag GmbH; 2002. p. 235.

[4] Yves P, Douglas ED, Karen K, Chris S. Science 1992;256:520-523.

[5] Asrar J, Gruys KJ. Biopolymers, volume 4. In: Doi Y, Steinbu¨ chel A, editors. Polyesters III: applications and commercial products. Weinheim: Germany: Wiley-VCH Verlag GmbH; 2002. p. 53

[6] Doi Y, Kunioka M, Nakamura Y and Soga K, Macromolecules 1986;19:1274.

[7] Koning D, Can G. J Microbiol 1995;41;303–309.

[8] Doi Y. Macromol Symp 1995;98,585.

[9] Luo S, Netravali AN. Polym Degrad and Stab 2003;80:59.

[10] Imam SH, Gordon SH, Shogren RL, Tosteson TR, Govind NS, Greene RV. Appl and Environ Microbiology 2009;65:431.

[11] Lai M, Li J,Yang J, Liu J, Tong X, Cheng H. Polym Int 2004;53:1479.

[12] Liu WJ, Yang HL, Wang Z, Dong LS, Liu JJ. J Appl Polym Sci 2002;86:2145.

[13] Zhihua G, Kazuhiro K, Motonori Y, Hideki A, Yoshiharu D. Polymer Degradation and Stability 2004;83:289–300.

[14] Luo JJ, and Daniel IM. Compos. Sci. Technol. 2003; 63 (11): 1607–1616.

[15] Usuki A, Kawasumi M, Kojima Y, Okada A, Kurauchi T and Kamigaito O J. Mater. Res.1993, 8 (5): 1174.

[16] Dennis HR, Hunter D, Chang D, Kim S and Paul DR. Polymer 2001; 42: 9513–9522.

[17] Vaia RA, Jant KD, Kramer EJ and Giannelis EP. Chem. Mater. 1996; 8: 2628–2635.

[18] Vaia RA, Ishii H and Giannelis EP. Chem. Mater. 1993; 5: 1694–1696.

[19] Rehab A and Salahuddin N. Materials Science and Engineering A 2005; 399: 368–376.

[20] Burnside SD and Giannelis EP. Chem. Mater. 1995; 7: 1597-1600.

[21] Usuki A, Kawasumi M, Kojima Y, Okada A, Kurauchi T and Kamigaito OJ. Mater. Res. 1993; 8(5): 1174.

[22] Halvatty V and Oya A. Appl. Clay Sci. 1994; 9: 199–210.

[23] Hussain F, Dean D and Haque A. Structures and Characterization of Organoclay-Epoxy-Vinyl ester Nanocomposite, ASME International Mechanical Engineering Congress and Exposition, LA, USA, IMECE 2002; 33552.

[24] Lan T, Kaviratna PD and Pinnavaia TJ. 1995; 7(11): 2144–2150.

[25] Kawasumi M, Hasegawan M, Usuki A and Okada A. Macromolecules 1997; 30: 6333–6338.

[26] Zhang F, Zhang H, Su Z. Polymer Bulletin 2008; 60: 251–257.

[27] Maurizio A, Maria EE, and Ezio M. Nano letters 2001; 1(4): 213-217.

[28] Ogboma SM, Richardson MC, Braterman PS, Xu ZP and D'Souza NA. Annual Technical Conference Proceedings of the Society of Plastics Engineers Milwaukee, 2008.

[29] Kornmann X, Linderberg H and Bergund L A. Polymer 2001; 42: 4493–4499.

[30] Lee DC and Jang LW. J. Applied Polymer Sci. 1998; 68(12): 1997–2005.

[31] Iijima S. Nature 1991; 354 (6348): 56.

[32] Iijima S and Ichihashi T. 1993; 363(6430): 603–605.

[33] Bower C, Rosen R, Jin L, Han J, Zhou O. Applied Physics Letters 1999; 74(22): 3317–3319.

[34] Cooper CA, Ravich D, Lips D, Mayer J and Wagner HD. Composites Science and Technology, 2002; 62(7–8): 1105–1112.

[35] Haggenmueller R, Gommans HH, Rinzler AG. Chemical Physics Letters 2000; 330(3–4): 219–225.

[36] Jin L, Bower C and Zhou O. Applied Physics Letters 1998; 73(9): 1197–1199.

[37] Jin Z, Pramoda KP, Xu G and Goh SH. Chemical Physics Letters 2001; 337(1–3): 43–47.

[38] Kearns JC and Shambaugh RL. Journal of Applied Polymer Science 2002; 86(8): 2079–2084.

[39] Lozano K and Barrera EV. Journal of Applied Polymer Science 2001; 79(1): 125–133.

[40] Potschke P, Fornes TD and Paul DR. Polymer 2002; 43(11): 3247–3255.

[41] Safadi B, Andrews R and Grulke EA. Journal of Applied Polymer Science 2002; 84(14): 2660– 669.

[42] Melechko A. Journal of Applied Physics 2005; 97: 041301.

[43] Yu M, Lourie O, Dyer M J, Moloni K, Kelly TF, Ruoff RS. Science 2000; 287(5453): 640.

[44] Terrones M. Annu Rev Mater Res 2003; 33: 419–501.

[45] Baughman RH, Zakhidov AA and Walt A. de Heer. Science 2002; 297 (5582): 787 – 792.

[46] Dyke CA, Tour JM. J Phys Chem A 2004; 108(51): 11151–9.

[47] Kamaras K, Itkis ME, Hu H, Zhao B, Haddon RC. Science 2003; 301(5639): 1501.

[48] Padgett CW, Brenner DW. Nano Lett. 2004; 4(6): 1051–3.

[49] Bose S, Khare RA, Moldenaers P. Polymer 2010; 51: 975–993.

[50] Wagner HD, Vaia RA. Nanocomposites: issues at the interface. Mater. Today 2004; 7: 38–42.

[51] Schadler LS, Giannaris S C and Ajayan PM. Applied Physics Letters 1998; 73(26): 3842–3844.

[52] Strano MS, Nanocomposites: Polymer-wrapped nanotubes. Nat. Mater. 2006; 5: 433–434.

[53] Matsubara K, Sukihara K, and Tusuku T. Phys. Rew. B 1990; 41: 969.

[54] Poncharal P, Berger C, Yi Y, Wang ZL, and de Heer WA. Journal of Phys. Chem. B 2002; 106: 12104.

CHAPTER 3

POLY(3-HYDROXYBUTYRATE-*CO*-3-HYDROXYVALERATE)/MULTIWALL CARBON NANOTUBES NANOCOMPOSITES

3.1 Introduction

Recent concern about the harmful effects of petroleum based non biodegradable polymers on the environment has raised new challenges for polymer industries. One of the solutions to tackle this problem is to replace the synthetic petroleum based polymers with equally competitive biobased biodegradable polymers. Poly(hydroxyalkanoates) (PHA), a family of biopolymers has attracted much attention recently, due to their complete biodegradability, biocompatibility, and natural origin. Most significantly, their mechanical properties are similar to that of widely used polypropylene. Several applications have been proposed for PHA polymers in the fields of medicine, agriculture, and packaging [1]. The most studied and easily produced member of this family is poly(3-hydroxybutyrate) (PHB), an isotactic, high molecular weight polymer whose mechanical properties compare favorably with polypropylene [2]. Produced in the form of intracellular granules by several microorganisms, PHB serves as a carbon and energy storage material. However, some drawbacks have prevented its introduction in the market as a valid alternative to the currently widespread nondegradable oil-based thermoplastics. Some of these drawbacks are its fragility, thermal degradability at temperatures not far above the melting point, and its high price [3].

In order to improve the properties of PHB, several kinds of PHA copolymers have been described in the literature incorporating structural units such as 3-hydroxyvalerate to obtain poly(hydroxybutyrate-co-valerate) (PHBV) [4]. PHBV is an attractive material

for environmental waste management and can be used as a substitute for conventional polymers when recovery for recycling or incineration is difficult or not cost effective [5-7]. Unfortunately, PHBV presents the following problems to be solved, which are: slow crystallization rate, relatively difficult processing due to low melt viscosity, low elongation at break, and very high crystallinity. Slow crystallization rate of the PHBV during processing causes tackiness for long period of time in the final product until it becomes completely crystalline. Even after cooling, PHBV with higher contents of hydroxyvalerate (HV) units will stick to each other as the PHBV chains still remain in the amorphous state [8]. Many researchers, including us, have proved improvement in the crystallization rate of the polymers by addition of fillers such as nanoclays, talc, carbon nano fibers, carbon nanotubes, etc. [9-13]. In all these efforts, solution casting and melt blending techniques were used to prepare polymer composites. In general, all methods showed higher recrystallization temperatures by addition of fillers. When comparing the melting temperature to the recrystallization temperature, the slow crystallization rate of PHB based polymers and copolymers is evident by a ~100 degree difference in the melting and recrystallization temperatures. A decrease in the difference between melting and recrystallization occurs for all fillers with the nucleation efficiency of carbon nanotubes [6] and graphene nanofillers [11] being the best (smallest difference between melting and recrystallization temperatures).

In addition to the growing interest in polymers from renewable resources, the importance of multifunctionality from the polymers has grown specially with the growth of polymer sensors [14, 15]. The discovery of carbon nanotubes by S. Iijima in 1991 [16] has resulted into the designing of novel materials with extraordinary combination of

mechanical, thermal, and electrical properties [17, 18]. Nanocomposites made up of biodegradable polymer matrices and carbon nanotubes are a class of advanced novel materials with great application potential such as: biocompatible and biodegradable sensors or actuators [19], anti-static conductive smart packaging [20], structural health monitoring [21], etc. In this work, nanocomposites of PHBV with carbon nanotubes as a fillers have been designed with the aim of exploring the mechanical, thermal, and electrical properties of PHBV/MWNT nanocomposites. The addition of MWNT to the PHBV biopolymer is anticipated to enhance the crystallization rate, thermal, mechanical, and electrical properties.

3.2 Experimental

3.2.1 Materials

PHBV (Mw = 250 000 g mol^{-1}) with 18 mol % hydroxyvalerate content was supplied by the School of Chemical Engineering (State University of Campinas, Brazil). PHBV was dried in an oven for 48 hours at 40 ^{o}C. MWNT (Baytubes® C150 P) were obtained from Bayer MaterialScience (Leverkusen, Germany), with outer number of walls 3-15, outer mean diameter 13-16 nm, inner mean diameter 4 nm, length 1-10 μm and bulk density 140-160 kg/m^3. MWNT were used as received without further purification. Prior to melt mixing, MWNT were vacuum dried at 100 ^{o}C for 4 hours.

3.2.2 Nanocomposites Preparation

Dried MWNT and PHBV were melt blended together in a counter rotating Brabender batch mixer at 170 °C temperature and 100 rpm for 5 min. Compression molding was used to make film samples for thermo-mechanical testing. Samples for electrical testing were prepared using metal template of 25 X 25 X 4 mm^3 size.

Compression molding was carried out at 170 °C under 10 MPa pressure with 10 min residence time. The contents of MWNT in PHBV powder were 0, 1, 5, and 10 weight percentage; and the compositions were coded as PHBV, PHBVCNT1, PHBVCNT5, and PHBVCNT10 respectively.

3.2.3 Measurements and Characterization

3.2.3.1 Mechanical Properties

The uniaxial tension and compression tests were performed on a MTS 810 Material Test System (MTS, Eden Prairie, MN, USA), in which the upper platen was fixed and the lower platen was mobile. Both the tension and compression tests were done at a strain rate of 5 mm/min. The axial force and the displacement data were recorded.

3.2.3.2 Differential Scanning Colorimetry (DSC)

Thermal transitions were determined using a Perkin–Elmer DSC6 (Norwalk, CT, USA), using 10 °C/min heating rate in an inert atmosphere of nitrogen. Samples were first heated from 20 to 190 °C and maintained at this temperature for 5 min until completely melted, thus eliminating the thermal history. Samples were then cooled to 20 °C. After holding for another 5 min at 20 °C, samples were again heated to 190 °C to study the behavior in the absence of the previous thermal history. The % degree of crystallinity was calculated according to the relation: $X_c = (\Delta H_f \times X_m) / \Delta H^o_f$, where ΔH_f is the enthalpy of fusion, X_m is the weight fraction of PHBV in the composite and ΔH^o_f is theoretical heat of fusion value of 100% crystalline PHBV. ΔH^o_f was taken as 109 J g^{-1} [22].

3.2.3.3 Dynamic Mechanical Thermal Analysis (DMTA)

The viscoelastic properties of PHBV and the nanocomposites were measured using a Rheometric Solids Analyzer 3 (RSA3) DMTA instrument (TA instruments, New Castle DE, USA) operating in the tensile mode. For the viscoelastic measurements, film samples measuring 25 x 5 x 0.12 mm^3 were used. The tests were done at heating rate of 10 °C/min, a frequency of 1 Hz and strain amplitude of 0.5%. The strain amplitude was determined from a separate strain amplitude sweep test at 1 Hz frequency to establish the linear viscoelastic region. The temperature sweep was conducted between -50 °C to 100 °C. All DMA measurements were done in triplicate to obtain average viscoelastic values.

3.2.3.4 Wide Angle X-Ray Diffraction (WAXD)

WAXD was conducted using a Rigaku model D/Max–Ultima III (Rigaku Tokyo). X-rays were generated at 44 mA current and 40 kV voltage with Cu Kα wavelength (λ) of 1.542 Å. Diffractograms of neat PHBV and nanocomposite samples were recorded at room temperature in an angular 2θ range of 5 to 35 degrees with a step size of 0.02 and a scanning rate of 2 degrees min^{-1}. All experiments were performed on same day with same set of X-ray filters and X-ray alignment.

3.2.3.5 Transmission Electron Microscopy (TEM)

The PHBV/MWNT composite block (5 X 3 X 3 mm) was microtomed into thin slices in a direction perpendicular to the length direction, using a diamond knife and a Reichert-Jung Ultracut microtome at room temperature. The slice size was approximately 70-100 nm. The slices were placed on a copper grid to observe under TEM. Since, the nanotubes embedded in the matrix were not aligned along any specific

direction, a large variety of orientations could be observed in the samples. Consequently, when the microtomy experiment was performed, nanotubes perpendicular to the blade of the knife were cut as well, leading to the subsequent observation of their cross sections. Further, bright-field TEM and diffraction images were recorded using a Philips EM420 (Philips Electronic Instruments Corp., Mahwah, NJ, USA) instrument at an accelerating voltage of 120 kV.

3.2.3.6 Electrical Resistivity

Compression molded samples with a size of 25 X 25 X 4 mm^3 were used for electrical resistance measurement. To ensure good electrical contact silver paste was applied and then fine copper mesh was mounted on both the sample surfaces. The two-probe method was used to measure volume resistance using an Agilent 34410A multimeter (Agilent Technologies, Santa Clara, CA, USA). The two-probe method is based on Ohm's law: V = I·R, with V, I, and R indicating the voltage, current, and resistance between the two electrodes, respectively. As the difference between the resistivity of the copper electrode and the material was significant, a two-probe over four-probe measurement was found to be equitable. After measuring the electrical resistance of the samples, the electrical resistivity ρ was obtained using following equation,

$$\rho = R\frac{A}{l} \tag{3.1}$$

Where,

ρ is the static resistivity (measured in ohm-centimeters, Ω cm)

R is the electrical resistance of a uniform specimen (measured in ohms, Ω)

ℓ is the length of the sample (measured in centimeters, cm)

A is the cross-sectional area of the specimen (measured in square centimeters, cm^2).

3.3 Results and Discussions

3.3.1 Mechanical Properties

Tensile Test

The influence of MWNT content on the mechanical properties of the nanocomposites is shown in Figure 3.1 (a) and detailed in Table 3.1. With the incorporation of 1, 5, and 10 wt % MWNT, the Young's modulus increased for all the compositions while yield stress values increased for 1 and 2 wt % MWNT compositions. This indicated effective stress transfer across the filler matrix interface resulting in the MWNT acting as effective reinforcements. As concentration of MWNT increased, agglomeration resulted in stress concentration and a decrease in the peak stress. A consistent decrease in failure strain with concentration indicates alteration in plastic deformation of the matrix with the incorporation of the MWNT.

Table 3.0.1 Tensile properties of PHBV/MWNT composites

Sample	Tensile Strength (MPa)	Modulus (GPa)	Strain at Break (%)
PHBV	25.10 (± 0.30)	1.12 (± 0.05)	4.01 (± 0.50)
PHBVCNT1	28.20 (± 0.15)	1.24 (± 0.06)	3.45 (± 0.40)
PHBVCNT5	28.50 (± 0.55)	1.32 (± 0.08)	2.75 (± 0.18)
PHBVCNT10	24.20 (± 0.25)	1.42 (± 0.09)	1.5 (± 0.20)

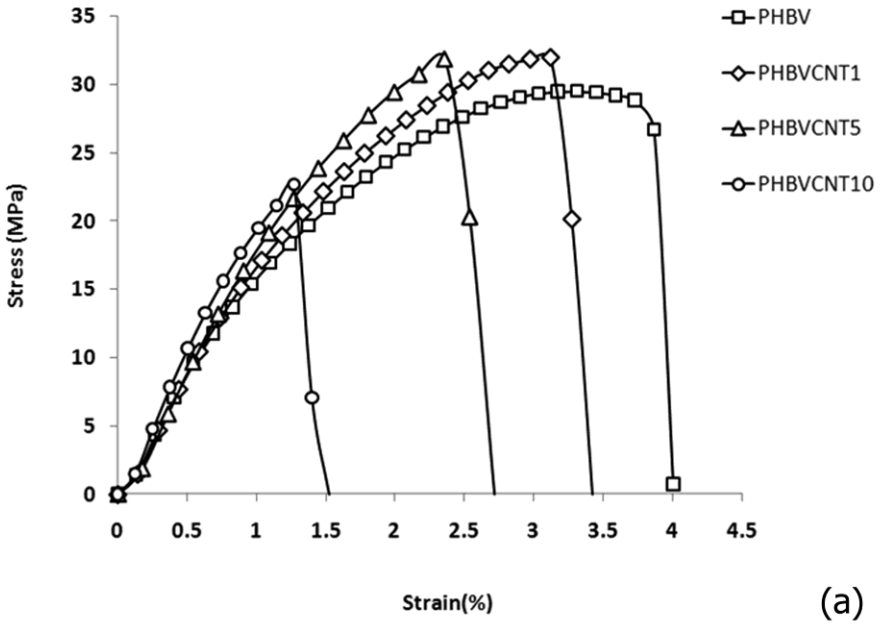

(a)

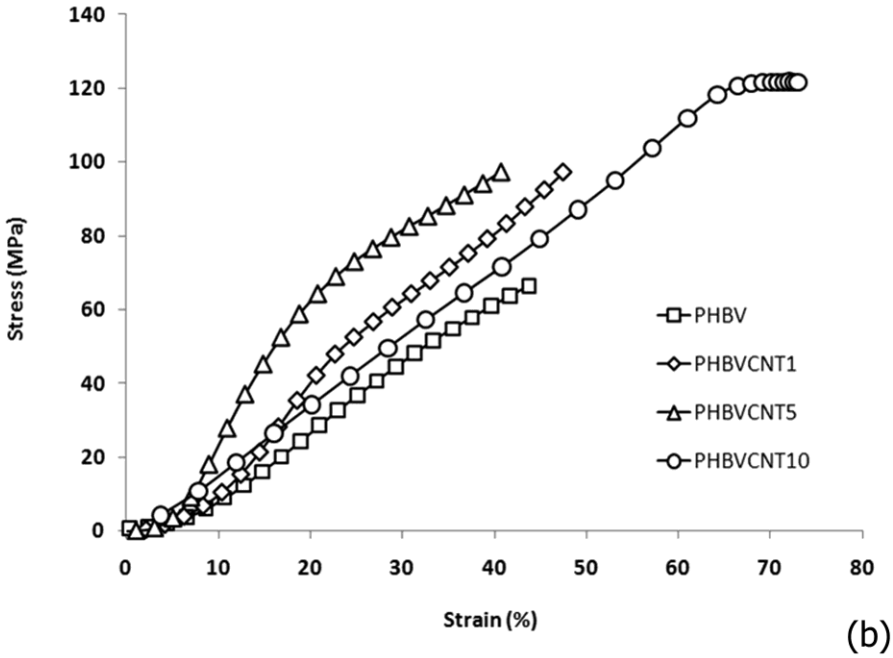

(b)

Figure 3.1 Mechanical test results (a) tensile testing, (b) compression testing.

Compression Test

The compression properties for compression molded composite samples are shown in Figure 3.1 (b) and Table 3.2. It is clear that PHBV composites offer improved compressive properties. Compressive curves were similar to those for most of the synthetic polymers as we have previously found in PVDF [14, 15]. Upper yield strength and modulus values increased with an increase in the % content of MWNT. For PHBVCNT10, at strains past the yield, a broad plateau indicates extensive plastic deformation. It can be also noted that PHBVCNT10 composite showed a very high improvement in the yield stress value under compressive load while the same composite showed poor performance under the tensile loading condition.

Table 3.2 Compressive properties of PHBV/MWNT composites

Sample	Compressive Strength (MPa)	Modulus (MPa)	Strain at Break (%)
PHBV	47 (± 2)	250 (± 6)	42 (± 3)
PHBVCNT1	55 (± 1.5)	340 (± 4)	41 (± 2)
PHBVCNT5	60 (± 2)	587 (± 10)	37 (± 3)
PHBVCNT10	118 (± 2)	160 (± 5)	65 (± 4)

Comparing tensile and compressive properties, it is clear that the compressive peak stress values are higher than the corresponding tensile stress value for the same compositions. This result indicates that failure in the PHBV and its MWNT nanocomposites is associated with heterogeneities in the sample voids or stress concentrations at the interface between MWNT and the polymer. The suppression of void nucleation in compression results in a significant increase in strains for failure compared to the tensile case. The higher strain to failure of the 10% sample coupled to the increased tensile modulus and decreased strain to failure indicates that

embrittlement of the sample increased the flow stress for the composite under compression when stress concentration is suppressed.

Dynamic Mechanical Thermal Analysis

Figure 3.2 (a) illustrate dynamic storage modulus (E') and dynamic loss modulus (E") and Figure 3.2 (b) illustrate tan δ (E"/E') as a function of temperature for all the compositions. E' represents the ratio of the in-phase stress to the applied strain. It represents the stiffness of a viscoelastic material. The loss factor or tan δ is the ratio of loss modulus (E'') to the storage modulus (E'). It is a measure of the energy dissipated, expressed in terms of the recoverable energy, and represents mechanical damping or internal friction in a viscoelastic material. Experiments were conducted in triplicate and the magnitudes of the representative curves shown in the figures have a deviation of not greater than 10%. The higher E' values of PHBV/MWNT nanocomposites reflect the reinforcement potential of MWNT in the PHBV matrix. The increase in the modulus can be ascribed to the reinforcing effect of the nanofillers. Although E' generally increased with increasing MWNT content, a discrepancy between the tensile modulus trends and the DMA E' trends were noted for the PHBVCNT10 composite. For PHBVCNT10, E' was lower than that of PHBV and other composites. The mode of material response is different for the oscillatory strain compared to quasi static strain, indicating that the agglomeration occurring at higher concentration leads to poor strain transfer in the composite.

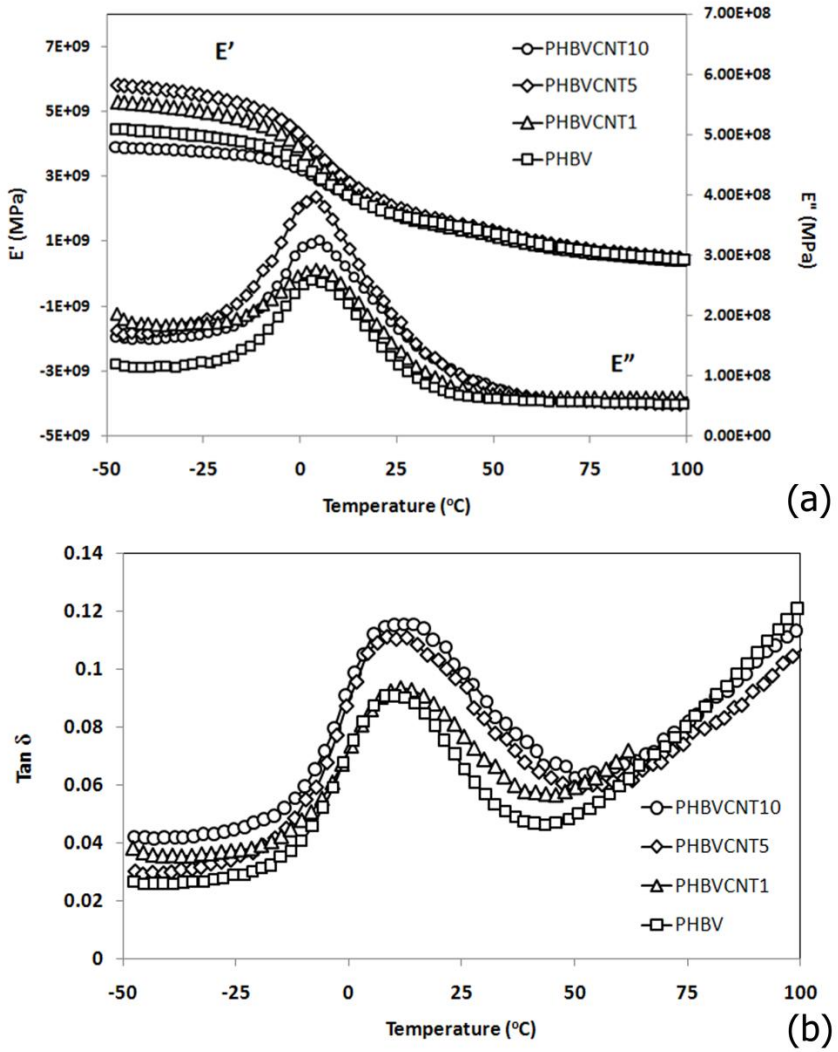

Figure 3.2 Dynamic thermo-mechanical properties of PHBV/MWNT nanocomposites in terms of (a) E' and E" (b) tan d

3.3.2 Differential Scanning Calorimetry (DSC)

Figure 3.3 shows the DSC results for neat PHBV and its nanocomposites. The melting temperature (T_m), melting enthalpy (ΔH_m), cold crystallization temperature (T_{cc}), cold crystallization enthalpy (ΔH_{cc}), melt recrystallization temperature (T_{mc}), melt recrystallization enthalpy (ΔH_{mc}) and the degree of crystallinity (X_c) were obtained from

the thermograms. The results of the first heating and cooling curves and the second heating and cooling curves are summarized in Table 3.3. Compounded PHBV and PHBV/MWNT nanocomposites except PHBVCNT1 showed bimodal endothermic melting peaks in the first heating (Fig. 3.3 (a)). PHBVCNT1 showed a single melting temperature peak at 168 ^{o}C. The bimodal peaks in other compositions correspond to T_m of the crystalline phases; suggest the presence of two crystalline phases in the samples and the two ΔH_m values reflect the relative amounts of the crystalline phases in the PHBV/MWNT nanocomposites. An evaluation of the two melting points in terms of peak height showed that the low-temperature melting peak (164 ^{o}C) was more or less unchanged whereas the high-temperature melting peak (178 ^{o}C) decreased slightly with increasing MWNT content. A similar phenomenon of a decrease in the melting peak temperature with increased nanofiller content in PHBV/montmorillonite nanocomposites was observed by S. Wang et al. [23] and by us for PHBV/LDH (layer double hydroxides) nanocomposites [8]. It was inferred that the low-temperature melting peak was probably related to heterogeneous nucleation of PHBV, which started spontaneously by PHBV chain aggregation below the melting point and the high temperature melting peak is related to homogeneous nucleation of PHBV [24]. The first heterogeneous low melting peak was suppressed in the second heating cycle implying stable crystal formation due to the erasure of metastable crystallization induced by processing during the first heat while the high temperature melting peak increased in intensity. In the second heating and cooling thermographs, PHBV/MWNT composites displayed higher melting enthalpies, higher crystallization temperatures, and narrower and more symmetrical melting and crystallization curves compared with PHBV. This established a

crystallization promoting effect of MWNT in PHBV. It can be observed from the second heating curve (Fig. 3.3 (c)) the absence of cold crystallization curve for composites with MWNT. Here the carbon nanotubes obstruct the diffusion of HV units and hence the recrystallization process. In that case, crystals in the nanocomposite are more unstable than in plain PHBV. However, the presence of the carbon nanotubes in the nanocomposites increased the crystallization temperature of PHBV (Fig. 3.3 (b) and 3.3 (d)). It can be concluded that the nanotubes increase the crystallization rate and have a heterogeneous nucleation effect on the polymer matrix. The nanoscale carbon tubes act as nucleating agents, facilitating the crystallization process. The well dispersed MWNT leads to an increased number of sites available for nucleation, thereby enhancing the crystallization rate. Bhattacharyya et al. [25] reported that this phenomenon should be attributed to the higher thermal conductivity of carbon nanotubes compared with that of the polymer.

Table 3.3 Thermal properties of PHBV and PHBV/MWNT nanocomposites: first heating and cooling

	Composition	Heating			Cooling	
		Peak 1	Peak 2	Peak 1 + Peak 2	T_{mc} (^oC)	ΔH_{mc} (J g^{-1})
		T_{mc} (^oC)		ΔH_m (J g^{-1})		
First heating	PHBV	164	178	62.1	72.7	-14.1
	PHBVCNT1	167	…	44.2	78.6	-49.3
	PHBVCNT5	162	174	54.7	92.4	-66.6
	PHBVCNT10	164	172	42.2	101.0	-53.0
Second heating	PHBV	57.2	172.0	44.3	48.0	-5.0
	PHBVCNT1	-	172.3	49.3	71.2	-44.5
	PHBVCNT5	-	172.2	47.3	96.2	-51.5
	PHBVCNT10	-	173.5	44.8	99.5	-52.4

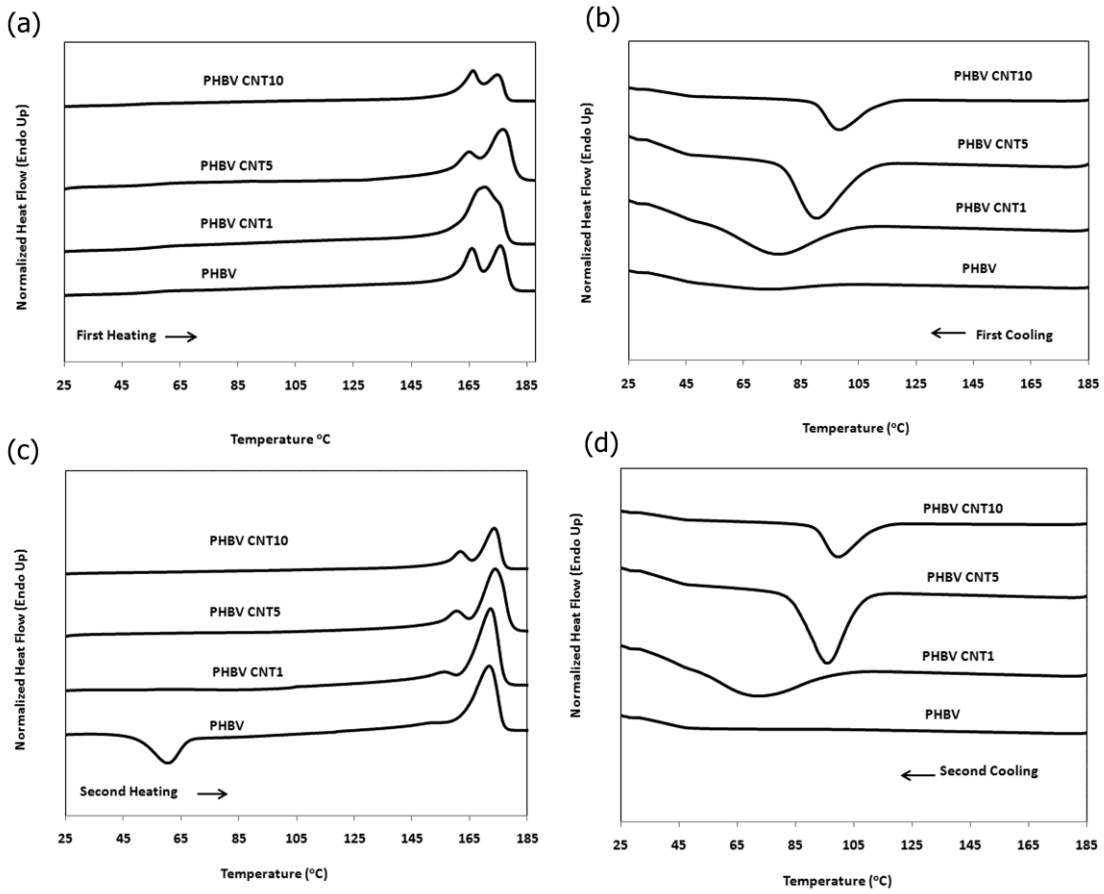

Figure 3.3 DSC traces for PHBV and PHBV/MWNT nanocomposites: (a) first heating; (b) first cooling; (c) second heating; (d) second cooling.

3.3.3 X-Ray Analysis

Figure 3.4 shows X-ray patterns in the range 2θ = 5 to 35^{o} of pristine PHBV and its nanocomposites with MWNT. The WAXD diffractogram of neat PHBV shows that this polyester is a semicrystalline material. Its characteristic reflections have been reported in the literature [26, 27]. These characteristic peaks of PHBV are indicated in Fig. 4 and correspond to an orthorhombic cell [28]. PHBVCNT1, PHBVCNT5, and PHBVCNT10 show PHBV reflections at the same values as for the neat biopolymer, indicating that, in the nanocomposites, PHBV crystallizes in its typical crystalline form. Its unit cell is not changed after incorporation of MWNT. However, the addition of MWNT results in

sharper peaks for the (020), (110) and (021) PHBV reflections compared to that of pure PHBV. The crystallite size L (nm) was determined for the peak corresponding to the (020) reflection using the Scherrer equation which is defined as: $L\ (nm) = 0.94\lambda / \beta \cos\theta$, where λ is the wavelength of the X-ray radiation which is 1.542 Å, θ is the Bragg angle and β is the full width at half maximum (FWHM). Table 3.4 shows the effect of MWNT on the crystalline lamella size for the (020) reflections. The lamella size for the (020) direction increased with increasing MWNT, indicating that the crystalline lamella size increased in the presence of MWNT. These results confirm that the crystallization of PHBV is promoted by the addition of carbon nanotubes, which is in agreement with the DSC data. It should be pointed out that crystallite growth of PHBV varies in different directions. The sharp rise in intensity and narrow peak of PHBV crystals in the PHBV/MWNT composite in particular direction indicates the crystallite growth of PHBV along that direction.

Table 3.4 Effect of MWNT content on the crystallite size for (020) reflections

Composition	FWHM (deg)	d-spacing (nm)	Crystallite size d_{020} (nm)
PHBV	0.457	0.66	14.23
PHBVCNT1	0.6	0.657	15.25
PHBVCNT5	0.56	0.658	18.68
PHBVCNT10	0.53	0.656	16.11

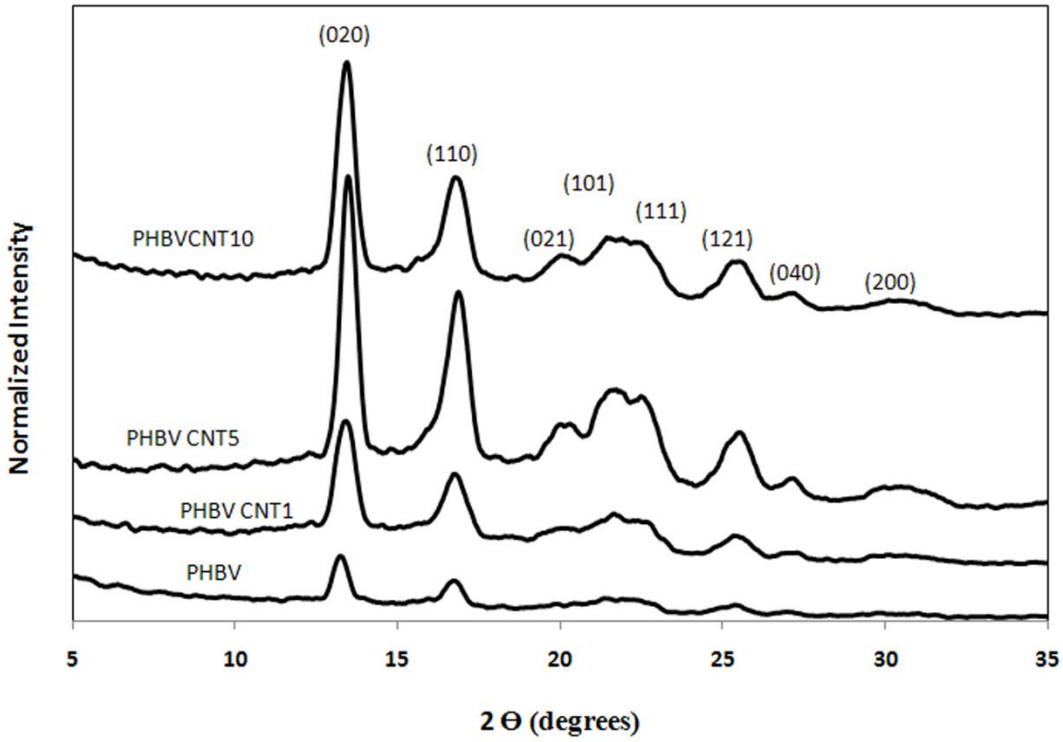

Figure 3.4 WAXD patterns of PHBV and PHBV/MWNT nanocomposites.

3.3.4 Electrical Resistivity

The influence of MWNT contents on electrical resistivity of PHBV/MWNT nanocomposites is shown in Figure 3.5. The volume resistivity of the composites decreased with increasing the MWNT content and the electrical percolation threshold occurred between 2 and 5 wt% MWNT.

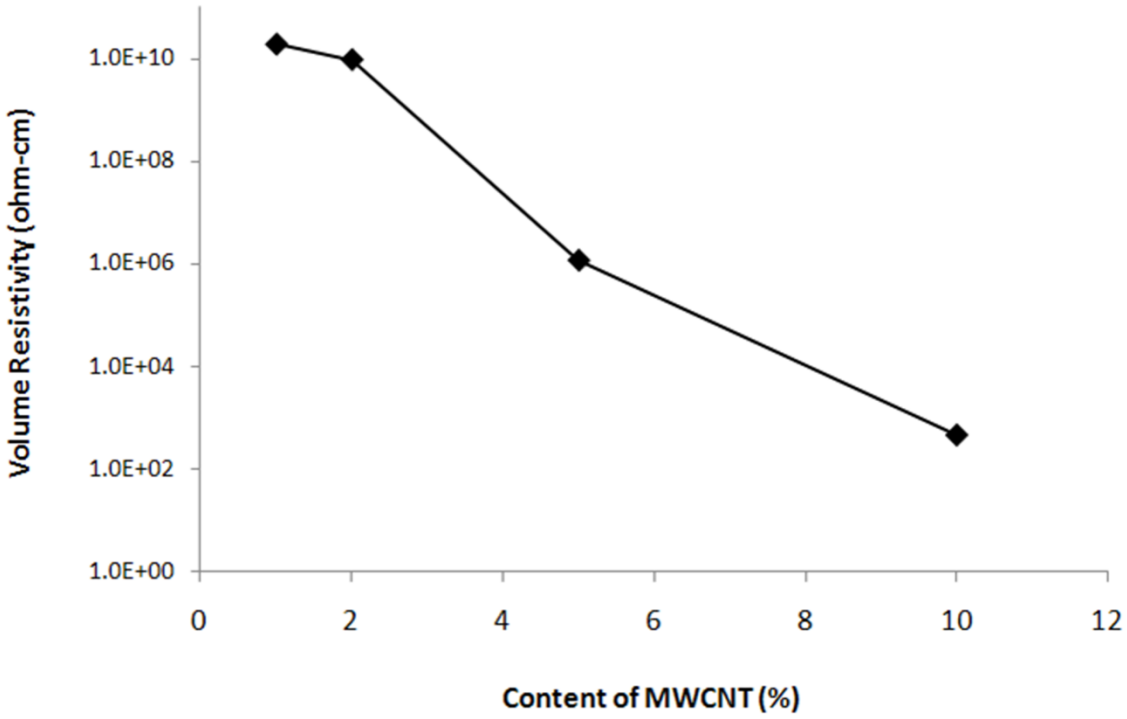

Figure 3.5 Electrical volume resistivity of PHBV/MWNT composites as a function of nanotube content.

3.3.5 Transmission Electron Microscopy (TEM)

The TEM images show good dispersion and wetting of MWNT in PHBV matrix. The extent of nanotube dispersion appears to be strongly dependent on the degree of entanglement, as well as on the strength of the shear forces experienced during processing. Agglomeration does not appear to be extensive in the nanocomposites indicating adequate mixing during extrusion.

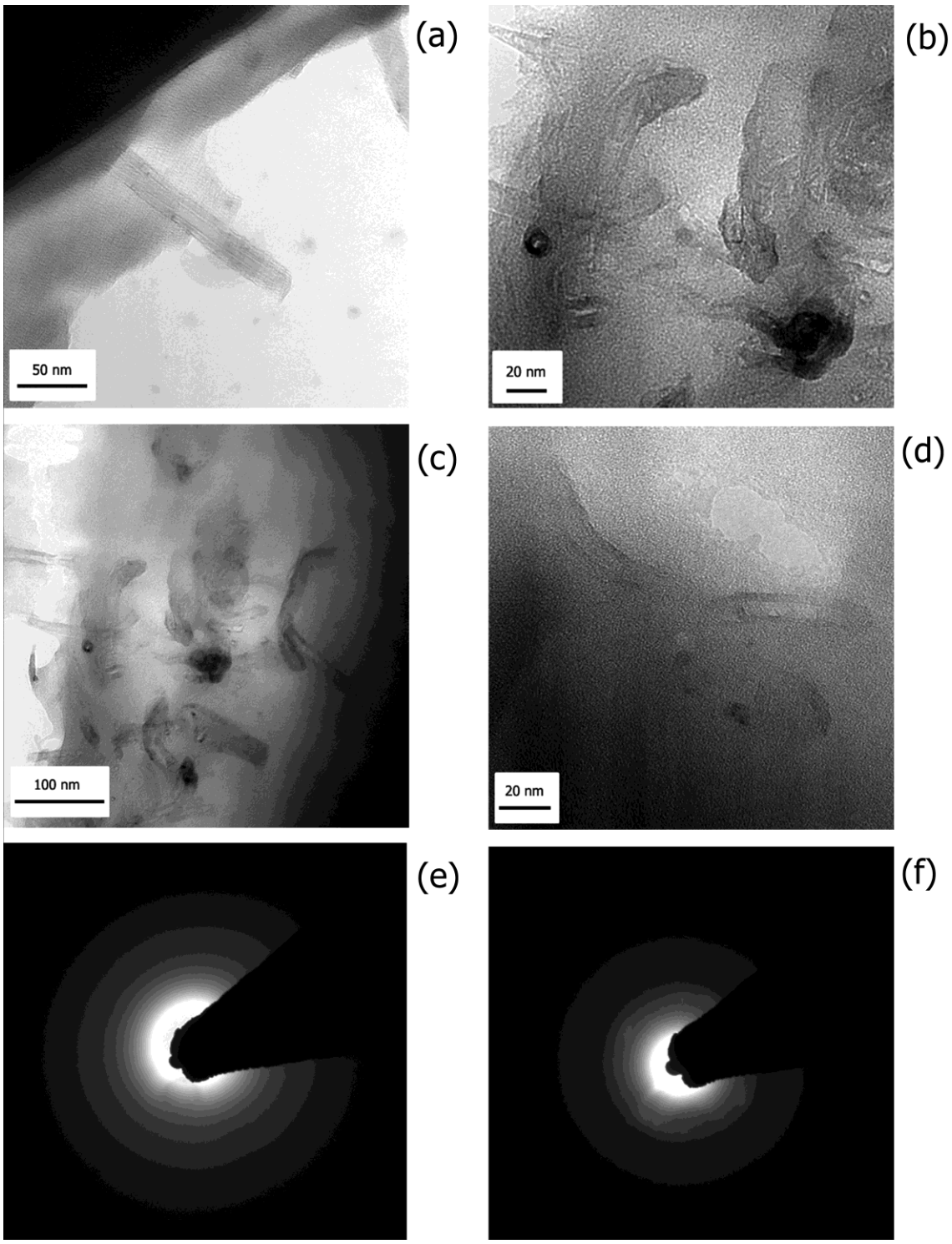

Figure 3.6 Bright field TEM imaging of semicrystalline PHBVCNT1 composites. (a) shows multiwall carbon nano tubes in the PHBV matrix, (b) breakage of agglomerate due to high shear forces during compounding process, (c) and (d) shows well dispersed CNTs in matrix, (e) image showing polycryastalline diffraction pattern of the polymer crystals far away from the CNTs and (f) is of the polymer crystal near CNT rich region.

To form a conductive network of MWNT it is important to preserve the aspect ratio of the MWNT during processing and the nanotubes should not be more then 2 to 3 nm away from each other. Figure 3.6 (e) and (f) shows a diffraction pattern produced by the electron beam through PHBV, which are polycrystalline orthorhombic crystals. TEM diffraction patterns can be obtained in much the same way as X-ray diffraction from powders. Semi crystalline polymers like PHBV have completely random polycrystals. In TEM diffraction we rotate the reciprocal lattice about all axes and produce a set of nested spheres. When we intersect these spheres with the plane (Ewald sphere) we see ring patterns. Amorphous or less crystalline regions produce a diffused ring pattern compared to the brighter ring pattern produced from more crystalline regions. So it can be inferred that the brighter diffraction pattern from the region close to carbon nanotubes (Figure 3.6 (f)) indicates crystallization. This confirms the effectiveness of nanotubes acting as a heterogeneous nucleating agent while the region away from nanotubes resulted in a less crystalline region giving diffused diffraction pattern.

3.4 Conclusion

MWNT were an effective nucleating agent for PHBV showing both the suppression of cold crystallization in the second heating thermogram as well as a ~70 degree increase in recrystallization temperature. The magnitude of the recrystallization temperature varied substantially with an increase in MWNT concentration. Analyzing the X-ray spectra in the context of PHBV crystallinity revealed an increase in crystallite size. Increased peak intensities of XRD peaks confirm that the crystallization of PHBV was promoted by the addition of MWNT, which is in agreement with the DSC data. DMA data showed that CNTs did not affect the T_g but increased storage modulus with an

increase in MWNT content. Improved mechanical properties and electrical conductivity were observed by incorporation MWNT in PHBV matrix.

3.5 References

[1] Pouton CW, Akhtar S. Adv Drug Deliv Rev 1996;18:133.

[2] Hahn SK, Chang YK, Kim BS, Chang HN. Biotechnology and Bioengineering 1994;44:256.

[3] Inoue Y, Yoshie N. Prog Polym Sci 1992;17:571.

[4] Doi Y. Macromol Symp 195;98:585.

[5] Luo S, Netravali AN, Polym Degrad and Stab 2003;80:59.

[6] Imam SH, Gordon SH, Shogren RL, Tosteson TR, Govind NS and Greene RV. Appl and Environ Microbiology 1999;65:431.

[7] Lai M, Li J, Yang J, Liu J, Tong X, Cheng H, Polym Int 204;53:1479.

[8] Liu WJ, Yang HL, Wang Z, Dong LS, Liu JJ. J Appl Polym Sci 2002;86:2145.

[9] Dagnon KL, Chen HH, Innocentini-Mei LH, D'Souza NA. Polym Int 2008;58:133.

[10] Jacquel N, Tajima K, Nakamura N, Miyagawa T, Pan P, Inoue Y. J Appl Polym Sci 2009;114:1287.

[11] Pan P, Liang Z, Nakamura N, Miyagawa T, Inoue Y, Macromol Biosci 2009;9:585.

[12] Dana GM, Hosein HA, Misra M, Lawrence TD, J Appl Polym Sci 2007, 106, 2548.

[13] Kai W, He Y, Inoue Y. Polym Int 2005;54:780.

[14] Vidhate S, Chung J, Vaidyanathan V, D'Souza N. Materials Letters 2009;63:1771.

[15]Vidhate S, Chung J, Vaidyanathan V, D'Souza N. Polymer Journal 2010;42:567.

[16] Iijima S. Nature 1991;56:354.

[17] Ijima S, Ichihashi T. Nature 1993;363:603.

[18] Seo KM, Park SJ. Chem Phys Lett 2004;44:395.

[19] Yang W, P. Thordarson P, Gooding JJ, Ringer SP, and Braet F. Nanotechnology 2007;18:412001.

[20] Nepal D, Balasubramanian S, Simonian AL, and V.A. Davis VA, Nano Lett 2008;8:1896.

[21] ZHANG W, SUHR J, KORATKAR N. JOURNAL OF NANOSCIENCE AND NANOTECHNOLOGY 2006;6:960.

[22] Buzarovska A, Bogoeva-Gaceva G, Grozdanov A, Avella M, Gentile G, Errico M, J Mater Sci 2007;42:6501.

[23] Wang S, Song C, Chena G, Guoa T, Liub J, Zhang B, Takeuchi S, Polym Degrad and Stab 2005;87:69.

[24] Owen AJ, Heinzel J, Škrbić Z, Divjaković V, Polymer 1992;33:1563.

[25] Bhattacharyya S, Kymakis E, Amaratunga GA. Chem Mater 2004;16:4819.

[26] Galegoa N, Rozsa C, Sanchez R, Fung J, Va´zquez A, Tomas JS, Polym Test 2000;19:485.

[27] Kunioka M, Tamaki A, Doi Y; Macromolecules 1989;22:694.

[28] Sandler J, Windle AH, Werner P, Altstädt V, Es MV, Shaffer MS. J Mater Sci 2003;38:2135.

CHAPTER 4

BIODEGRADABLE PIEZORESISTIVE MULTIWALL CARBON NANOTUBE/POLY(3-HYDROXYBUTYRATE-CO-3-HYDROXYVALERATE) COMPOSITES

4.1 Introduction

There is increasing interest in developing piezoresponsive stress sensors in the biomedical industry and for structural health monitoring with low environmental footprint. While previously limited to ceramics, the low strain to failure and problems with adhesion to the underlying substrate led to increased interest in flexible polymer based piezo-sensors. From an initial focus on intrinsic piezoresponse of the polymer, more recent efforts are directed to the incorporation of conductive nanoparticles into the polymer. All materials show a change in resistance through change in length, which is the basis of strain sensing instrumentation. Recognizing that in a dispersed composite, inter-particle distance changes as a function of the strain in the material, a new technology based on nanoparticle dispersed structural health monitoring materials has emerged [1]. Nanotubes in particular offer a viable nanoparticle option for structural health monitoring. Carbon nanotubes (CNTs) offer an extraordinary combination of electrical, mechanical, and thermal properties [2]. The ballistic electrical conductivity and high aspect ratio of CNTs can significantly improve the bulk electrical conductivity of dielectric polymeric materials at low percolation threshold [3]. Such electrically conductive CNT/polymer composite materials can respond by changing their electrical resistance under the influence of change in mechanical stress or strain. This phenomenon of change in electrical resistance with applied stress or strain on the material is called as piezoresistivity. Based on this phenomenon various strain sensors

or self sensing composite structures and some mechanical damage based self-monitoring materials can be developed [4-11]. Many researchers are applying this phenomenon using various types of material systems like thermoplastics [3-6], thermoset resins [7], cement [10], etc. with range of fillers.

Dielectric materials like polymers can be made conductive or semi-conductive by addition of highly conductive CNT particles. The magnitude of conductivity is dependent on how the conducting particles are distributed in the dielectric matrix. Percolation theory (as illustrated in Ch. 2, Figure 2.4) is based on the way the nanoparticles form links to conduct electricity when dispersed in polymer matrix. We have recently established that the functionality of piezoresponse can be obtained at low and high concentrations with a resistive-conductive mechanism both providing a stress-resistance correlation in a MWCNT/polyvinylidene fluoride composites [1]. Changes in resistance were determined to be stress loading rate dependent. The quasi-static compressive loading show a decrease in resistance with stress irrespective of the CNT concentration while transient creep deformation show CNT concentration dependent resistance change. At low concentration lack of CNT-CNT contact leads to change in dielectric response of the matrix, which is related to the distance between the conductive particles. The time dependent response is therefore determined to be resistive in nature. At higher concentrations, when conductive particles come in contact with each other they form conductive or tunneling path and the whole composite become conductive. Increase in the concentration of conductive particles increases the probability of forming conducting paths throughout the dielectric material.

Based on manufacturing considerations, thermoplastics are preferred as they can be easily processed by extrusion and injection molding. Composites can be easily synthesized by the addition of nanofillers and designed for required stress or strain level. This results in reduced cost, good mechanical strength, and ease of stress or strain monitoring.

In this paper, we utilize poly(hydroxybutyrate-co-hydroxyvalerate) (PHBV) as the host matrix for a stress/strain sensor. PHBV is part of the poly hydroxyl alkanoate (PHA) family. PHAs are polyesters of hydroxyalkanoic acids synthesized by bacteria as intracellular-carbon and energy storage compounds and accumulated as granules in the cytoplasm of cells [12]. As biodegradable and biocompatible materials, they have attracted much attention in diverse applications [13]. A frequently utilized member of PHA family is poly(3-hydroxybutyrate), a polymerized 3-hydroxybutyrate discovered in 1927 by Lemoigne. This biomaterial has distinct properties including biodegradability, biocompatibility, and piezoelectric characteristics [14]. It also has the particular advantage that it is thermoplastic and therefore, in principle, can be processed using existing processing equipment.

Thermo-mechanical properties of PHBV are close to conventional petroleum based polypropylene [15,16]. PHBV has attracted much attention recently due to their full biodegradability [17], biocompatibility [18], and natural origin [19]. PHBV shows promise to use in wide range of applications in various fields. Composites made from biodegradable polymer matrix like PHBV and CNTs is a class of advanced novel materials with great application potential. CNT/polymer composites can be used for smart packaging [20], structural health monitoring [21], or advanced biocompatible

prosthetics [22]. For such applications the study of electrical response under the various loading conditions is crucial. In this work, composites of PHBV with MWCNTs as filler have been designed with the aim of exploring the piezoresistive response of MWCNT/PHBV composites.

4.2 Experimental

4.2.1 Materials

PHBV (Mw = 250 000 g mol^{-1}) with 18 mol % hydroxyvalerate content was supplied by the School of Chemical Engineering (State University of Campinas, Brazil). PHBV was dried in an oven for 48 hours at 40 ^{o}C. MWCNT (Baytubes® C150 P) were obtained from Bayer MaterialScience (Leverkusen, Germany), with outer number of walls 3-15, outer mean diameter 13-16 nm, inner mean diameter 4 nm, length 1-10 μm and bulk density 140-160 kg/m^3. Figure 4.1 show the TEM images of Baytubes® MWCNTs. MWCNT were used as received without further purification. Prior to melt mixing, MWCNT were vacuum dried at 100 ^{o}C for 4 hours.

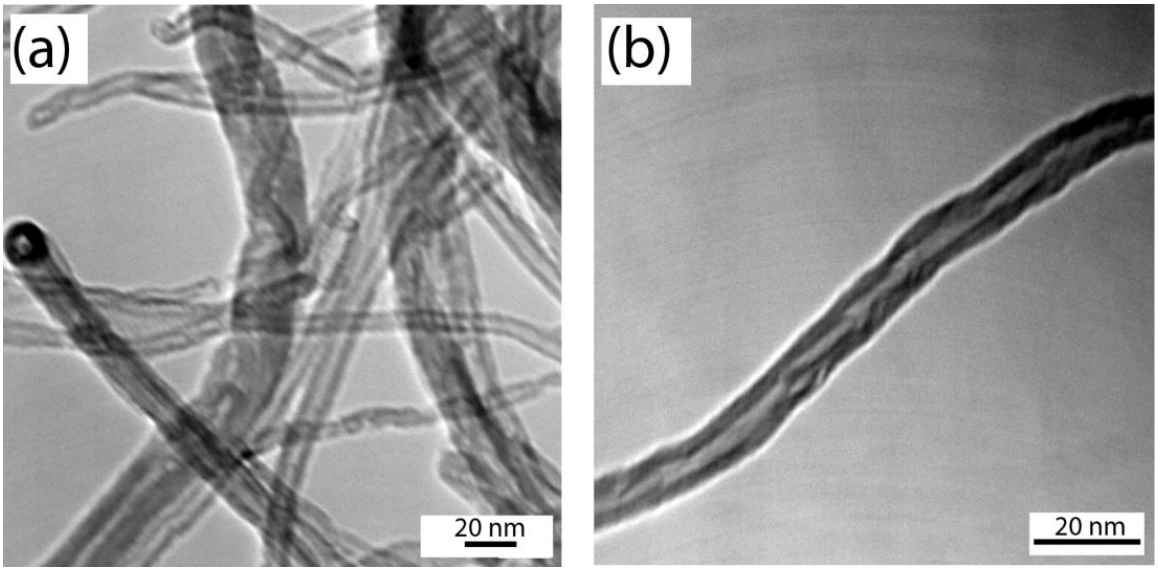

Figure 4.1 TEM images of Baytubes® MWCNTs

4.2.2 Sample Preparation

MWCNTs and PHBV were melt blended in a counter rotating Brabender batch mixer at 170 °C and 100 rpm with residence time of 5 min, followed by a compression molding at 170 °C under 10 MPa for 10 min to form a sheet with smooth surfaces. After natural cooling to room temperature, the sheet was cut into samples with a size of 25 × 25 × 3 mm^3. Silver paste and copper mesh (Fig. 4.2) was applied on the both surfaces to make better electrical contact. The contents of MWCNT in PHBV powder were 0, 1, 5, and 10 weight percentage; and the compositions were coded as PHBV, PHBVCNT1, PHBVCNT5, and PHBVCNT10 respectively.

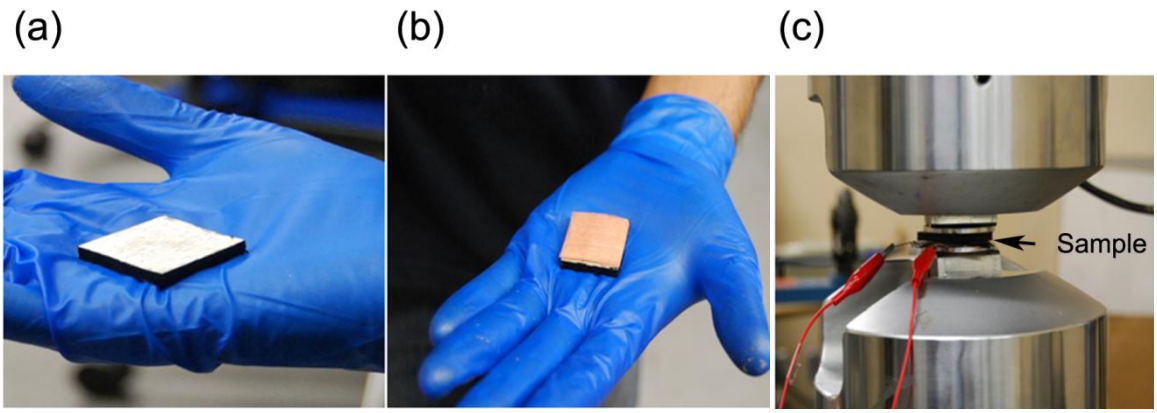

Figure 4.2 Sample preparation and test set up; a) application of silver paste, b) mounting copper mesh and c) compressive test set up

4.2.3 Measurements

The compression tests were performed on MTS 810 Material Test System (MTS, Eden Prairie, MN, USA), in which the upper platen was fixed and the bottom platen was mobile. The two-probe method was used to measure the volume resistance by using Agilent 34410A multimeter. The two-probe method is based on Ohm's law, i.e., V = IR with V, I and R being voltage, current and resistance between the two electrodes

respectively. Since the copper electrode-material resistivity difference was significant, a two point over four point measurement configuration was found to be equitable. The compression test was done at the speed of 0.5 mm/min. The axial compressive force and the displacement data were automatically recorded in a computer. The experimental setup for simultaneous measurements of stress, strain, and volume resistance measurements is schematically illustrated in Fig. 4.3. For creep testing under compression, the specimen was compressed with a certain axial stress which was maintained during the creep period. Compressive creep tests on the composite samples were performed under axial stress of 32 MPa. Fatigue tests were conducted between 1 and 10 MPa in a triangle wave using frequency of 1 cycle per minute.

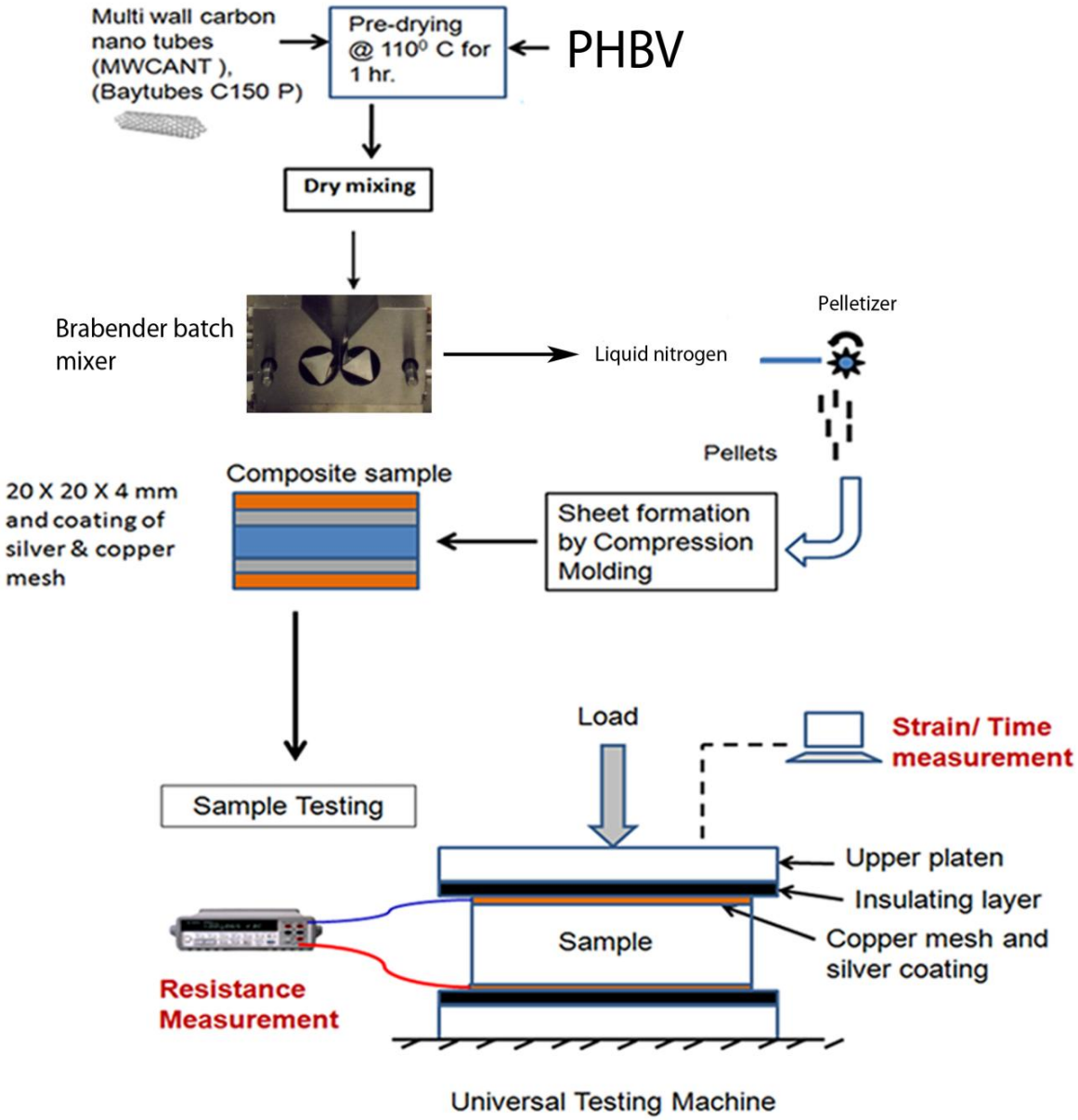

Figure 4.3 Experimental procedure showing sample preparation and electrical, mechanical response measurement technique.

4.3 Results and Discussion

4.3.1 Compressive Stress and Resistance Response under Quasi-Static Loading

Compression tests were performed first to determine the maximum yield stress values of the samples. The compression test results for all compositions are shown in Table 4.1. It is clear that MWCNT reinforced the PHBV matrix and the compressive yield stress and elastic modulus values increased with increase in MWCNT concentration in PHBV.

Table 4.1 Compressive properties of PHBV/MWCNT composites.

Composition	Yield Stress (MPa)	Modulus (Mpa)	Strain at yield
PHBV	47 ± 2	250 ± 6	12 ± 0.8
PHBVCNT1	55 ± 1.5	340 ± 4	10 ± 0.6
PHBVCNT2	57 ± 1.1	368 ± 6	8.8 ± 0.8
PHBVCNT5	60 ± 2	587 ± 10	6.2 ± 0.6
PHBVCNT10	118 ± 2	160 ± 5	5 ± 0.5

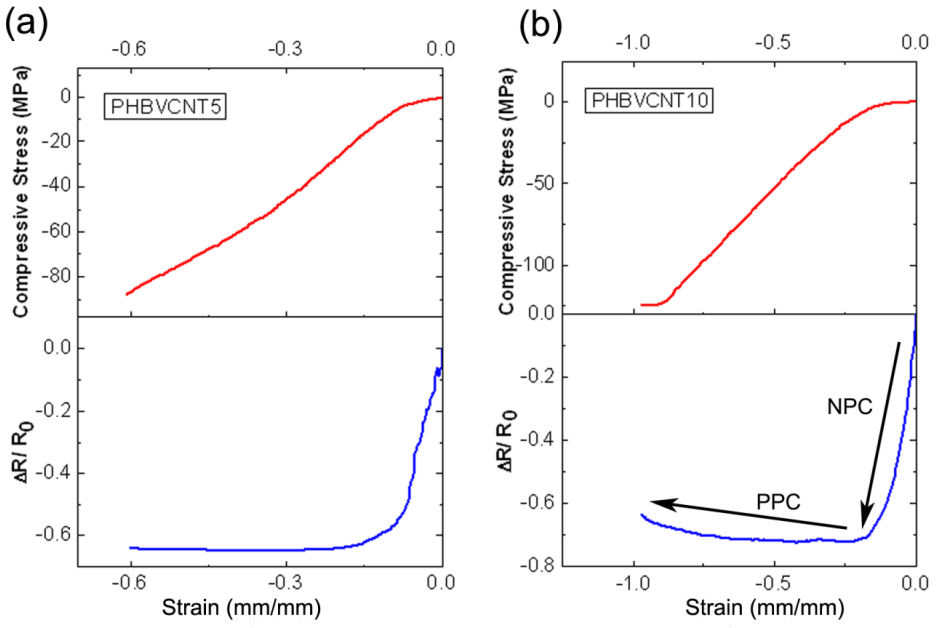

Figure 4.4 Change in the resistance as a function of applied compressive stress.

Figure 4.4 shows change in the fractional resistance ($\Delta R/R_0$) as a function of compressive stress for PHBVCNT5 and PHBVCNT10 samples. R_0 is the resistance before loading and R is the resistance under the loading condition. In the composites, MWCNTs can be considered as incompressible, as Young's modulus of MWCNTs is very high (0.9–5.5 TPa) [23]. When the composite was compressed, the compressibility of the matrix led to decrease in the inter-particle distance of the MWCNTs. For both PHBVCNT5 and PHBVCNT10 composites, the decrease in the resistance with applied stress was very high below 10 MPa. The change in the resistance with respect to change in strain is defined as a gauge factor (GF). GF= ($\Delta R/R_0$) / ε; where ε is a mechanical strain. Metals have a reported gauge factor of around 2 while poly-silicon has a gauge factor around 25. Our previous work with PVDF has shown values in the range of 2 to 3 (close to metals). Here, gauge factor values of 6.25 and 8 were observed for PHBVCNT5 and PHBVCNT10 respectively. When the stress values went above the 10 MPa the change of resistance reduced and at around 30 MPa resistances became constant. Further increase in compressive stress did not change the resistance value of PHBVCNT5 but a gradual increase in the resistance was observed for PHBVCNT10. This phenomenon of increase in resistance with increase in stress is called as a positive pressure coefficient (PPC) and the opposite of it i.e. decrease in resistance with increase in stress is called as a negative pressure coefficient (NPC). For PHBVCNT10, the chances of formation of agglomerates were higher than PHBVCNT5. So after a certain stress level the realignment of the agglomerates and destruction of the conductive path would have taken place to cause PPC effect in PHBVCNT10. However, in PHBVCNT5 the PPC effect was negligible. Better dispersion and less

chances of agglomerate formation would have resulted in maintaining the conducting paths in PHBVCNT5. Resistance therefore remained almost constant.

4.3.2 Composite Resistivity

The resistivity values of all samples as a function of nanotube concentration are summarized in Figure 4.5. The value for the lowest concentration corresponds to PHBVCNT1 composite which is 1×10^{10} (Ohm-cm). For the PHBVCNT10 composite the resistivity value is 1×10^{3} (Ohm-cm). Percolation threshold is approximately at 2 wt % of MWCNT loading where resistivity starts dropping rapidly. A significant change in resistivity of PHBVCNT5 and PHBVCNT10 indicate valuable piezoresponse potential for these concentrations.

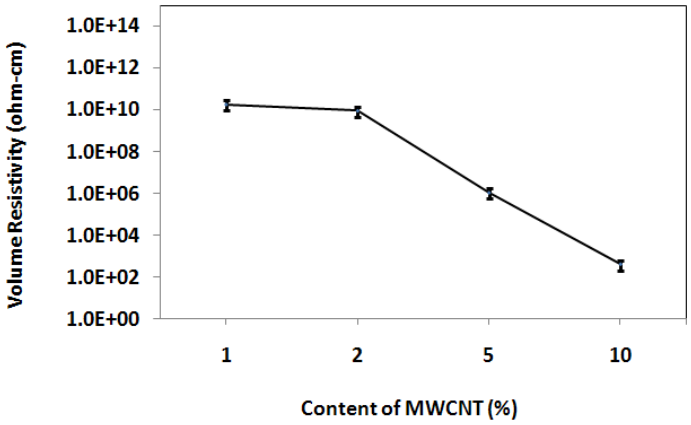

Figure 4.5 Resistivity response of PHBV/CNT nanocomposites.

4.3.3 Compressive Creep and Resistance under Transient Creep

The specimen was loaded using a mechanical test system using a stress ramp up rate of 10 MPa/sec. When the sample reached a predetermined value of stress 32 MPa, the stress was kept constant for 1 hour. The strain continued to be monitored for 1 hour following creep. Creep compliance was calculated by dividing obtained strain

values by constant stress. All the tests were performed at ambient temperature. As shown in Fig. 4.6 (a), the effect of MWCNT concentration on creep compliance can be seen. The creep compliance decreased in PHBVCNT10 compared to pure PHBV sample. Typical viscoelastic behavior of PHBVCNT10 composite was observed. Simultaneously measured resistance response for PHBVCNT5 and PHBVCNT10 is shown in Figure 4.6 (b). During initial load ramping when stress was increased at a high ramp rate (5 MPa/second) till the constant stress reached, MWCNTs came close enough to form a conductive or tunneling path leading to decreased electrical resistance. During this stage, the composite behaved in an elastic manner as the applied load was within the Hookian region.

During creep, when the applied load was constant, the material yielding response led to CNT separation competing with the axial compressive force bringing CNT in greater contact. Thus during the creep segment there was simultaneous destruction and formation of the conducting paths leading to constant resistance. Both PHBVCNT5 and PHBVCNT10 showed time independent constant resistance response under the constant loading condition.

During creep, when the applied load was constant, the material yielding response led to CNT separation competing with the axial compressive force bringing CNT in greater contact. Thus during the creep segment there was simultaneous destruction and formation of the conducting paths leading to constant resistance. Both PHBVCNT5 and PHBVCNT10 showed time independent constant resistance response under the constant loading condition.

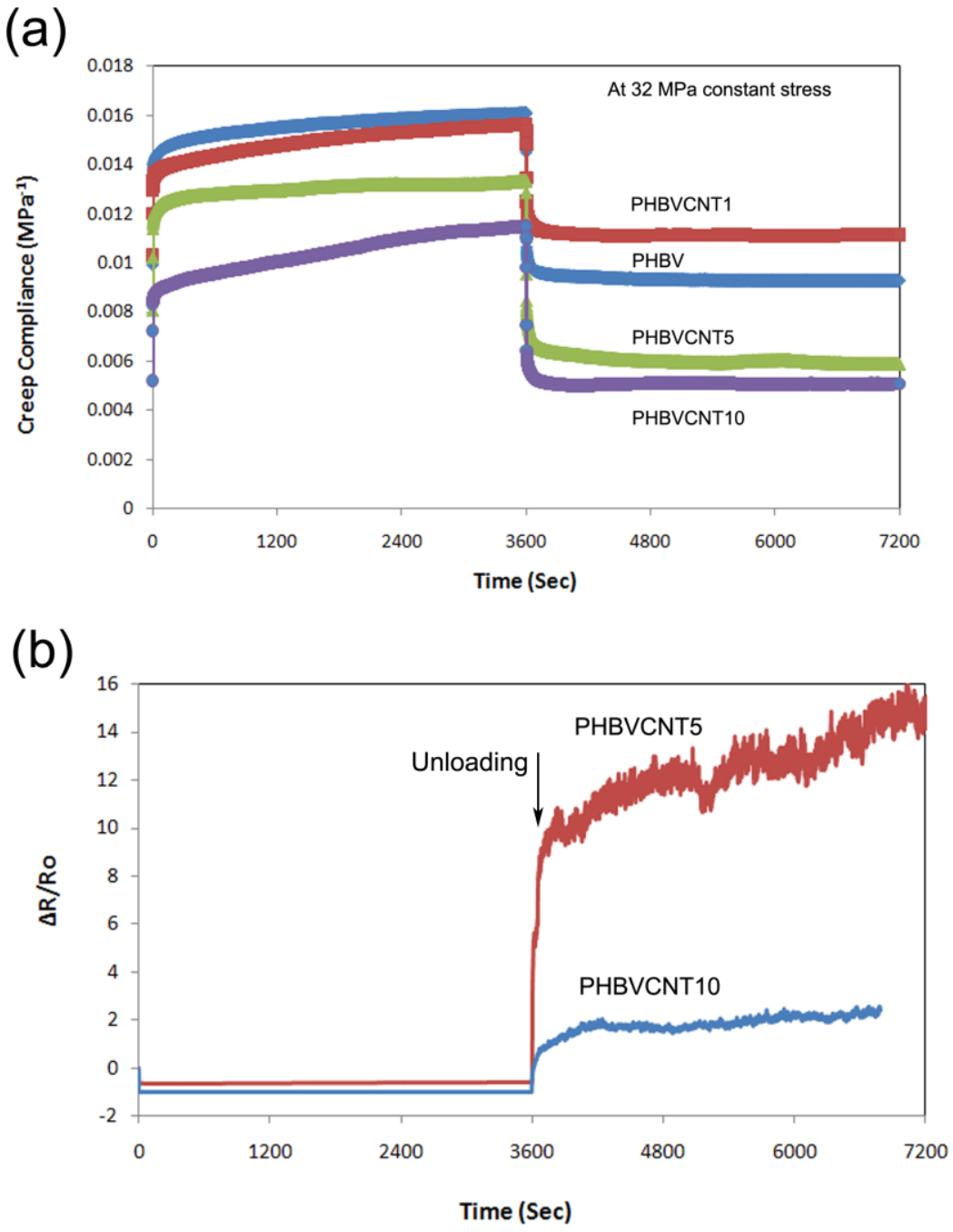

Figure 4.6 (a) Creep compliance versus time curves for PHBV/MWCNT composites and (b) time independent resistance response of PHBVCNT5 and 10 composites under constant loading.

When the load was removed (recovery following the creep), the stress was reduced to zero, a sudden increase in the resistance was observed. The absence of the constant compressive load forcing the CNT-CNT contact resulted in a domination of material flow response in this segment. The material resistance increased with further relaxation of the sample as the CNT-CNT distances increased. The lower CNT concentration (PHBVCNT5) resulted in fewer CNT-CNT contact an hour after the stress was removed compared to the higher concentration (PHBVCNT10). Thus there was increased resistance over time in the PHBVCNT5 case versus a constant permanent resistance in the PHBVCNT10 case.

4.3.4 Cyclic Loading and Electric Resistance Response of Composites

Cyclic loading was applied within the elastic limit of the sample. As shown in Figure 4.7, during the cyclic loading the specimen resistance was changed synchronously with applied stress on the sample. The increase in the resistance was observed with increasing number of cycles which was inferred to permanent residual stain built-up after each cycle of loading.

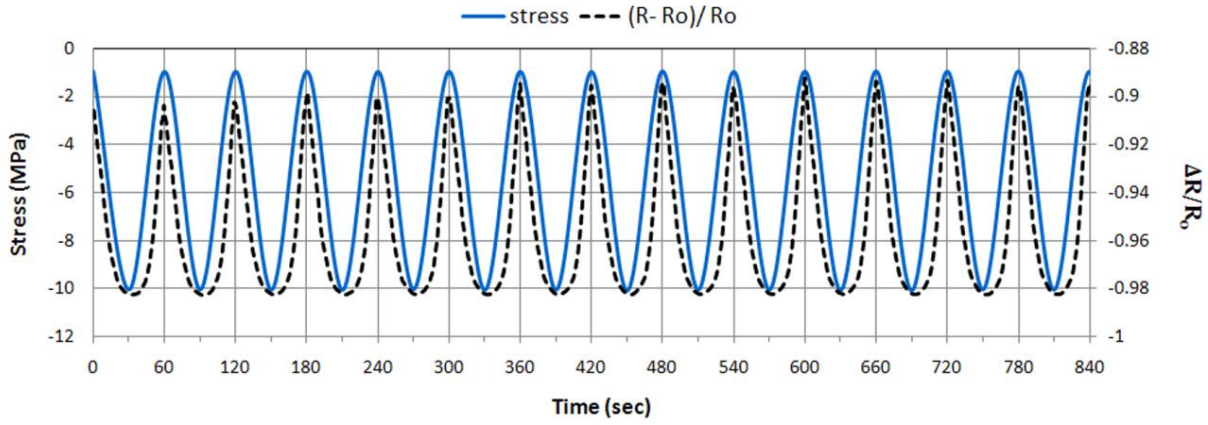

Figure 4.7 Resistance response under cyclic loading.

4.4 Conclusion

A biocompostable and biocompatible piezoresponsive nanoparticle dispersed composite was developed that can operate under transient, quasi-static, and cyclic loading. A transition from NPC to PPC behavior for PHBVCNT10 composites under compression was determined. Higher gauge factors relative to nonrenewable polymers such as PVDF were determined. The observed gauge factors for PHBVCNT5 and PHBVCNT10 composites were 6.25 and 8 respectively. Time independent piezoresistive response was observed under long term constant loading condition. PHBVCNT5 and PHBVCNT10 both showed a time independent decrease in resistance change during creep loading but when the load was removed the PHBVCNT5 composite had a gradually increasing resistance while the PHBVCNT10 had a time independent recovery. Both had a permanent remnant change in resistivity following the creep-recovery test. Under cyclic load, the stress–time and resistance–time were synchronous. These results show that these composites are viable candidates for biomedical and environmental applications.

4.5 References

[1] Vidhate S, Chung J, Vaidyanathan V, D'Souza NA. Polym Journal 2010;42:567–574.

[2] Ijima S, Ichihashi T. Nature 1993;363:603–604.

[3] Sandler JKW, Kirk JE, Kinloch IA, Shaffer MSP, Windle AH. Polymer 2003;44(19):5893-5899.

[4] Ponomarenko A, Shevchenko V, Klason C, Pristupa A. Smart Mater Structure 1994;3:409-415.

[5] Xia H, Wang Q. Chem. Mater. 2002;14:2158-2165.

[6] Mei Z, Guerrero V, Kowalik D, Chung D. Mechanical damage and strain in carbon fiber thermoplastic-matrix composite, sensed by electrical resistivity measurement. Polym. Compos. 2002;23:425-432.

[7] Song Y, Zheng Q, Yi X. J. Polym. Sci., B: Polym. Phys. 2004;42:1212-1217.

[8] Yamaguchi K, Busfield J, Thomas A. J. Polym. Sci., B: Polym. Phys. 2003;41:2079-2089.

[9] Sau K, Khastgir D, Chaki T. Die Angewandte Makromolekulare Chemie 1989;258:11-17.

[10] Pramanik P, Khastgir D, De S, Saha T. J. Mater. Sci. 1990;25:3848-3853.

[11] Vipulanandan C, Garas V. J. of Materials in Civil Engg. 2008;20:93-101.

[12] Anderson AJ, Dawes EA. Microbiol Rev 1990;54:450-472.

[13] Philip S, Keshavarz T, Roy I. J Chem Technol Biotechnol 2007;82: 233–247.

[14] Lee YH, Kang MS, Jung YM. J of Bioscience and Bioengineering 2000;89:380-383.

[15] Doi Y, Kitamura S, Abe H. Macromol. Symp. 1995;28(14):4822-4828.

[16] Kunioka M, Doi Y. Macromolecules 1990;23(7):1933–1936.

[17] Imam SH, Gordon SH, Shogren RL, Tosteson TR, Govind NS, Greene RB. Applied and Environmental Microbiology 1999;65(2):431–437.

[18] Li H, Zhai W, Chang J. J Mater Sci: Mater Med 2008;19:67–73.

[19] Poirier Y. Nature Biotechnology 1999;17:960-961.

[20] Sorrentino A, Gorrasia G, Vittoriaa V. Trends in Food Science & Technology 2007;18(2):84-95.

[21] Böger L, Wichmann MHG, Meyer LO, Schulte K. Composites Science and Technology 2008;68(7-8):1886-1894.

[22] Sementsov YI, GP, Prikhod'ko GP, Melezhik AV, Aleksyeyeva TA, Kartel MT. In: Shpak AP, Gorbyk PP, editors. Nanomaterials and Supramolecular Structures, Springer Netherlands; 2010, part 5, 347-368.

[23] Liu T, Wang X. Phys. Lett. A 2007;365:144-148.

CHAPTER 5

CRYSTALLINE/CRYSTALLINE POLYMER BLENDS

5.1 Introduction

The technology of polymer blends has been one of the major areas of research and development in polymer science in the past four decades. There are a wide range of polymer blend systems studied by researchers. The difference in polymer blend systems mainly involves phase behavior; specifically, miscibility versus phase separation [1]. Polymer blends can exhibit miscibility, phase separation, and various levels of mixing in between the two extremes. The miscibility in low molecular weight materials involves combinatorial entropy which is very high compared to in high molecular weight materials. The basic thermodynamic equation which governs the mixing of two dissimilar materials is:

$$\Delta G_m = \Delta H_m - T\Delta S_m \tag{5.1}$$

where ΔG_m is the free energy of mixing, ΔH_m is the enthalpy of mixing, and ΔS_m is the entropy of mixing. For miscibility to occur ΔG_m must be smaller than zero. Along with the above requirement, the following condition must also be satisfied.

$$\left(\frac{\partial^2 \Delta G_m b}{\partial \emptyset_i^2}\right)_{T,P} > 0 \tag{5.2}$$

Negative values of equation 5.2 can result in phase separation of two components. In low molecular weight materials increasing temperature can result in an increase in entropy which can lead to miscibility. However, for high molecular weight polymers $T\Delta S_m$ is smaller and an increase in temperature can result in non-combinatorial entropy contributions and ΔH_m values leading to immiscibility of two components. The liquid-

liquid and polymer solvent mixtures usually exhibit upper critical solution temperature (UCST) while a polymer-polymer mixture exhibit lower critical solution temperature (LCST). Figure 5.1 represents this behavior.

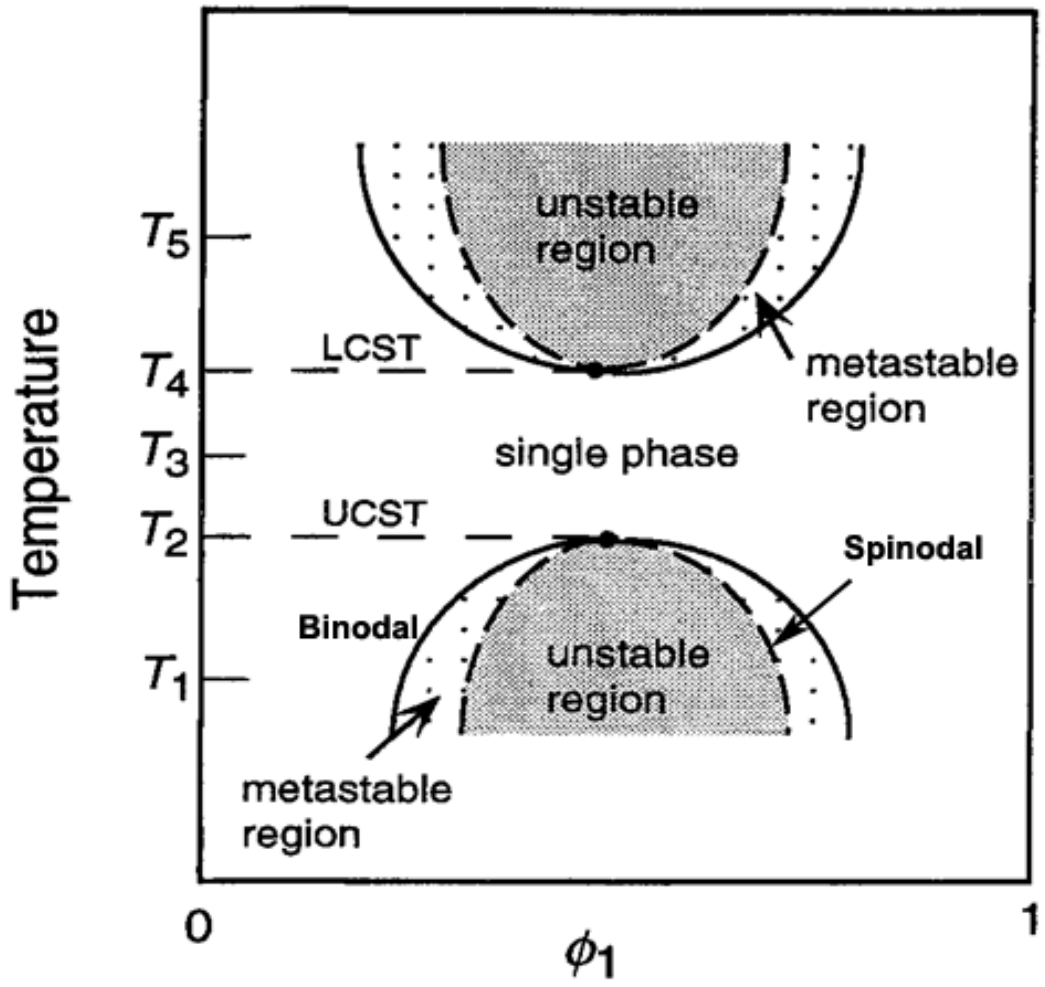

Figure 5.1 Phase diagram showing UCST and LCST behavior for polymer blends.

.

The spinodal curve shape is related to

$$\left(\frac{\partial^2 \Delta G_m b}{\partial \emptyset_i^2}\right)_{T,P} = 0. \quad (5.3)$$

The entropy of mixing can be derived from the Boltzmann relationship.

$$\Delta S_m = k \ln \Omega \quad (5.4)$$

$$\Delta S_m = -k (N_1 \ln x_1 + N_1 \ln x_2) \quad (5.5)$$

where x is the mole fraction of the components and N_1 and N_2 are the number of molecules of component 1 and 2. For a polymer mixture it was observed that the above equation did not agree frequently with experimental observation as it die for low molecular weight mixtures. Thus for a polymer, the assumption is made that the lattice is comprised of *N* cells with volume of V. Each polymer occupies volume v_1 and v_2 having volume fraction $\emptyset_1$ and $\emptyset_2$. Therefore ΔS_m leads to

$$\Delta S_m = -RV \left(\frac{\emptyset_1}{v_1} \ln \emptyset_1 + \frac{\emptyset_1}{v_1} ln\, \emptyset_2\right) \quad (5.6)$$

Enthalpy of mixing is related to w_{12} by equation

$$\frac{\Delta H_m}{V} = \frac{Z w_{12}}{v_r} \emptyset_1 \emptyset_2 \quad (5.7)$$

where z is the coordination number whose value lies between 6 and 12 and w is the exchange energy given by equation 5.8.

$$W = \frac{1}{2} \epsilon_{11} + \frac{1}{2} \epsilon_{22} - \epsilon_{12} \quad (5.8)$$

The free energy of mixing is therefore expressed by equation 5.9.

$$\Delta G_m = kT \left(N_1 + \frac{N_2 V_2}{V_1}\right) \left[\emptyset_1 ln \emptyset_1 + \emptyset_2 \left(\frac{V_1}{V_2}\right) ln \emptyset_2 + \frac{zw\emptyset_1\emptyset_2}{kT}\right] \quad (5.9)$$

The coefficient of the enthalpic term is termed Flory interaction parameter [2, 3]. The addition of functional groups on polymers which provide strong polymer-polymer interaction can make ΔH_m negative. For blends containing a copolymer of monomer segments A and B and a homopolymer of a monomer C, the net interaction parameter is given by equation 5.11.

$$\Delta H_m = \chi_{12}\phi_1\phi_2 \tag{5.10}$$

$$\phi_{ABC} = \chi\phi_{AC} + \chi_{BC}\phi_B - \chi_{AB}\phi_A\phi_B \tag{5.11}$$

This has also been proven based on the Mean Field Theory by Kambour et al. [4]. which supports the determination that the interaction parameter is negative for miscible intermolecular interactions.

The prediction of polymer-polymer miscibility based on solubility parameter (δ) can be done by following equation.

$$\frac{\Delta H_m}{N_1V_1+N_2V_2} = \left[(\delta_{d1} - \delta_{d2})^2 + (\delta_{p1} - \delta_{p2})^2\right] \emptyset_1\emptyset_2 \tag{5.12}$$

The determination of compatibility in polymer blends relies on the presence and variation in glass transition temperature across the composition. In immiscible polymer blends, individual components separate from each other and thus show two glass transition temperatures. There are also some examples of partially miscible blends exhibiting only one glass transition temperature, whose value depends on the blend composition. For such blends the Fox equation is often used which is shown in equation 5.13, and 5.14.

$$T_g = W_1T_{g1} + W_2\,T_{g2} \tag{5.13}$$

$$\frac{1}{T_g} = \frac{W_1}{T_{g1}} + \frac{W_2}{T_{g2}} \tag{5.14}$$

where W is mass fraction of polymer component.

5.2 Polymer Crystallization

The discovery of folded chain crystals by Andrew Keller in 1957 was one of the important milestones in polymer science. The basic unit of a polymer crystal is thin two dimensional lamellae separated by amorphous material. The dimensions of these lamellae are much smaller than the extended polymer chain. In polymers, due to the presence of these long chains, crystallization is a non-equilibrium process. Thus in polymers crystalline and amorphous phases coexist violating Gibbs phase rule. During the crystallization process a change in density, symmetry, and phase transition takes place which determines the properties of the final product. The initial crystallization from an entangled melt can be thought of as a kind of separation process between crystallizable and non-crystallizable polymer chains. And this process eventually forms crystalline and amorphous regions in the final crystallized polymer. Kinetic constraints on crystallization play an important role in determining final morphology. Crystallization commonly proceeds by nucleation of a fiber like structure followed by lamellar structure formation. The lamellae growth continues to form fibrils. Such fibrils grow from the point of nucleation in all directions and form spherulitic structures. Once spherulitic structures form they contuinue to grow (primary crystal growth) and impinge on each other. After this primary crystal growth there is a secondary crystal growth which takes place within the confined regions of uncrystallized melt which is secondary crystal growth. The primary crystals are more thick and regular while secondary crystals are thin, small, and less regular in structure.

5.3 Polymer Crystal Structure and Characterization

Structural order in polymers range from Å to mm lead to rich variety in morphology. Therefore characterization of the polymers is challenging and requires several techniques to characterize the whole range of length scale as shown in Figure 5.2.

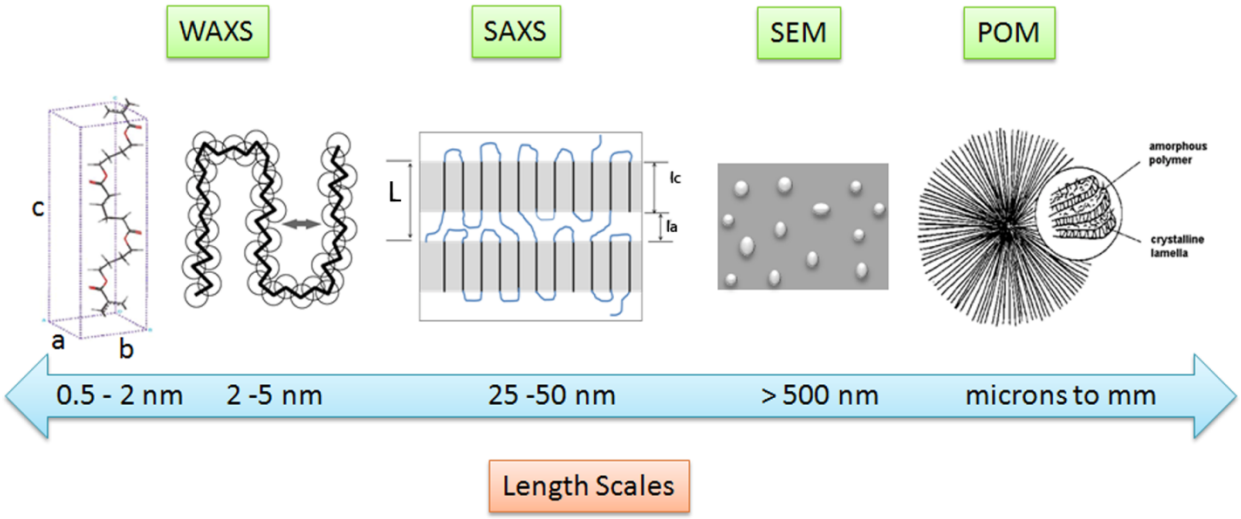

Figure 5.2 Hierarchical structural order of polymer crystal and respective characterization techniques.

Kinetic Theories of Crystallization

Many kinetic theories have been formulated to study and describe these non-equilibrium morphological features. Many researchers use the Avrami model to describe the kinetics of isothermal phase transformation. This model assumes that nucleation takes place randomly and that the crystal grows over three dimensions. Crystal volume fraction x(t) at any given time (t) can be calculated by following equation.

$$x(t) = \int_0^t v\,(t,\tau)\acute{n}(t)[1 - x(\tau)]\,d\tau \qquad (5.15)$$

where, $v\,(t,\tau)$ is volume fraction of crystallites at a given time t that was nucleated at time τ , $\acute{n}(t)$ is nucleation rate at time t. Since the polymer crystals cannot grow completely, the Avrami equation is modified to the following form.

$$\ln[1-\frac{x(t)}{x(\infty)}]=\frac{-kt^{n}}{x(\infty)} \tag{5.16}$$

where $x(\infty)$ is the crystalline volume fraction after a long period of time, k is a constant that depends upon the nucleation and growth rate, n is the "Avrami exponent" which takes value from 1 to 4 depending on the nature of crystallization. The various Avrami exponents associated with different crystal geometries and nucleation type [5]are shown in Table 5.1.

Table 5.0.1 Avrami exponent and for various types of crystal geometry, nucleation type.

Avrami Exponent	Crystal Geometry	Nucleation Type	Rate Determination
0.5	Rod	Athermal	Diffusion
1	Rod	Athermal	Nucleation
1.5	Rod	Thermal	Diffusion
2	Rod	Thermal	Nucleation
1	Disc	Athermal	Diffusion
2	Disc	Athermal	Nucleation
2	Disc	Thermal	Diffusion
3	Disc	Thermal	Nucleation
1.5	Sphere	Athermal	Diffusion
2.5	Sphere	Thermal	Diffusion
3	Sphere	Athermal	Nucleation
4	Sphere	Thermal	Nucleation

But before using the Avrami model and utilizing the interpretations of it based on 'K' and 'n', it is important to know the assumptions of Avrami equation and the inherent

problems related to it [6, 7]. The problems associated with Avrami model are enlisted below.

- Constant radial growth of spherulite and fixed shape (rod/disc/sphere) of growth has been assumed.
- Analysis does not account for induction time.
- Complete crystallinity of sample is assumed.
- Considered primary crystallization only.
- Radial density of crystal considered constant which has not been observed experimentally.

Thus, the phenomenological based Avrami model cannot explain the experimental observations and crystallization kinetics such as crystal growth, dependence of melting temperature on crystallization temperature, etc. Therefore, independent microscopic investigation is critical before assigning 'K' and 'n' to particular features of crystallization.

The surface nucleation theory [8] of Lauritzen and Hoffman can help to understand and predict several experimental observations of crystallization. According to this theory polymer chains from the melt come in contact with the growing face of lamella and form secondary nuclei. The growth rate of lamella, g, at temperature T is given by equation:

$$g = g_0 \exp\left[\frac{-U}{K_b T}\right] \exp\left[\frac{-K_g}{T\Delta T f}\right] \tag{5.17}$$

where, g_0 is constant, $\frac{-U}{K_b T}$ term is associated with transport of polymer chains to the crystal surface, K_g is temperature independent term, ΔT is the subcooling and f

accounts for variation in the heat of fusion with temperature. The regime transitions in Lauritzen and Hoffman theory are highly dependent on equilibrium melting temperature, T_m^0. The equilibrium melting temperature is defined as the melting point for infinite chain crystals where the polymer chain ends have been paired as in the case of crystallization in small molecules. However, such equilibrium crystals can never form. Therefore T_m^0 has to be estimated by extrapolation. This nucleation theory is based on the assumption that the difference between melting and crystallization temperature is due to crystal thickening at the crystallization temperature. This forms the basis for Hoffman-Weeks method to determine T_m^0. In this method a plot of melting temperature Vs crystallization temperature can be conveniently used to determine the T_m^0.

5.4 Crystallization in Polymer Blends

Crystallization in polymer blends can take place in various ways resulting in various supermolecular structures. The formation of structure depends on whether the polymers are miscible within the temperature range of both component melting points and composition range, whether they exhibit a miscibility gap, or whether they are immiscible over all the conditions. The crystallization process in these three miscibility conditions have been discussed below:

5.4.1 Complete Immiscible Blends [9, 10]

On mixing of two immiscible polymer components they phase separate and stay side by side after crystallization. The two different phases exist as two separate pure components and show composition dependent overall melting and crystallization behavior. However, the crystallization mechanism can be altered due to the interface between two components or one of the components acting as a nucleating agent for the

other component. In some cases both the blend components may crystallize at the same time when the minor component is finely dispersed in the other component. Sometimes the continuous phase can also form droplets to act as the dispersed phase like the minor component. In such a case the major component can exhibit fractionated crystallization. i.e. crystallization at different temperature. Fractionated crystallization can be enhanced by the addition of compatibilizer or by increasing the mixing time while processing which causes a reduction of droplet size. The reduction in the droplet size reduces the surface area of the droplet and thus affects heterogeneous nucleation. Polymers have a high molecular weight. During mixing of two or more polymers, unlike low molecular weight compounds, polymers do not show very high entropy of mixing even if they are chemically identical. Yet within crystalline polymers, the higher order afforded by the crystalline region results in a lower entropy of mixing contribution. Highly crystalline phases are thus more likely to phase separate from less crystalline or amorphous phases [11].

5.4.2 Crystallization in Blends with Miscibility Gap [12]

In phase separated crystallizing components, the component with more crystallinity will start crystallizing first. The crystallization spreads over the whole phase. After complete crystallization of that phase the crystallites reach to the interface and induce the crystallization of other phase. The crystallization of other phase takes place which looks completely different from the first one. This kind of interface crossing crystallization can lead to interesting morphological structure and can show positive effect on improved mechanical properties of the blend due to better adhesion between two components.

5.4.3 Crystallization in Miscible Blends [9-12]

In blends of two crystalline polymers, the kinetics of crystallization of one polymer can be hindered by the crystallization or presence of the other polymer. Thus a reduced melting temperature of the blend is observed. There are very few polymer blend systems of crystalline polymers which show miscibility at the whole range of temperature and composition. Examples are PVDF/PHB, PC/PCL, PET/PBT, PHB/PEO blend systems. Simultaneous crystallization of the polymers results in interpenetrating spherulites. It is well know that spherulites of the same polymer stop growing when they meet their own spherulites but in case of spherulites of the different polymers they interpenetrate and grow into each other. The spherulites of the two components then grow successively. The fast growing and highly crystalline component may fill the whole volume. The structural features of these miscible blends can be analyzed by small angle X-ray scattering (SAXS). The change in the lamellar morphology can be observed using SAXS that can be correlated to the miscibility of a polymer pair.

5.5 Crystalline/Crystalline Polymer Blends

In the next section various crystalline/crystalline polymer blend systems investigated in the past have been reviewed.

Poly(vinylidene fluoride) (PVDF)/Poly(1,4-butylene adipate) (PBA) Blends

For the miscible blend of PVDF and PBA Penning et al. [7] determined that both components were capable of crystallizing over a full range of compositions. Co-crystallization did not occur due to well separated melting and crystallization temperature regimes. Therefore, the crystallization of each component resulted in a phase separation process in which the polymers were partially segregated from the

mixture to form a pure phase. During the crystallization of PVDF, the PBA acted as a noncrystalline diluent which reduced the spherulitic growth rate as well as the overall crystallization rate of the PVDF phase. Also, PBA affected the spherulitic texture of PVDF and facilitated the formation of PVDF polymorph.

Poly(butylene terephthalate) (PBT)/Polyarylate bisphenol A isophthalate [PAr(I-100)] Blends

Liu et al. [13] studied the miscibility and crystallization behavior of PBT and PAr(I-100) binary crystalline blend system. This crystalline/crystalline blend showed composition dependent T_g-temperature relationships such as the Fox relation to confirm miscibility of the blend system over entire range. Further, the PBT and PAr could form the crystals at the same temperature for 50/50 blend but they did not form the cocrystal as evidenced by a single recrystallization temperature. Using thermal analysis, they showed that the crystallization of PAr(I-100) was much faster when a small amount of PBT was added. This was explained as being due to the increasing segmental mobility or plasticization of the high Tg component by addition of low-T_g components. However, the presence of crystallites of PBT in the blend suppressed the crystallization of PAr(I-100).

Poly(ethylene oxide) (PEO)/Poly(ethylene succinate) (PES) Blends

H-L Chen et al. [14] investigated the crystallization kinetics and semicrystalline morphology of PEO/PES blend. Morphological structures can be controlled by modifying the crystallization kinetics. The dilution of PES by PEO enhanced segmental mobility and increased crystallization rate. When PEO content was further increased the crystallization rate of the PES was reduced due to dominant dilution effect. SAXS

studies for crystalline amorphous state of PEO and PES revealed that there was significant amount of interfibrillar segregation of amorphous PEO and for crystalline/crystalline state, two separate lamellar stack domains were observed, where one contained pure PES lamellae and the other contained mixed PEO and PES lamellae.

Poly(vinylidenefluoride) (PVDF)/Poly(1,4-butylene adipate) (PBA) Blends

Liu et al. [15] studied PBA crystallization behavior within the PVDF spherulites of PBA/PVDF miscible blends using small-angle X-ray synchrotron scattering (SAXS). The incorporation of PBA into the PVDF interlamellar region was found to be dependent on the PVDF crystallization conditions. Three recrystallization temperature regions emerge when dealing with two crystalline melts. At temperatures above that of the higher melting point polymer, the microstructure is completely amorphous and an amorphous/amorphous blend exists. At temperatures between the melting point of the lower melting polymer and the higher melting polymer, a crystalline/amorphous mixtures will exist. Finally at temperatures below that of the lowere melting system, a semicrystalline/semicrystalline mixture will exist. Thus by changing the crystallization paths through isothermal recrystallization temperature selection, onditions the PBA (which was the lower melting component) component can be introduced into interlamellar, interfibrillar or interspherulitic regions. The crystallization behavior and crystalline morphology of the PBA component in the PVDF interlamellar region also changed with the blend composition.

Poly(vinylidenefuoride) (PVDF)/Poly(3-hydroxybutyrate) (PHB) Blends

H. J. Chiu et al. [16] studied the lamellar morphology of a melt-miscible blend consisting of PVDF and PHB using small angle X-ray scattering (SAXS). SAXS pattern revealed the presence of lamellar stacks of PVDF and PHB domain. The interlamellar regions of both lamellar stack (LS) domains were found to contain mixed amorphous PVDF and PHB. Further crystallization kinetics played an important role in the microstructure of the lamellar stacks domains. At a high crystallization temperature where PHB was basically an amorphous diluent of PVDF, PHB is expelled from between the PVDF lamella stacks. (e.g. the μm scale) during the crystallization of PVDF, so that the sequential stacking of PVDF lamellae extends over a long distance. Large PVDF LS domains are thus created.

Poly(3-hydroxybutyrate) (PHB)/Poly(ethylene oxide) (PEO) Blends

Jiang-Wen You et al. [17] studied the spherulitic morphology and crystallization kinetics of PHB/PEO blends prepared by the solution casting by differential scanning calorimetry (DSC) and polarized optical microscopy (POM). The blends of PHB with low molecular weight PEO were found to be miscible in the melt. Sequential crystallization of PHB and PEO was observed at 70 ^{o}C. Banded spherulitic texture of PHB was perturbed by subsequent crystallization of PEO. When PHB/PEO blend was quenched from melt to room temperature fairly competitive crystallization emerged where crystallization and segregation of PHB and PEO occurred simultaneously, leading to a complicated spherulitic morphology.

Poly(butylene succinate) (PBSU)/Poly(ethylene oxide) (PEO) Blends

Z. Qiu et al. [18] found PBSU/PEO blend miscible based on the existence of single composition dependent glass transition temperature over the entire composition

range. Also, thermodynamic miscibility was studied using the Flory-Huggins equation. The depression of melting temperature was found to be composition dependent and interaction parameter values were always negative. In their further studies of PBSU/PEO blend Z. Qiu et al. [19] studied the influence of the blend composition, crystallization temperature, and scanning rate on the melting behavior of PBSU. The recrystallization of PBSU was observed to be restricted by either of increasing a) the PEO in blend composition, b) scanning rate, or c) crystallization temperature.

Immiscible Poly(ethylene oxide) (PEO)/Poly(1-caprolactone) (PCL) and Poly(butylene succinate) (PBSU)/Poly(1-caprolactone) (PCL) Blends

Z. Qiu et al. [20] studied the miscibility and crystallization of PEO/PCL blends by phase contrast microscopy (PCM) and DSC. PCM study showed that PCL is immiscible with PEO. The crystallization rate of the PEO decreased with increase of PCL in the blends due to physical restriction by the PCL domains. However, the crystallization mechanism of PCL did not change with PEO. Also, Z. Qiu et al. [21] found immiscibility of PBSU/PCL based on the composition independent glass transition temperature and the biphasic melt.

Poly(butylene succinate-co-butylene carbonate) (PEC)/poly(L-lactic acid) (PLLA) blends

Ikehara et al. [22] observed the spherulitic morphology in PEC/PLLA AFM to obtain direct evidence for the formation of inter-penetrating spherulites (IPS) i.e. spherulites of one component crystallized inside the spherulites of the other component. It revealed that PEC crystals penetrated between edge-on fibrils of a PLLA spherulite.

Poly(1,4-butylene succinate) (PBSU) in the Oriented Blend with Poly(vinylidene fluoride) (PVDF)

The PBSU/PVDF blend was reported to be a miscible crystalline/crystalline blend based on remarkable decrease in the melting temperature upon blending of the two components [23]. Li et al. [24] studied the crystal orientation and the lamellar textures of PBSU/PVDF (30/70) blend using WAXD, SAXS, and TEM and correlated the results with mechanical properties of the blend. They concluded that the morphology of the miscible blend is segregated into the fibrillar morphologies of PBSU and PVDF, forming a periodic structure with a long period of 50 nm perpendicular to the stretching direction. The TEM studies revealed that PBSU-rich domains dispersed in the PVDF-rich matrix were elongated into ribbon like domains with a width of 20-50 nm, which was consistent with the SAXS and WAXD results.

Poly(vinylidene fluoride) (PVDF)/poly(3-hydroxybutyrate-co-hydroxyvalerate) (PHBV) blends

Based on single T_g Zhaobin et al. [25] showed miscibility of PVDF/PHBV blend over entire range. They observed spherulitic morphology of PHBV was influenced significantly by the presence of the pre-existing PVDF crystals. The spherulitic growth rate of PHBV decreased with increasing PVDF and increased with the crystallization temperature.

Poly(butylene adipate-*co*-butylene succinate) (PBAS)/Poly(ethylene oxide) (PEO) Blends

Ikehara et al. [26] observed the interpenetrating spherulites growth of PBAS and PEO components in their miscible blends. The growth of the PEO lamellae took place along the preexisting PBAS lamellae. They described the conditions for interpenetrating spherulite formation as follows: 1) The difference in T_m of the two constituents must be

sufficiently small so that they can crystallize simultaneously, 2) The content of the higher T_m component should be smaller than that of the lower T_m component, 3) The spherulites of penetrated (host) component must contain a sufficient amount of interlamellar amorphous regions that contain an adequate quantity of the penetrating (guest) component.

Poly(vinylidene fluoride) (PVDF)/Poly(butylene succinate-*co*-butylene adipate) (PBSA) Blends

Zhaobin et al. [27] proved PVDF/PBSA blends as a miscible blends based on the decrease of crystallization peak temperature and melting point temperature of each component with increasing the other component content and the homogeneous melt. Individual component fraction and crystallization condition dependent three different morphological structures of PVDF/PBSA were observed: 1) Crystallization of PBSA in the interspherulitic regions of the PVDF spherulites, 2) Formation of PBSA spherulite in remaining space after PVDF's complete crystallization, 3) PBSA spherulites nucleated and continued to grow inside the PVDF spherulites. In another work of Zhaobin et al. [28] studied the spherulitic morphologies and overall crystallization kinetics of miscible PVDF/PBSA blends by POM, DSC, and WAXD. Independent crystallization of PVDF and PBSA was observed due to large difference in melting temperatures and the two components could not crystallize simultaneously. The WAXD pattern showed no effect on crystalline structure of the individual components in the blend and also indicated that the individual components crystallize separately. The intensity of the characteristic peaks of individual components increased with their fraction in blend.

POM results indicated decrease in crystallization with increase in the crystallization temperature despite blend composition. Overall crystallization rate of the blends increased due to nucleation effect of PVDF at low concentration and lower crystallization rate at high concentration of PVDF due to a dilution effect which reduced the number of crystallizable units at the crystal growth front.

Poly(butylene succinate) (PBSU)/Poly(ethylene oxide) (PEO) Blends

Takayuki et al. [29] studied the spherulitic growth rate of PEO inside PBSU spherulites of PBSU/PEO blends. They showed PBSU contains wide amorphous region and PEO crystallizes primarily in interfibrillar regions in PBSU spherulites. Also, the spherulitic growth rate of PEO decreased with crystallization temperature and increased with PEO fraction in blend.

Poly(ethylene succinate) (PES)/Poly(ethylene oxide) (PEO) Blends

A single Tg across the composition range in PES/PEO inferred miscibility [30]. Lu et al. [31] observed the composition and crystallization condition dependent sequential and simultaneous crystallization of PES/PEO blends. Here they proposed that the density of lamellae in PES spherulites was lower than that in PEO spherulites, and PEO spherulites continued to penetrate into PES spherulites on contact. In their further work [32] they studied the effects of PES/PEO blend composition and crystallization temperature on the crystalline morphologies of PES/PEO by optical microscopy. At some compositions (which) and crystallization temperatures PEO fibrils grew faster inside the amorphous regions of the PES spherulites due to presence of high concentration of PEO in PES crystals. Also they observed, during the growth of PEO fibrils in PES spherulites, PEO fibrils do not keep their original direction of growth but

change their growth direction along PES fibrils. Other novel crystalline morphologies were interpenetrated spherulites and nucleation of PEO and PES spherulites from the same site.

Poly(butylene adipate) (PBA)/Poly(vinylidene fluoride) (PVDF) Blends

Yang et al. [33] investigated the effect of the PVDF component on the crystallization kinetics, crystalline structure, phase transition, and morphology of polymorphic poly(butylene adipate) (PBA) in their miscible PVDF/PBA binary blends. They observed composition dependent melting temperature, crystallization temperature, and a single glass transition temperature. The addition of a small amount of PVDF (~10%) increased the crystallization rate acting as a nucleating agent for PBA. But addition of a large % of PVDF decelerates the crystallization process as the solidified matrix of PVDF provided many confined and restricted spaces to hinder the crystallization of the PBA component. Similarly, increased transition rate of α phase PBA into β phase PBA was observed at low % loading of PVDF while at high % loading of PVDF the same transition rate decreased.

Poly(ethylene succinate)(PES)/Poly(*p*-dioxanone)(PPDO) Blends

Zing et al. [34] reported the miscibility and crystallization behaviors of (PES/PPDO) blends. From a single glass transition temperature and decreased crystallization temperature in comparison with the respective component of the blends they found blends were completely miscible. The T_g values of the blends were increased with an increase in the volume fraction of the PES. The T_g values obtained by using Fox equation ($1/T_g=W1/T_g1. + W2/T_g2$) and by DSC experimentation were close to each other. But as the difference between the glass transition temperatures of the

two polymers was less than about 4 ^{o}C, the T_g result provided partial explanation for miscibility of blends. Increase in the cold crystallization temperature of the blend indicates the poor crystallization and indicates miscibility of the two components. They also observed increased crystallization temperature and decreased melting temperature of all the blends compared with both neat PES and PPDO. POM observation for 50/50 composition of the blend showed interpenetrating growth of the PES and PPDO spherulites. Isothermal crystallization revealed slow crystallization rate of the blends and WAXS study indicated no change in the crystal structures of the PES and PPDO.

Poly(ε-caprolacton) (PCL)/ Poly-L-Lactide (PLLA) Blends

Biocompatible PCL/PLLA is a typical immiscible blend which has been widely investigated in order to formulate it into practical applications [35, 36]. Aliphatic polyesters represent an important family of biodegradable materials. It has been reported that the addition of PCL enhanced the cold crystallization of PLLA, while there was little effect on the melt crystallization [37, 38]. The addition of PCL even at low% can cause enhanced nucleation. Rusa et al. [39] reported that the crystallization rate of the PLLA can be promoted by the addition of PCL. However, the crystallization rate of PLLA does not increase monotonically with increasing PCL composition. Since the glass transition temperature of PLLA cannot be identified directly from the thermogram (melting point of PCl is 60 and Tg of PLLA is 65 causing overlap), T_g criteria cannot to be used to judge the miscibility between PLLA and PCL. So, on the basis of polarized optical microscopy where birefringence and phase separation occurred; immiscible behavior and compatibility of PLLA/PCL blends have been shown. Maglio et al. [40] demonstrated that for immiscible blends the use of a very efficient corotating twin screw

miniextruder with a retrofeeding channel system enhances the dispersion of the minor component in the matrix and minimizes coalescence. Castillo [41] investigated the crystallization kinetics and morphology of PLLA and PCL blends. He reported, both T_c and T_m of PLLA blocks were depressed with PCL content because of a diluent effect, caused by the miscibility or partial miscibility of both phases. The crystallization kinetics of the PLLA blocks decreases due to PCL. An Avrami analysis of the data indicated that 3D superstructures were formed from instantaneous nuclei (n= 2.5 to 3). The phase separation behavior was observed by DSC, DMA, and SEM. Miscible PCL/PLLA blend can be obtained at low molecular weights. According to Lopez Rodriguez et al. [37] PCL/PLLA has similar solubility parameter (10.1 and 9.2 $cal^{0.5}/cm^{1.5}$) but lack of specific interaction between PCL and PLLA could contribute to the immiscibility of this polymer pair. Wu et al. [42] reported on the rheological behavior of PLLA and PCL. PLLA showed pseudoplastic behavior while PCL showed Newtonian behavior in the regime 60 to 70 ^oC. They observed the variation in dispersed phase due to difference in viscosities. Improved mechanical properties were observed in these compatible blends. The melting and crystallization behavior of crystalline/crystalline polymer blends has been summarized in Table 5.2.

Table 5.2 Melting and crystallization behavior of crystalline/crystalline polymer blends.

Polymer 1	Polymer 2	T_{g1}	T_{g2}	$T_{g\ blend}$	T_{m1}	T_{m2}	$T_{m\ blend}$	$T_{recryst\ 1}$	$T_{recryst\ 2}$	$T_{recryst\ blend}$	Remark
PVDF	PBA	-45	-55	Single	175	55	Single	125	25	120	Miscible
PVDF	PBSU	-40	-37	Single	165	116	Double	145	86	125/85	Miscible
PVDC	PBSU	7	-40	Single	115	148	Double	-	-	-	Miscible
PBT	Par	38	180	Single	250	380	Single	-	-	-	Miscible
PEO	PES	-55	-10	Single	62	100	Double	58	44	40	Miscible
PHB	PEO	2	-80	Single	170	60	Single	64	35	65	Miscible
PBSU	PEO	-32	-55	Single	115	67	Single	83	45	85	Miscible
PEO	PCL	-54	-60	Single	62	68	Single	36	46	26/48	Immiscible
PBS	PCL	-34	-66	Double	118	60	Single	92	35	91	Immiscible
PEC	PLLA	-26	40	-	106	140	-	-	-	-	Miscible
PVDF	PHBV	-35	-1	Single	171	150	Single	-	-	-	Miscible
PBAS	PEO	-54	-63	Single	98	67	Double		-		Miscible
PVDF	PBSA	-43	-44.8	-	170	98	Single	140	52	138	Miscible
PBSU	PEO	-32	-60	Single	114	67	Single	-	-	-	Partially Miscible
PBSU	PCL	-34	-66	-36	118	60	Double	26	85	83	Immiscible
PCL	PLLA	-36.8	70.1	-37.2	60	179	Single	-	-	100	Immiscible
PES	PPDO	-12.8	-8.6	-	102	105	Single	-	-	-	Miscible

5.6 References

[1] Robeson MI, Lloyd M. Polymer Blends (Hanser gardner Publication, Munich) 2007;Chapter 1:pp 3.

[2] Flory PJ. J Chem Phys 1941, 9, 660.

[3] Flory PJ. J Chem Phys 1941, 9, 660.

[4] Kambour RP, Bendler JT, Bopp RC. Macromolecules 1983;16,753.

[5] Hiemenz PC. Polymer Chemistry: The Basic Concepts Marcel Dekker, New York, 1984, pg. 219.

[6] Grenier D, Homme RE. J Poly Sci Part B 1980;18:1655.

[7] Tomka J. Eur Poly J 1968;4:237.

[8] Marand H, Hoffman JD. Macromolecules 1990;23:3682.

[9] Anastasiadis SH, Gancarz I, Koberstein JT. Macromolecules *1988;*21:2980–2987.

[10] Favis BD, Therrien D. Polymer 1991;32:1474-1481.

[11] Penning JP, Manley J. Macromolecules 1996;29:84-90.

[12] Horst R, Wolf BA. *Macromolecules* 1993;26:5676–5680.

[13] Liu AS, Liau WB, Chiu WY. Macromolecules 1998;31:6593-6599.

[14] Chen HL, Wang SF. Polymer 2000;41:5157–5164.

[15] Liu LZ, Chu B, Penning JP, John RS, Manley J. Journal of Polymer Science Part B: Polymer Physics 2000;38:2296–2308.

[16] Chiu HJ, Chen HL, Lin JS. Polymer 2001;42:5749-5754.

[17] You JW, Chiu HJ, Don TM. Polymer 2003;44:4355–4362.

[18] Qiu Z, Ikehara T, Nishi T. Polymer 2003;44:2799–2806.

[19] Qiu Z, Ikehara T, Nishi T. Polymer 2003;44:3095–3099.

[20] Qiu Z, Ikehara T, Nishi T. Polymer 2003;44:3101–3106.

[21] Qiu Z, Komura M, Ikehara T, Nishi T. Polymer 2003;44:7749–7756.

[22] Kim J, Ryba E, Bai JM. Polymer 2003;44:6657–6661.

[23] Lee JC, Tazawa H, Ikehara T, Nishi T. Polym J 1998;30:327.

[24] Fujita K, Kyu T. Macromolecules 2004;37:2119-2127.

[25] Qiu Z, Fujinami S, Komura M, Nakajima K, Ikehara T, Nishi T. Polymer 45 (2004) 4355–4360.

[26] Ikehara T, Kimura H, Qiu Z. Macromolecules 2005;38:5104-5108.

[27] Qiu Z, Yan C, Lu J, Yang W, Ikehara T, Nishi T. J Phys Chem B 2007;111:2783-2789.

[28] Qiu Z, Yan C, Lu J, Yang W. Macromolecules 2007;40:5047-5053.

[29] Ikehara T, Kurihara H, Qiu Z, Nishi T. Macromolecules 2007;40:8726-8730.

[30] Chen H, Wang S. Polymer 2000;41:5157.

[31] Qiu Z, Ikehara T, Nishi T. Macromolecules 2002;35:8251.

[32] Qiu Z , Yan C, Lu J, Yang W. Macromolecules 2008;41:141-148.

[33] Yang J, Pan P, Hua L, Zhu B, Dong T, Inoue Y. Macromolecules 2010;43:8610–8618.

[34] Zeng JB, Zhu QY, Li YD, Qiu Z, Wang YZ. J Phys Chem B 2010;114:14827–14833.

[35] Ikada Y, Tsuji H. Macromol. Rapid Commun. 2000;21:117.

[36] Tsuji H, Horikawa G. Polym. Int. 2007; 56:258.

[37] Lopez-Rodrı´guez N, Lopez-Arraiza A, Meaurio E, Sarasua J. R. Polym. Eng. Sci. 2006;46:1299.

[38] Dell'Erba R, Groeninckx G, Maglio G, Malinconico M, Migliozzi A. Polymer 2001;42:7831.

[39] Rusa CC, Tonelli AE. Macromolecules 2000;33: 5321-5324.

[40] Maglio G, Malinconico M, Migliozzi A, Groeninckx G. Macromol. Chem. Phys. 2004;205: 946–950.

[41] Castillo R. Macromolecules 2010;43:4149–4160.

[42] Wu DF, Zhang YS, Zhang M, Zhou WD. Eur Polym J 2008;44:2171–2183.

CHAPTER 6

MISCIBILITY, CRYSTALLIZATION, AND MELTING BEHAVIOR OF PHBV/PBAT CRYSTALLINE BLENDS

6.1 Introduction

Polymer blending has remained an economical and effective choice for improving the mechanical and physical properties of polymers [1, 2]. To date more than 29000 scientific articles have been published in various journals regarding various aspects of the polymer blends. The polymer blend preparation changes the structure property relationship of the blend components and ultimately causes change in various properties of the mixture. Macroscopic properties of the multi-component polymer blend largely depend on the microscopic properties like morphological structure of the blend, amorphous and crystalline nature of the individual component, interface between different phases, crystallization of different components, molecular interaction, etc. In short, the final blend properties depend on whether the blend is miscible, immiscible, or partially miscible. Many polymer blends made from synthetic and natural polymers have been successfully prepared, studied, and commercialized all over the world for a broad range of applications.

Miscibility, crystallization, morphology, of the polymer blends have been studied extensively. Most of the studied polymer blend systems represent mixing of two amorphous polymers or mixture in which one of the components is amorphous. However, blends in which both components are crystalline polymers have received much less attention. Both PHBV and PBAT are crystalline polymers. Investigating the crystalline/crystalline blend is more complicated and provides an opportunity to study

the crystallization behavior, miscibility, and morphological structure [3-11]. The difference between the melting points (T_m) of the two polymers plays an important role in the crystallization behavior of their blend. When the T_m difference between the two components is small enough, they usually crystallize simultaneously. Thus the polymer components which crystallize simultaneously can form unique interpenetrated crystalline morphologies. The difference between the T_m, T_c, and T_g of PHBV and PBAT is ~ 40, 12, and 43 ^oC respectively. Even though the T_m and T_g difference of two polymers is quite high, the T_c difference is low enough that both polymers can undergo co-crystallization. Also, in the crystalline/crystalline polymer blends, it is important to know how the crystallinity of one polymer affects the crystallization of other. So in this work it was expected that crystalline PHBV/PBAT blend can provide a blend system with intriguing phase behavior, crystallization kinetics, and crystalline morphologies.

Objectives

The purpose of this work was to investigate the miscibility, crystallization, and melting behavior of PHBV/PBAT blends. In this work, the blends of PHBV/PBAT were prepared by melt mixing. The isothermal and non-isothermal crystallization and melting behavior of the blends was studied by isothermal and non-isothermal differential scanning calorimetry (DSC). The crystalline structure and lamellar thickness of PHBV/PBAT blends were studied by wide angle X-ray diffraction (WAXD) and small angle X-ray scattering (SAXS) respectively. PHBV-PBAT phase interaction was studied by contact angle method. The phase and spherulitic morphologies of the PHBV and PBAT components in this blend system were observed by scanning electron microscopy (SEM) and polarized optical microscopy (POM).

Crystallization, miscibility, effect of blending on morphology are discussed in this chapter. Figure 6.1 shows the flow chart of experimentation.

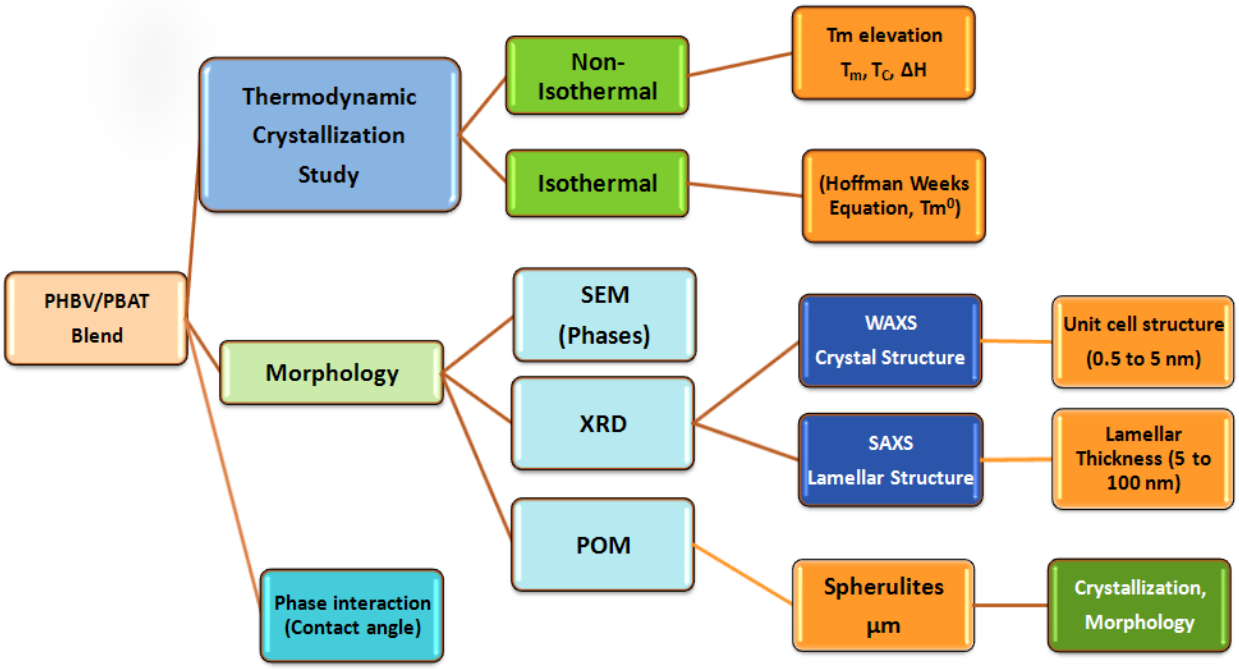

Figure 6.1 Flow chart of experimentation

6.2 Experimental

6.2.1 Materials

PHBV (Enmat® -Y1000) was supplied by Tianan Biologic Material Co., Ltd. The hydroxyl valerate (HV) content in PHBV is 3 %. PBAT is available under the trade name of Ecoflex® F BX 7011 was supplied by BASF. Ecoflex® is an aliphatic-aromatic copolyester based on terephthalic acid, adipic acid, 1,4- butanediol and modular units. This copolyester contains 44 mol% of BT.

6.2.2 Blend Preparation

PHBV was dried at 70 ^{o}C for 3 hours before melt blending with PBAT. PBAT was used as received as predrying before melt processing is not required for PBAT. The processing was done at 190 ^{o}C, 70 rpm (counter rotating blades), and 5 min mixing time. The compounded blend compositions were then cryo-grinded to obtain the blend in powder form. The following blend compositions were prepared and labeled as mentioned: PHBV100, PHBV90, PHBV80, PHBV70, PHBV60, PHBV50, PHBV40, PHBV30, PHBV20, PHBV10, and PHBV0. In PHBVx, x indicates wt % of PHBV component in the blend and (100 – X) is the PBAT wt %.

6.2.3 Film Preparation in Carver Compression Press

To facilitate the dynamic mechanical analysis (DMA) testing (Chapter 7), wide angle X-ray (WAXD) diffraction, and small angle X-ray scattering (SAXS) characterization, film samples of the blend compositions were prepared using a compression press. All the films were prepared simultaneously in one molding cycle to obtain samples with the same thermal history. In this process the powder samples were preheated at 170 ^{o}C for 10 min considering the heating rate of the metal mold and the

time to heat transfer through Teflon sheets. After preheating, three tons of compressive pressure for 5 min was applied gradually to form uniform films. In the cooling cycle, the films' temperature was suddenly dropped to 80 ^{o}C and kept constant for two hours to ensure slow and extended crystallization of the blends. After two hours the mold was cooled to room temperature and the samples were removed from the mold. The prepared samples were kept for two days at room temperature for conditioning and then used for characterization.

6.2.4 Characterization

6.2.4.1 Differential Scanning Colorimetry (DSC)

Thermal transitions were determined using a Perkin–Elmer DSC6 (Norwalk, CT, USA). A temperature calibration was performed before doing the actual tests using indium (T_m= 156.6 °C, ΔH_f=28.5 J/g). A heating rate of 10 °C/min and an inert atmosphere of nitrogen were used during all the testing. Approximate 5 mg of each sample was used for testing. The samples were first heated from 20 to 190 °C and maintained at 190 °C for 5 min to ensure complete melting of all crystallites and elimination of the blending process thermal history. Samples were then cooled to 20 °C at 10 degrees C/minute. After holding for another 5 min at 20 °C, samples were again heated to 190 °C to study the behavior in the absence of the previous thermal history. The data obtained from the first cooling and the second heating was used for crystallization and melting study, respectively. The value of ΔH^{o}_{f} i.e. is theoretical heat of fusion value of 100% crystalline material for PHBV and PBAT ΔH^{o}_{f} was taken as 109 J g^{-1} and 114 J g^{-1} respectively [12].

Isothermal crystallization experiments of the blends were carried out on DSC. For the isothermal crystallization of the blends, samples were melted at 190 ^{o}C for 4 min, and then rapidly cooled to the respective isothermal crystallization temperature. After complete crystallization, the samples were cooled to room temperature and then heated to 190 ^{o}C at a rate of 10 ^{o}C/min.

6.2.4.2 Wide Angle X-ray Diffraction (WAXD)

To investigate the crystal structure of blend compositions, WAXD measurements were carried out using a Rigaku model D/Max–Ultima III (Rigaku Tokyo). X-rays were generated at 44 mA current and 40 kV voltage with Cu Kα wavelength of 1.542 Å. Diffractograms of the blends were recorded at room temperature in an angular 2θ range of 2 to 60 degrees with a step size of 0.02 and a scanning rate of 2 degrees min^{-1}. All the experiments were performed on the same day with the same set of X-ray filters and X-ray alignment. Film samples made at the same time and in the same mold using same processing conditions were used for the experiment.

6.2.4.3 Small Angle X-ray Scattering (SAXS)

SAXS Working Principle

When a sample is subjected to an incident X-ray beam it causes the oscillations of electrons in the sample at the frequency of the incident radiation. Due to oscillations of electrons, it emits radiation in all the directions. Thus, in SAXS diffraction occurs due to variation in the electron density within the material. When the waves of these scattered radiations from different locations of the material interfere with each other constructively or destructively, a scattering pattern is produced. According to Bragg's law, when the phase shift between the scattered waves is a multiple of 2π it forms

constructive interference. For regular repeating units in the material the scattering angle 2θ is related to the inter-planer distance d. Bragg's equation correlates the inter-planer distance d, scattering angle 2θ, and the wavelength (λ) of X-ray.

$$n\lambda = 2\, d \sin(\theta/2) \qquad (6.1)$$

where n is the order of reflection (positive integer). Scattering in SAXS takes place at very low angle typically less than 2^{o}. The lamellar thickness in the semicrystalline polymers ranges from 10 to 100 nm. The small angle ($0\text{-}2^{o}$) scattering by CuKα radiation corresponds 1 to 100 nm Braggs spacing. So SAXS serves as a powerful tool for analyzing crystalline lamellae in this range. There are several experimental differences between conventional (wide angle) x-ray diffraction and SAXS. The intensity or flux of the incident X-rays in SAXS is several magnitudes higher than the flux of the radiation scattered by material. So the incident X-rays can be overwhelming over sample scattered radiations. Therefore, SAXS requires a highly collimated incident beam. The scattered pattern from the sample is then collected on the detector. The detector measures the intensity as a function of position i.e. 2θ. A vacuum path is used to avoid scattering due to air or other contaminating particles. The X-ray beam monochromatization, components alignment, and adequate counting time is crucial during SAXS.

Instrumentation

D/MAX Ultima III has multilayer mirror and measurement based on a 2-slit type small-angle scattering geometry. X-rays emitted from an X-ray source are made to enter the multilayer mirror. The surface of the multilayer is curved to form a parabola so that any reflected X-rays are emitted in parallel. Parameters used in this investigation are:

- X-ray wavelength: CuKα
- Distance between the x-ray source and mirror center: 100 mm
- Divergence angle of the emitted beam: ~ 0.03-0.05°
- Emitted beam width: 0.84 mm or less

The symmetric transmission (also called as symmetric reflection) method was used for small angle scattering measurement.

A 1 mm divergent slit, 0.2 mm scattering slit, and 0.1 mm receiving slit was used. Figure 6.2 shows standard SAXS configuration.

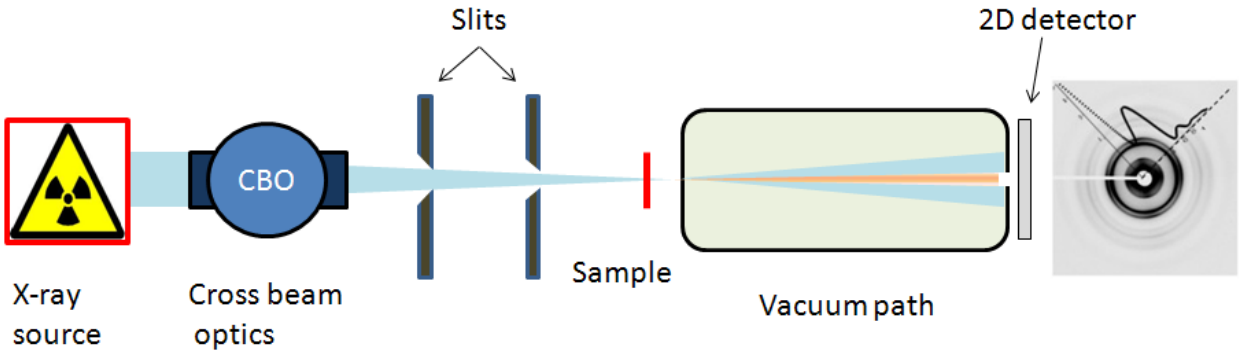

Figure 6.2 Standard Standard measurement configuration

Experimental Procedure and Data Collection

In this work SAXS was performed at room temperature to reveal the lamellar structure in the blends using D/MAX-Rigaku III (Japan) equipped with “Cross Beam Optics”. X-ray source was operated at 40 kV and 40 mA. The generated X-rays provided CuKα radiation with wavelength, λ=1.54 Å. Corrections were made for empty beam, instrumentation background and detector efficiency. The scanning speed of 0.1 degrees/min was used. The isothermally crystallized film samples were used for SAXS. The sample size was 5 mm X 30 mm with 150 ± 10 μm thickness. The SAXS pattern

was collected in the range of 2θ = 0-2º. The raw data obtained from the SAXS experiment was in the form of intensity (I) vs 2θ. The angle θ was used to calculate scattering vector q, where: q= (4π/λ) sin(θ/2).

6.2.4.4 Contact Angle and Surface Energy Measurement [13]

Contact angle and surface energy measurements were carried out by a static sessile drop technique using a CAM- Plus® Contact Angle Goniometer (Cheminstruments, Inc., Fairfield, OH), equipped with a fiber optic light source and video camera for imaging. Samples for contact angle measurements were made on the samples made in compression molding between flat Teflon sheets. Further, the measurement was based on the patented half angle method (US Patent 5 268 733) (Figure 6.3) which eliminates the errors associated with arbitrary tangential alignment. Van Oss et al. [14] have shown that the contribution due to acid base interaction can be expressed in terms of the product of their electron donor and electron acceptor components by using three liquids, one apolar and two polar. According to the Van Oss et al. [27] the surface energy calculations were made using the following equation:

$$(1+\cos\theta) = \left\{\left(\gamma_s^{LW}\gamma_L^{LW}\right)^{1/2} + \left(\gamma_s^{+}\gamma_L^{-}\right)^{1/2} + \left(\gamma_s^{-}\gamma_L^{+}\right)^{1/2}\right\} \quad (6.2)$$

The surface energy of a solid γ_S (or a liquid γ_L) can be divided into the Lifshitz–van der Waals surface energy (γ_s^{LW}) and Lewis acid–base surface energy (γ_S^{AB}) components as described below:

$$\gamma_s = \gamma_s^{LW} + \gamma_S^{AB} \quad (6.3)$$

$$\gamma_S^{AB} = \sqrt[2]{\gamma_s^{+}\gamma_{LS}^{-}} \quad (6.4)$$

Here γ_S^+ is the Lewis acidic or the electron-acceptor component, γ_S^- is the Lewis basic or the electron-donor component and θ is the contact angle of liquid *L* and solid *S*. The surface energy components of three well-characterized test liquids [15, 16] (Table 6.1), i.e. one apolar (dioiodomethane) and two polar liquids (water and glycerol) were used in equation (6.2) to solve for γ_S.

Table 6.1 Surface energy components of the standard liquids (units mJ m^{-2})

Liquids	γ_L^{LW}	γ_L^+	γ_L^-	γ_L^{AB}	γ_L
Water	21.8	25.5	25.5	51	72.8
Glycerol	34	3.92	57	30	64
Diidomethane	50.8	0	0	0	50.8

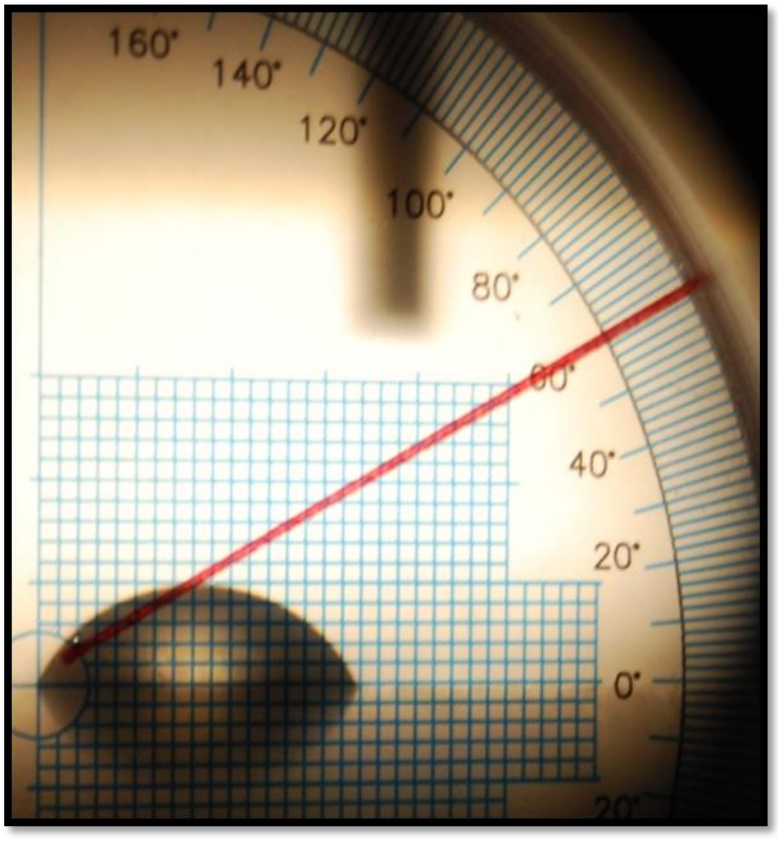

Figure 6.3 Contact angle measurement by half angle method

6.2.4.5 Environmental Scanning Electron Microscopy (ESEM)

The blend morphology of the specimens was observed using FEI Quanta Environmental Scanning Electron Microscope (ESEM; FEI Company, Oregon, USA) at an accelerating voltage of 15 to 20 kV. The SEM samples were prepared by cryo fracturing the compression pressed samples. The fractured surface was then gold coated for better electron discharge and to obtain good resolution and morphological images.

6.2.4.5 Polarized Optical Microscopy

A Zeiss Imager A1 polarized optical microscope equipped with an Instec STC200 hot stage was used to investigate the microstructure of the PHBV/PBAT blends. Thin films of all the compositions were prepared in a Carver compression press. The films were 20 to 40 μm thick. During polarized optical microscopy the film samples were sandwiched between two thin glass slides and heated on a hot-stage from 30°C to 190°C at the rate of 10°C/min. The samples were then held at 190°C for 5 minutes in order to destroy any traces of previous crystallinity and then quenched to 80°C (T_c) at the rate of 40°C/min and crystallized isothermally to observe the spherulitic growth. It should be noted that the thermal history applied during the optical microscopy was similar to that used in preparation of samples for SAXS.

6.3 Results

6.3.1 Differential Scanning Calorimetry

Figure 6.4 and Table 6.2, 6.3 presents DSC second heating and second cooling scans at 10 ^{o}C/min for PHBV/PBAT blends. The various thermal property results calculated from the DSC heating and cooling curves are summarized in Table 6.2 and Table 6.3 respectively. In the heating scans bimodal endothermic melting peaks can be observed. The bimodal peaks at 160-170 ^{o}C can be the result of either the presence of two crystalline phases or the modification of the same crystalline phase. Multiple melting peaks in poly(vinylidene fluoride) and polypropylene have been attributed to the coexistence of multiple crystal modifications [17, 18]. This can be confirmed from the wide angle X-ray diffraction (WAXD) results.

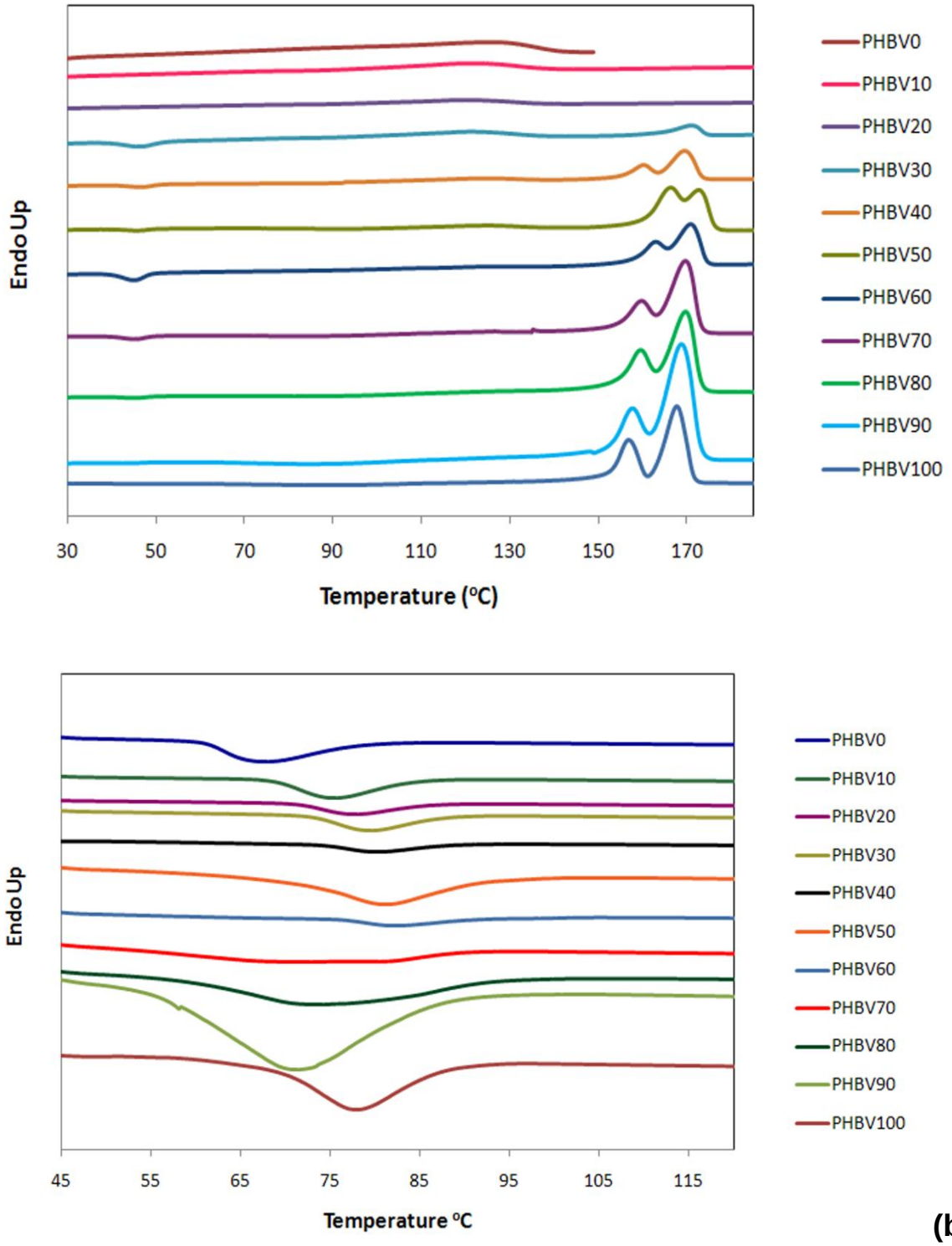

Figure 6.4 DSC traces for PHBV and PHBV/PBAT blends (a) second heating; (b) second cooling.

The crystallization rate of PHBV is very slow and therefore, the chances of forming metastable crystallites during the cooling cycle are very high. The same metastable structure melts at low temperature giving an endothermic peak. Subsequently, with an increase in temperature the crystallites form an ordered structure, releasing heat and forming a crystallization trough during melting. The newly ordered crystallites and the crystallites which were already present in the sample, melt simultaneously giving a second bigger endothermic peak.

An intriguing result in the analysis is the observation of an increase in the melting point temperature by the addition of low melting component i.e. PBAT. The T_m of PHBV100 (first peak) was observed at 155 ^oC which increased to 161 ^oC for PHBV50. For PHBV80 AND PHBV90, a single melting temperature was observed. In PHBV30 two separate melting peaks for PHBV and PBAT components were observed again increased T_m for PHBV peak. The melting point hump was also observed for the PBAT component around 125 ^oC and the peak temperature decreased with a decrease in wt % of PHBV from 30 to 0.The possible reasons for elevation in melting point temperature are discussed in the next section. The ΔH value for PHBV90 is higher than pure PHBV indicating a nucleation effect of well dispersed PBAT at low concentration. In the cooling curve also, ΔH value for PHBV90 was higher than the pure PHBV but reduced the crystallization rate.

In cooling curves, single crystallization peaks were observed for PHBV/PBAT blends. Increased crystallization temperatures (T_c) can be observed for blend compositions relative to the pure components. For PHBV90 to PHBV60 compositions, crystallization took place over a broader temperature range (onset to end crystallization

temperaure) compared to other compositions. This indicates that the addition of PBAT restricted the crystallization by interfering with the PHBV crystallization. Here the PBAT acted as a noncrystalline diluent which reduced the overall crystallization rate of the PHBV phase. In case of PHBV10 to 40, the crystallization temperature increased with an increase in the % of PHBV. This can be attributed to the simultaneous crystallization of both the phases induced by finely dispersed PHBV phase. The overall non-isothermal DSC results indicated composition dependent melting and crystallization of the blends. The modified melting behavior and restricted crystallization ability of the blends compared with neat polymers indicated miscibility of the blends.

Table 6.2 Second heating cycle thermal parameters of PHBV/PBAT blends

PHBV Fraction	Peak #	Onset Temp. (°C)	End Temp. (°C)	Peak Temp. (°C)		Area (mJ)	Delta H (J/g)
0	1	100.57	137.38	121.37	-	55.02	11.96
10	1	97.95	138.39	120.39	-	64.61	12.92
20	1	100.26	137.61	120.1	-	40.27	11.18
30	1	40.03	51.72	46.77	-	-11.74	-2.21
	2	104.48	136.84	120.54	-	44.15	8.33
	3	163.17	174.59	171.02	-	28.16	5.31
40	1	41.69	50.96	47	-	-4.66	-1.23
	2	103.96	136.2	123.8	-	15.86	4.18
	3 (Double)	156	173.54	158	170	95.97	25.32
50	1	42.49	48.87	46.05	-	-1.84	-0.38
	2	109.58	135.99	124.23	-	15.85	3.28
	3 (Double)	160.21	176.34	165	173	204.21	42.36
60	1	40.31	48.98	45.24	-	-14.38	-4.23
	2 (Double)	160	174.54	162	172	143.09	42.08
70	1	40.61	48.81	45.43	-	-5.25	-1.01
	2 (Double)	153	173.3	158	170	263.03	50.87
80	1	40.89	49.24	45.24	-	-0.01	-0.48
	2 (Double)	162.72	173.39	157	169.83	369.51	59.59
90	1 (Double)	153	173.14	156	168.83	559.12	61.1
100	1 (Double)	152	171.67	155	167.93	287.17	82.05

Table 6.3 Second cooling cycle thermal parameters of PHBV/PBAT blends

PHBV Fraction	End Ttemp. (°C)	Peak Temp. (°C)	Peak Height (mW)	Area (mJ)	Delta H (J/g)
0	78.23	61.09	67.41	-1.27	-18.72
10	84.21	68.49	75.2	-1.25	-14.9
20	85.51	71.17	77.3	-0.78	-12.64
30	87.82	72.63	79.21	-1.02	-11.37
40	88.14	74.23	80.44	-0.54	-7.79
50	92.18	70.53	80.79	-1.71	-32.39
60	90.45	76.47	82.37	-0.43	-6.71
70	87.71	91.31	81.19	-0.36	-5.03
80	92.35	57.71	72.94	-1.71	-38.19
90	85.38	56.92	70.98	-3.81	-43.67
100	87.39	60.23	77.8	-2.95	-66.03

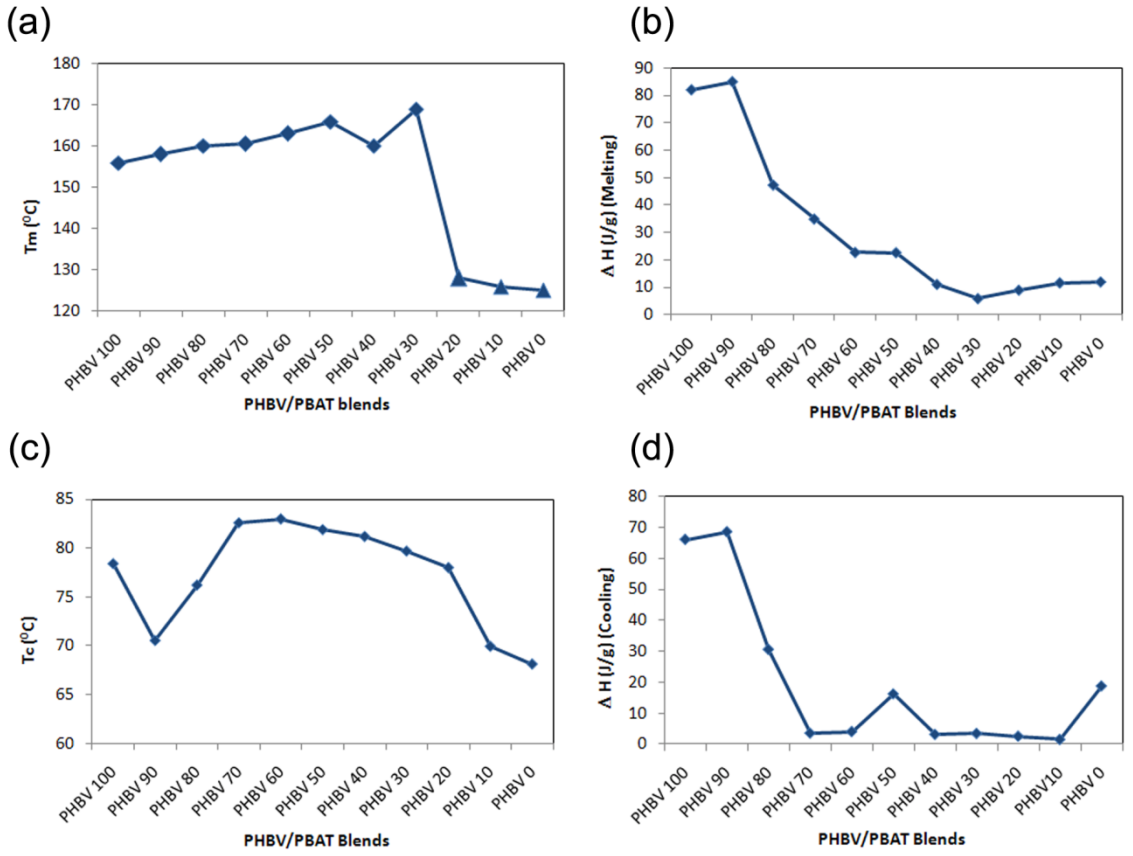

Figure 6.5 Composition dependent a) Tm, b) ΔHmelting, c) Tc, and d) ΔHcooling of PHBV/PBAT blends

6.3.2 Crystalline Structure of PHBV/PBAT Blends Analyzed by WAXD

In order to investigate the effect of blending on the crystal structure of the components, WAXD experiments of PHBV/PBAT were performed. Figure 6.6 demonstrates the WAXD patterns of PHBV/PBAT blends with various blend compositions. Neat PHBV shows two strong diffraction peaks at around 13.5°, 16.5°, 22.5°, 25.3° corresponding to (020), (110), (111) and (121) planes, respectively which indicates an orthorhombic crystal structure of the PHBV crystal unit [19, 20]. The WAXD patterns involve all the diffraction peaks corresponding to neat components in the blends, however particularly for PHBV70, PHBV60, and PHBV50 the (110) peak height was increased were shifted to lower 2θ values. The WAXD results indicate that PHBV crystal structure was affected by the addition of PBAT and both the components of the blend crystallized simultaneously. However, the above WAXD results confirm that PHBV and PBAT adopt the same crystal modification and chain conformation. Consequently, the multiple melting peak behavior appeared in the DSC was not the result of different crystal forms or chain conformations but from the modification of α-crystalline form. Thus, multiple endothermic peaks in the DSC results cannot be from different phases but due to modification of the same crystalline phase. To evaluate the equilibrium melting point temperature in isothermal crystallization studies, the first lower melting peak temperature was chosen. The first melting peak was completely related to the melting of crystallites formed during crystallization and the second peak was the result of melting and recrystallization of first peak [21].

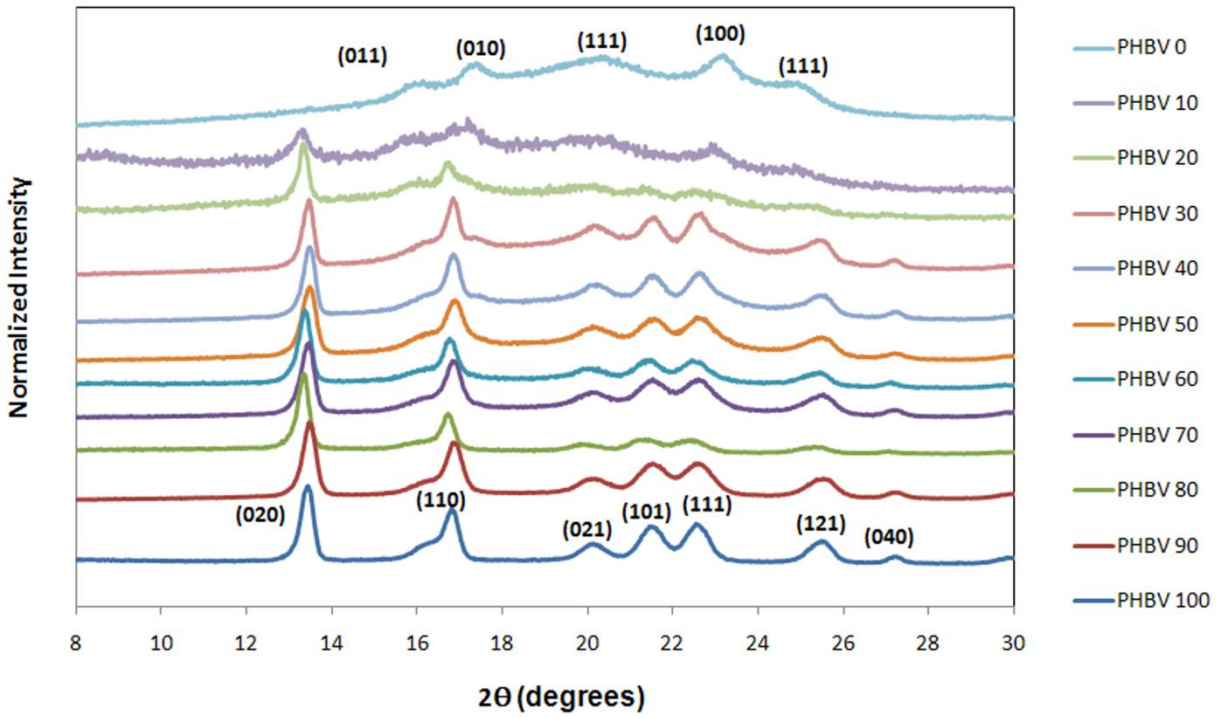

Figure 6.6 WAXD pattern of PHBV/PBAT compositions

6.3.3 SAXS

The semicrystalline polymer blend supposed to consists of periodically arranged crystalline lamellae. The lamellar stack contains crystalline and amorphous regions. The basic crystalline microstructures depend strongly on chemical structure, molecular weight, thermal history, cooling rate, crystallization, etc. Figure 6.7 shows interlamellar morphological structure containing average crystal thickness (l_c), average amorphous thickness (l_a) and the average distance between crystals (L). The average distance between two crystals (average long period of the crystalline stacks) (L) can be calculated from the peak maximum position of the Lorentz-corrected profile using Bragg's equation.

$$L = 2\pi / q_{max} \qquad (6.5)$$

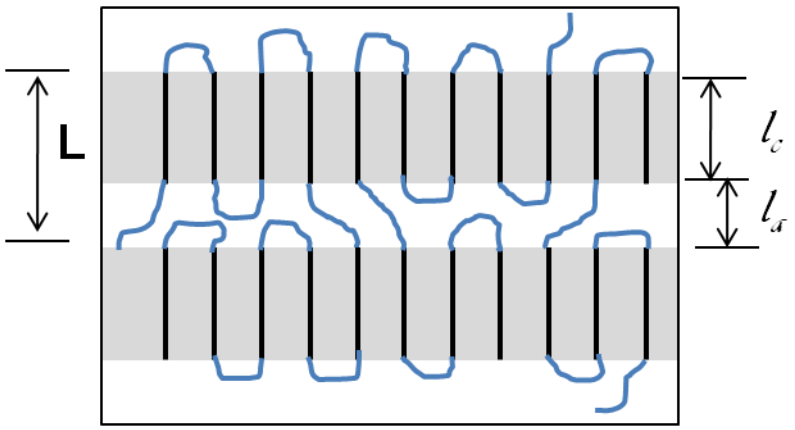

Figure 6.7 Schematic representation of interlamellar morphology of polymer crystal

L, ℓ_c, and ℓ_a can be determined from one dimensional correlation function γ (z). From scattering intensity γ (z) can be obtained by following equation.

$$\gamma(z) = \int_0^\infty I(q) q^2 \cos(2\pi q z) dq \tag{6.6}$$

where z is the direction along which electron density is measured. Fourier transformation of Lorentz-corrected intensity gives a one dimensional correlation function. The experimentally measured *q* value is limited so integration intensity from the lower *s* to higher *q* values is necessary. The lower q value and higher q value can be obtained by extrapolating measured q value to zero and using Parod's law respectively.

$$\lim_{q \to \infty}(I(q)) = K_p q^{-4} + B \tag{6.7}$$

where K_p is Parod constant and B is residual background term. K_p can be obtained from following equation.

$$K_p = 2\pi (s/v)(\Delta\rho)^2 \tag{6.8}$$

where (s/v) is the specific surface, $\Delta\rho$ is difference in scattering intensities of crystalline and amorphous region.

Polymer blends do not have long range order therefore higher order peaks cannot be seen in the SAXS result. Further, blends show isotropic scattering in the absence of any flow. So it can be inferred from the SAXS data that the primary crystal structure remained unchanged while secondary small crystal structure changed with composition. As both the polymer components are crystalline and were crystallized at 80 ^{o}C, the degree of supercooling decreased to form more perfect crystalline structure.

Figure 6.8 shows the Lorentz-corrected SAXS profiles of PHBV/PBAT crystallized at 80 °C. The multiple peaks indicate a well lamellar stacking in the samples. All the sample compositions exhibits a strong scattering peak due to high electron density contrast ($\Delta\eta=\eta_c-\eta_a$) between the crystalline and amorphous layers. The enhancement in scattering intensity of the blends compared to pure components is attributed to the incorporation of PBAT in inter lamellar (IL) regions, as this would enhance the electron density contrast between the different crystalline layers. Second and third peak indicate the small, thin, and less regular crystalline structure. With the addition of PBAT, the secondary SAXS peaks systematically moved towards lower q, indicating the inclusion of PBAT in PHBV interlamellar region. Peak broadening was observed with addition of PBAT in PHBV indicating increased lamellar thickness distribution. For crystalline-crystalline polymer blend the increase in long period (crystalline + amorphous) is associated with an increase in the thickness (T) of the crystal. This is confirmed in Table 6.4.

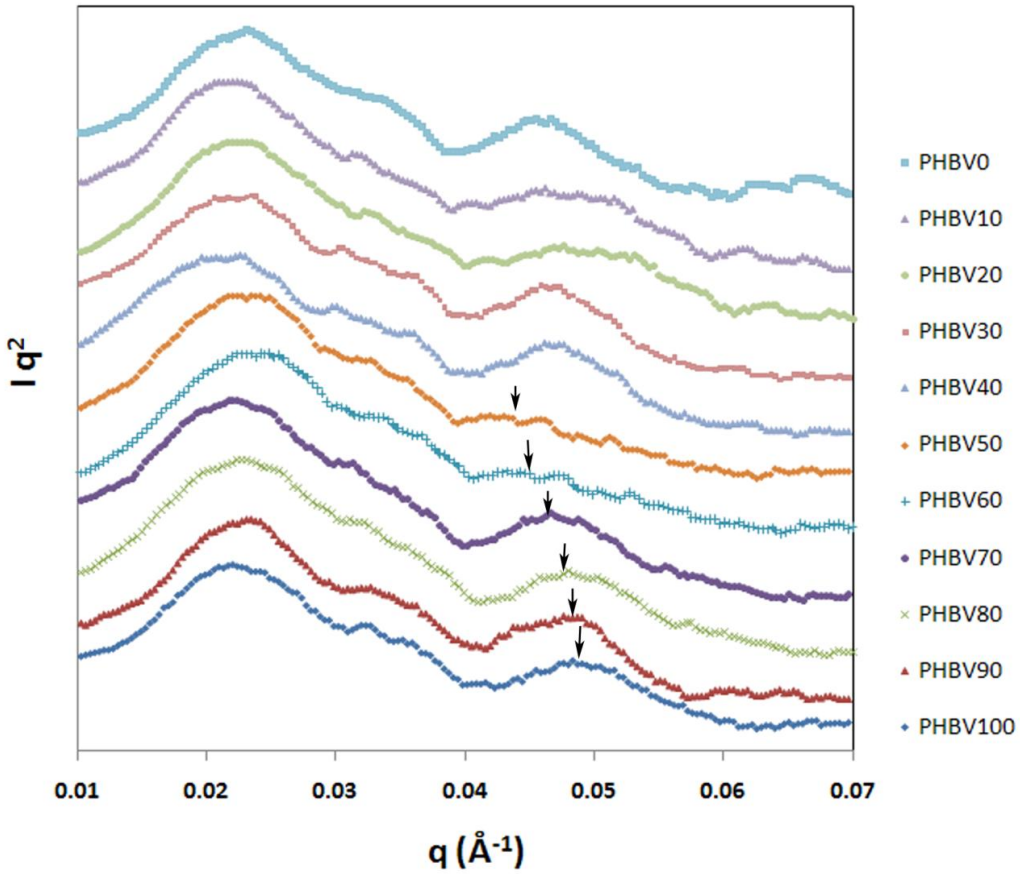

Figure 6.8 Lorentz-corrected scattering data for PHBV/PBAT blends.

Table 6.4 Secondary crystal thickness and equilibrium melting point comparison

Composition	T (nm)	T_m^0
PHBV100	20.4	171.1
PHBV90	20.8	172
PHBV80	21	174
PHBV70	21.3	175.5
PHBV60	21.8	181.5
PHBV50	22.1	182.3
PHBV40	22.2	176
PHBV30	21.2	134.1
PHBV20	21.4	133
PHBV10	21.7	131.8
PHBV0	21.7	129.6

Isothermal Crystallization and Melting of PHBV/PBAT Blends

To avoid potential complications due to changes in lamellar thickness, we have followed the method of Hoffman and Weeks and directly determined the T_m^o of the compositions. As shown in the SAXS study, rejected PBAT component resides in the interlamellar regions of PHBV during crystallization. The T_m/T_c method has been employed to investigate the effect of blending on equilibrium melting point (T_m^o). Therefore an isothermal crystallization and subsequent melting thermal scan was done. The equilibrium melting temperature is defined as the melting point for infinite chain crystals where polymer chain ends have been paired as in the case of crystallization in small molecules. However, such an equilibrium crystal can never form so T_m^o has to be estimated by extrapolation. This nucleation theory is based on the assumption that the difference between melting and crystallization temperature is due to crystal thickening at the crystallization temperature. This forms the basis for the Hoffman-Weeks method to determine T_m^o. In this method a plot of melting temperature Vs crystallization temperature has been used to determine the T_m^o.

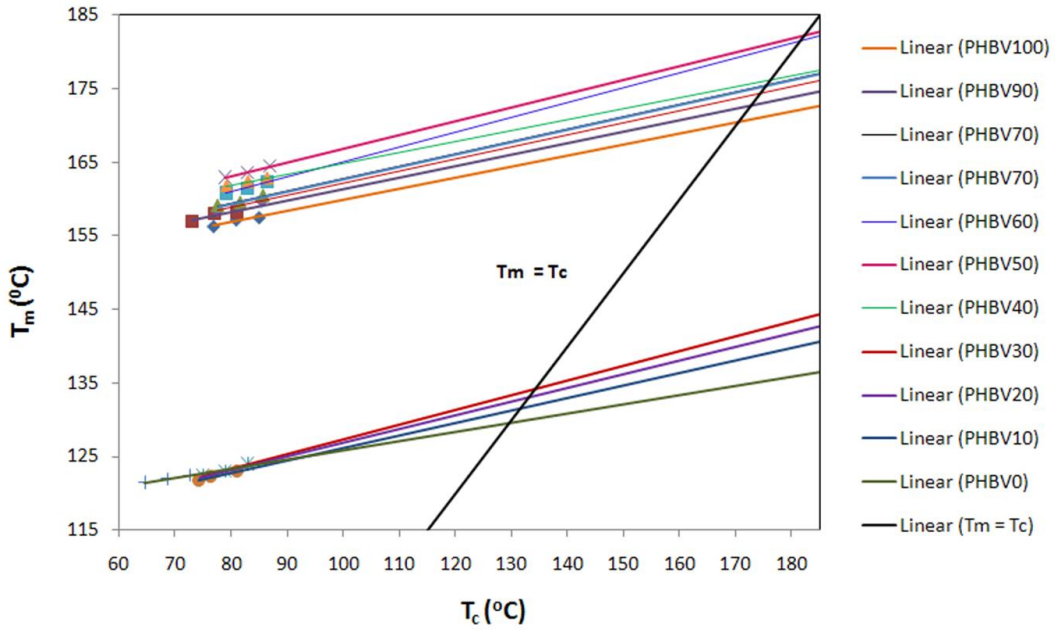

Figure 6.9 Hoffman Weeks plot shows the dependence of melting point on crystallization temperature

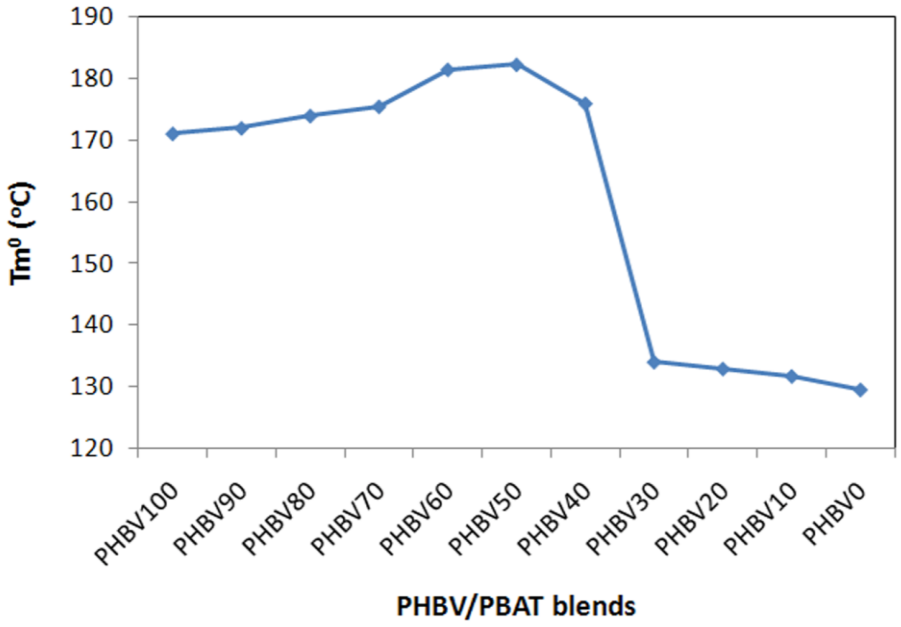

Figure 6.10 Equilibrium melting point temperatures of PHBV/PBAT blends

Table 6.5 Melting point temperature dependence on crystallization temperature

PHBV 100		PHBV 90		PHBV 80		PHBV 70		PHBV 60		PHBV 50	
T_c	T_m	T_c	T_m	T_c	T_m	T_c	T_m	T_c	T_m	T_c	T_m
84.9	157.5	81.1	158.25	77.6	158.5	85.65	160.45	79.1	160.8	87	164.5
80.9	157.2	77.1	158	81.4	159.1	81.65	159.51	82.9	161.5	83	163.6
76.9	156.3	73.1	157	85.5	159.8	77.65	159.1	86.5	162.3	79	163

PHBV 40		PHBV 30		PHBV 20		PHBV 10		PHBV 0	
T_c	T_m	T_c	T_m	T_c	T_m	T_c	T_m	T_c	T_m
79.1	161.8	83	124	81	123.4	74.2	121.8	72.6	122.5
83	162.4	79	123	77.1	122.6	76.4	122.3	68.6	122
86.5	162.9	75	122.4	74.5	122.2	81.1	123	64.6	121.5

Table 6.6 PHBV/PBAT blends and equilibrium melting point temperature obtained by extrapolation method

Composition	T_m^0
PHBV100	171.1
PHBV90	172
PHBV80	174
PHBV70	175.5
PHBV60	181.5
PHBV50	182.3
PHBV40	176
PHBV30	134.1
PHBV20	133
PHBV10	131.8
PHBV0	129.6

6.3.4 Contact Angle and Surface Energy

According to the Nishi Wang relationship, a change in the surface energy has a direct effect on the melting temperatures of the blends. From the DSC cooling data it has been observed that the less crystalline PBAT phase has disturbed the degree of crystalline perfection due to a dilution effect. Many researchers [22, 23] have shown that the spherulite becomes coarse and open as the concentration of the noncrystallizable component increases. However, spherulitic order itself would not directly influence the melting point temperatures. If the individual lamella within the spherulites become of dimensions such that side surface free energy affects the melting point. Following the argument of Hoffman and Weeks, the free energy of formation of a crystal and lateral thickness of the crystal "x", and crystal thickness L can be correlated by following equation.

$$T_m = \Delta T_m{}^o \left[1 - \frac{1}{\Delta H_f{}^o}\left(\frac{2\sigma_e}{L} - \frac{4\sigma}{x}\right)\right] \quad (6.9)$$

So it is important to note that the increase in melting point temperature can be observed with increase in lateral crystal thickness of the sample. The results of the surface energy measurements are presented in Table 6.7. As can be seen surface energy decreased with increased PBAT content. Further, surface characterization of the blends gives an idea of the thermodynamic work of adhesion between the PHBV and PBAT polymer chains. As known from acid–base adhesion theory, when the surface acidity of one component is high and the surface basicity of the other component is also high, then strong adhesion between the components, and better compatibility occurs [24].

Table 6.7 Surface energy components and surface energy of PHBV/PBAT blends

Compositions	Contact angle			Surface energy components				Surface energy γ_S (mJ m^{-2})
	Water	Glycerol	Diiodomethan	γ_S^{LW}	γ_S^+	γ_S^-	γ_S^{AB}	
PHBV100	62 ± 0.23	58 ± 0.16	37 ± 0.21	40 ± 0.11	0.19 ± 0.01	17 ± 0.32	3.6 ± 0.12	44 ± 0.12
PHBV90	66 ± 0.42	61 ± 0.31	39 ± 0.17	39.9 ± 0.08	0.15 ± 0.03	14 ± 0.55	3.0 ± 0.22	42 ± 0.22
PHBV80	68 ± 0.3	62 ± 0.2	39 ± 0.21	39 ± 0.02	0.1 ± 0.01	13 ± 0.2	2.8 ± 0.14	42.2 ± 0.18
PHBV70	70 ± 0.34	64 ± 0.21	41.0 ± 0.3	39 ± 0.15	0.09 ± 0.02	12 ± 0.41	2.1 ± 0.16	41.2 ± 0.17
PHBV60	70 ± 0.28	65 ± 0.12	42 ± 0.14	38 ± 0.13	0.09 ± 0.01	12 ± 0.32	2.1 ± 0.13	40.5 ± 0.14
PHBV50	71 ± 0.26	66 ± 0.42	44.9 ± 0.31	37.1 ± 0.17	0.09 ± 0.02	12 ± 0.4	2.1 ± 0.26	39.2 ± 0.27
PHBV40	72 ± 0.16	67 ± 0.41	47.1 ± 0.24	35 ± 0.15	0.08 ± 0.01	12 ± 0.2	2.1 ± 0.24	37.3 ± 0.14
PHBV30	73 ± 0.25	69 ± 0.25	50.4 ± 0.27	34 ± 0.15	0.08 ± 0.02	13 ± 0.34	2.1 ± 0.18	36.2 ± 0.19
PHBV20	75 ± 0.3	70 ± 0.8	63.1 ± 0.2	32.1 ± 0.2	0.6 ± 0.03	8.5 ± 0.26	3.6 ± 0.3	35.7 ± 0.2
PHBV10	83 ± 0.25	73 ± 0.43	67.0 ± 0.42	24 ± 0.23	1.0 ± 0.09	5.7 ± 0.28	4.9 ± 0.15	29.4 ± 0.18
PHBV0	91 ± 0.3	82 ± 0.52	70 ± 0.22	22 ± 0.12	0.37 ± 0.07	4.3 ± 0.3	2.5 ± 0.16	25.2 ± 0.17

6.3.5 ESEM

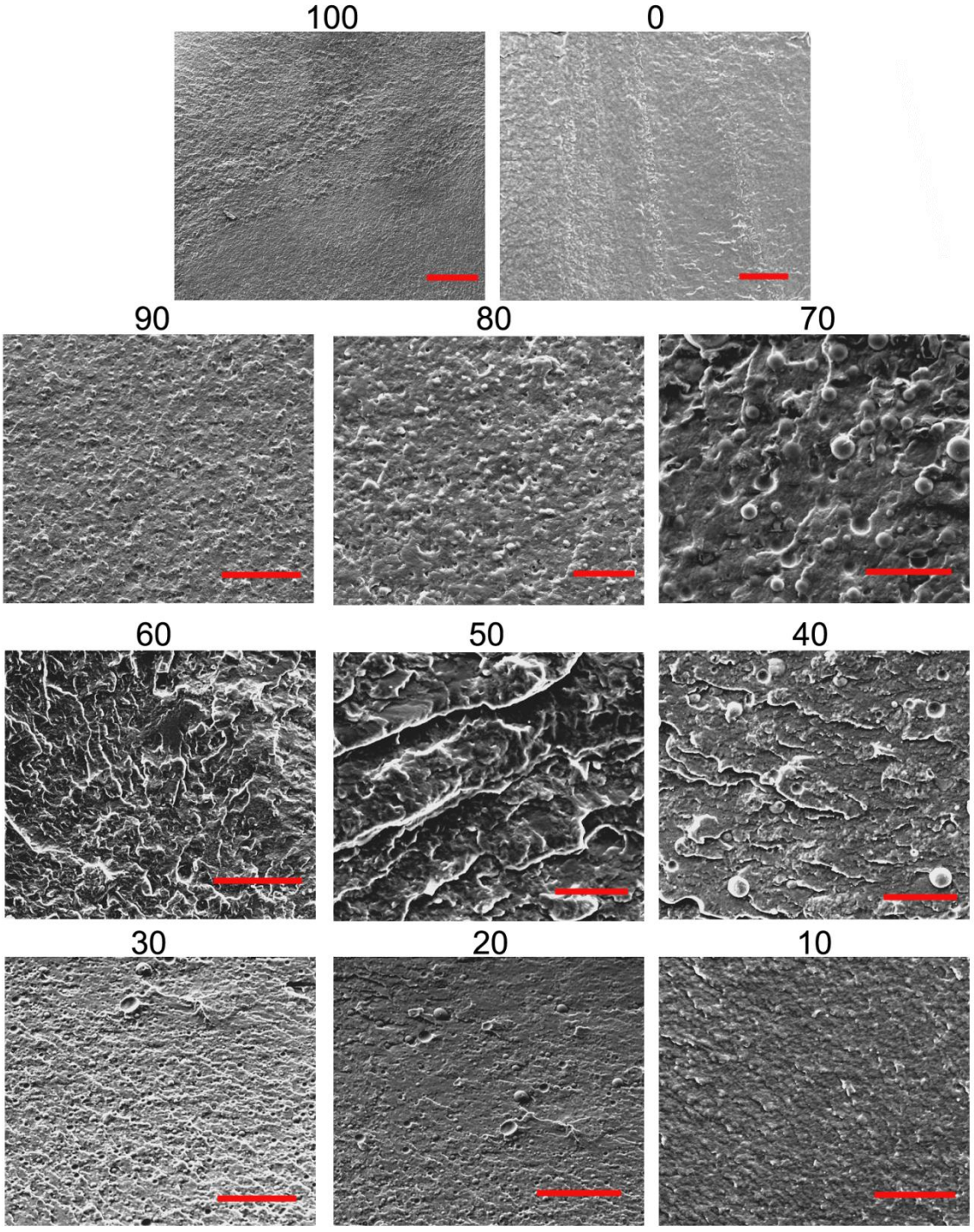

Figure 6.11 ESEM images of PHBV/PBAT blends (numbers indicate PHBV wt % in the sample composition, scale bar 50 μm)

Figure 6.11 shows SEM images of PHBV/PBAT brittle fractured samples. The dispersed phase of PBAT in PHBV rich blend compositions and vice versa can be seen. Domain size of dispersed phase increased with increase in concentration. Co-continuous morphology was observed at PHBV50 and PHBV60 concentration.

6.3.6 Polarized Optical Microscopy

During crystallization, polymers form spherulitic morphology and form ribbon like crystals (lamellae) growing outwards from a central nucleus. Banded structures are commonly observed in polymeric spherulites and are believed to arise from twisting of radiating lamellar crystals about their axis of fastest growth [25]. Long range order of spectacular banded structure can be observed in PHBV spherulites. The size of the perfect ring-banded spherulites is greater than 1 mm. The band spacing is quite uniform, and it is calculated to be about 20 μm. In the banded structure synchronously twisted lamellar growth takes place. Keith and Padden [26, 27] proposed an explanation of synchronously twisted lamellar growth based on unbalanced mechanical stresses existing on the lamellar surface. An alternative view by Bassett et al. [28] considers a succession of isochiral giant screw dislocations whereby each screw dislocation contributes to the overall twist by a quantum increment of lamellar splay.

On a glass slide, under optical microscope the crystalline lamellae are quasi-2D objects and it can be assumed that the thickness of the lamellae is much smaller than their width and length. Highly birefringent spherulites were observed in pure PHBV. Figure 6.12 shows the crystalline morphology of PHBV spherulites at 80 ^{o}C for 20 min. Growth ceased when two PHBV spherulites impinged on each other. However, when one growing PHBV spherulite reached the fixed PBAT spherulite, it continued to grow

over the PBAT spherulite instead of growth termination. A dominant PHBV banded structure can be seen in PHBV rich blends. While in the PBAT rich phase, smaller, low birefringent, and more compact spherulites of the PBAT were observed. In the blend samples the large and compact spherulites were of PHBV and the small ones were of PBAT component.

Figure 6.13 to 6.21 show the spherulitic morphology of the PHBV and PBAT phases, at various blend compositions, during and after crystallization from melt at 80 ^{o}C. The spherulites show the familiar maltese cross birefringent pattern and exhibit concentric extinction bands but the PBAT rich composition showed a coarse PHBV spherulitic texture with a disruption of Maltese-cross pattern as shown in Fig. 6.12.

In the PHBV rich phase, the growth of the PHBV spherulites takes place in the background of the PBAT phase. The diameter of isothermally crystallized spherulites grows linearly. It should be noted that for the neat polymer phases, the crystallization proceeds through homogenous nucleation while in the blends, nucleation appears to be heterogeneous with uneven phase structures. Disruption of Maltese-cross pattern indicates the intraspherulitic segregation of PBAT during the crystallization of PHBV. The spherulites of the PBAT are very small compared to the spherulites of the PHBV. The diameter of fully grown spherulite of the PHBV is approximately 500-800 μm while the PBAT spherulite is 5 – 20 μm.

The observation of the spherulitic growth of the low- T_m component is usually difficult in crystalline/crystalline polymer blends because it must crystallize in the matrix of the pre-existing crystals of the high-T_m component. In case of PHBV-rich blends, we found that the original PHBV spherulitic texture in Fig. 6.13, 6.14, and 6.15 was not

influenced much. This implies that PBAT was unable to crystallize or just formed tiny crystals totally masked by the PHBV crystals at 80 ^{o}C in these PHBV-rich compositions. These observations reveal that the spherulitic morphology of the crystalline/crystalline PHBV/PBAT generated by isothermal crystallization at 80 ^{o}C is largely affected by the blend composition where the major component always dominates the spherulitic formation.

For PHBV90 the nucleation density increased due to the presence of the dispersed PBAT phase acting as a nucleating agent. The decreased size of the PHBV spherulites was observed at this composition. During the crystallization of blend, it was observed that PBAT component acted as a noncrystalline diluent which reduces the spherulitic growth rate as well as overall crystallization rate of the PHBV phase. The interesting co-crystallization of PHBV and PBAT components and the migration of crystallite domains to form separate phases was observed for the PHBV rich blend samples.

The crystallization of both PHBV and PBAT could be observed simultaneously with PHBV spherulite growing faster, and the interpenetration of PHBV spherulites by PBAT spherulites was also found. The inter-penetration process is shown in Figure 6.17. Two different types of spherulites could be observed during the crystallization of this blend sample. Instead of growth being arrested, the PHBV spherulite continued to grow over PBAT spherulites. The smaller spherulites of PBAT compare to PHBV spherulites were hard to see due to high nucleation density but at high magnification and corrected focus, both the spherulites were clearly visible. These results indicated that PBAT spherulites penetrated into the PHBV spherulite.

The fact that PBAT penetrated into PHBV spherulites but PBAT did not penetrate into PHBV spherulites may be explained as follows. The number of lamellae per unit volume, in PBAT spherulites may be higher than that of PHBV. Furthermore, the sparse spherulites of PHBV contained a sufficient amount of amorphous space, which enabled the fibrils (stacks of lamellae) of PBAT spherulites to continue to crystallize in the interfibrillar region of PHBV spherulites on contact.

Even though the phase separation was evident, increased band spacing was observed for blend samples. This implies that PBAT was partially contained within the PHBV spherulites during co-crystallization at 80 ^{o}C. With, increasing PBAT content, the band spacing progressively became larger. The increased band spacing with increased PBAT content can be correlated to increased T_c temperature [29]. Therefore, the effect of the addition of PBAT on the band spacing is equivalent to an increase in Tc.

6.4 Discussion

6.4.1 Melting Point Elevation in Polymer Blends

In the DSC study, an elevation in the melting point temperature was observed by the addition of PBAT (up to 70 wt %) in PHBV. In a majority of blend melting studies, the experimental melting point was observed to decrease with an increase in the second compatible polymer concentration. However, there are very few reports with an elevation of the melting point temperature with increasing concentration of the second component. The possible reasons for observed melting temperature elevation are discussed here. The most widely used technique to study the compatibility and induced interaction in polymer blends is to investigate the melting and crystallization behavior. If two polymers are miscible then the chemical potential of the blend will decrease by the

addition of the diluents. If the polymers are crystallizable, this decrease in the chemical potential will result in decreased equilibrium melting point. According to the Scott [30], Nishi and Wang [31] equations, the melting point depression is a function of blend composition and interaction parameters (χ). In other words one would expect depression in melting point when χ is negative. And so it has been suggested that if χ is positive, one should observe an equilibrium melting point elevation. Based on the thermodynamic criteria, when χ is positive the blend is expected to be incompatible. Runt et al. [37] suggests that even if χ is positive, the blend can be miscible or compatible when mixing is driven by combinatorial entropy which is not considered in Nishi - Wang equation. The Scott, Nishi-Wang relationship [32] describing melting point depression of a crystalline polymer due to presence of miscible diluent is expressed as :

$$\frac{1}{T_{m_{PHBV}}{}^{o}} - \frac{1}{T_{m_B}{}^{o}} = \frac{RV_{PHBV}}{\Delta H_{f\,(PHBV)}{}^{0}\, V_{PBAT}} \left[\frac{\ln \Phi_{\mathrm{PHBV}}}{\mathrm{m_{PHBV}}} + \left(\frac{1}{\mathrm{m_{PHBV}}} - \frac{1}{\mathrm{m_{PBAT}}}\right) \Phi_{\mathrm{PBAT}} + \chi\, \Phi_{PBAT}{}^{2}\right] \tag{6.10}$$

where V is the molar volume of the polymer, Φ is volume fraction of the component, in the blend, $\Delta H_f{}^0$ is perfect crystal heat of fusion, M is the degree of polymerization, R the universal gas constant, Tm^o equilibrium melting point, and χ is the interaction parameter. In polymer blends with high molecular weight, the effect of entropy can be neglected and the change in the melting point will be due to enthalpic effects. Therefore the above equation will reduce to:

$$\frac{1}{T_{m_{PHBV}}{}^{o}} - \frac{1}{T_{m_B}{}^{o}} = \frac{RV_{PHBV}}{\Delta H_{f\,(PHBV)}{}^{0}\, V_{PBAT}} \left(\chi\, \Phi_{PBAT}{}^{2}\right) \tag{6.11}$$

It can be observed that when χ is less than zero, greater the polymer-polymer interaction and reduced melting point temperature of the blend is predicted. Also, with an increase in the fraction of the less crystalline component, an increase in the T_m^0 would be observed. This phenomenon has been widely studied and the depression in the equilibrium melting point has been observed in miscible blends on addition of a diluting polymer component by many researchers. Further, according to the Hoffman Weeks relationship (equation 6.6), T_m^o would decrease with increasing th amount of amorphous component and the thickness of lamella in the blend would be expected to be larger than that of the pure polymer due to decreased supercooling when the blend crystallizes. J Runt et al. [32] explained that if the crystallizable polymer and amorphous polymer crystallized at the same temperature the thickness of lamella in the blend would be expected to be larger than that of the pure polymer. This is due to decreased supercooling at which the blend crystallizes. Runt et al. [34] and Rim et al. [33] explained that melting point elevation can be observed in the blend when the following conditions occur. Their possible reasons for melting point elevation are as follows:

1) Change in the surface energy of the blend.

Hoffman Weeks equation shows the dependence of melting point on surface energy and crystal thickness.

$$\Delta T_m = \Delta T_m{}^o + \frac{2\sigma_e}{\Delta H_f{}^o}\left(\frac{T_{mB}{}^o}{L_B} - \frac{T_m{}^o}{L}\right) \qquad (6.12)$$

where, σ_e is the surface energy, $\Delta T_m = T_m - T_{mb}$ is the experimentally observed melting point difference between pure crystalline polymer and crystalline polymer in blend, L

and L_B are the crystalline thicknesses of the crystalline polymer in the pure state and in the blend. Thus an increase in L will contribute to an increase in Tm.

2) DSC experimental effect

The scanning rate can also affect the melting temperature of the polymer. Polymers have low thermal conductivity. Therefore, when they are heated at a very high rate chances are that they may not be completely molten at the measured temperature. Due to poor thermal conductivity and less high temperature exposure time at a high heating rate, the polymer would melt at a higher temperature than its actual melting temperature.

3) Increase in crystal perfection

Increased T_c temperature indicates an increase in crystal perfection as the degree of supercooling decreases. The blend melting point would be expected to increase with increasing crystal perfection.

4) Also, when the lateral crystal order increases one can see possible elevation in the melting point.

6.4.2 Miscibility Analysis

Miscibility behavior of the two polymer phases can be observed under an optical microscope during crystallization process. The molten phases are clearly heterophasic, as shown in Fig. 6.18, where circular domains of PBAT are present in the PHBV matrix, some of which coalesce after a short time. By reducing the temperature, crystallization of the PHBV begins. During this process, the spherulites of PHBV segregate the crystalline domains of PBAT, as shown in Fig. 6.19. Moreover, the blends of PHBV/PBAT examined at the DMTA exhibit two glass transition temperatures at around

-22 ^{o}C and 25 ^{o}C, in agreement with the values of the neat components. For all of the samples studied, biphasic separation was observed, indicating that PHBV was not miscible with PBAT in the melt but affected the crystallization process of individual components. The crystallization of the two phases took place at the same time and temperature; however the crystallization of each of the polymer blend components resulted in phase separation in which the individual component segregated from the mixture to form a pure phase.

Once spherulitic structures are formed, they continue to grow until they impinge one another. This crystal growth is called primary crystal growth in which the crystals are more ordered and thick in shape. After primary crystal growth, secondary crystal growth starts in confined regions of uncrystallized melt. Secondary crystals are usually thinner and imperfect.

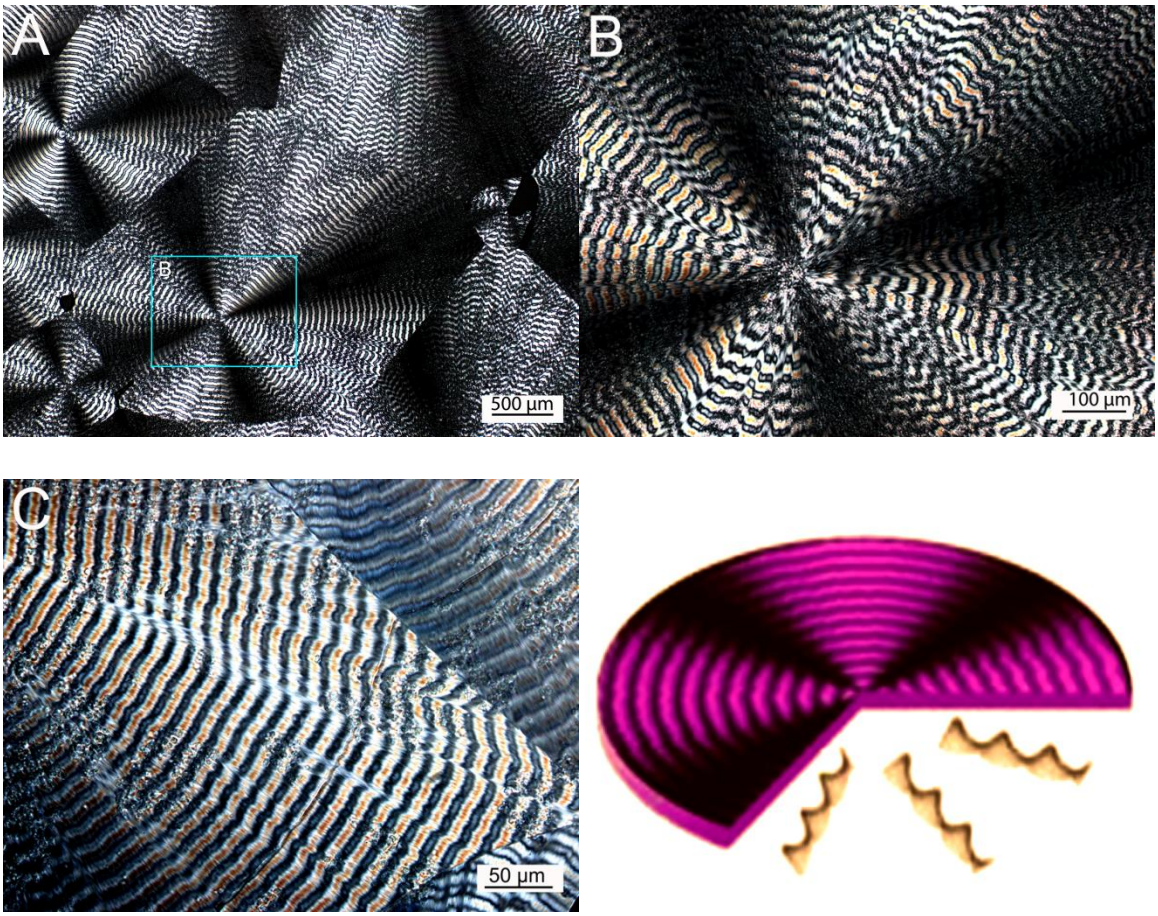

PHBV100

Figure 6.12 (a) Polarized optical micrograph of a maltese cross birefringent pattern in neat PHBV, (b) and (c) show the banded spherulitic structure crystallized from the melt at 80°C. (d) Sketch show orientation of the lamellar helicoids in a PHBV spherulite.

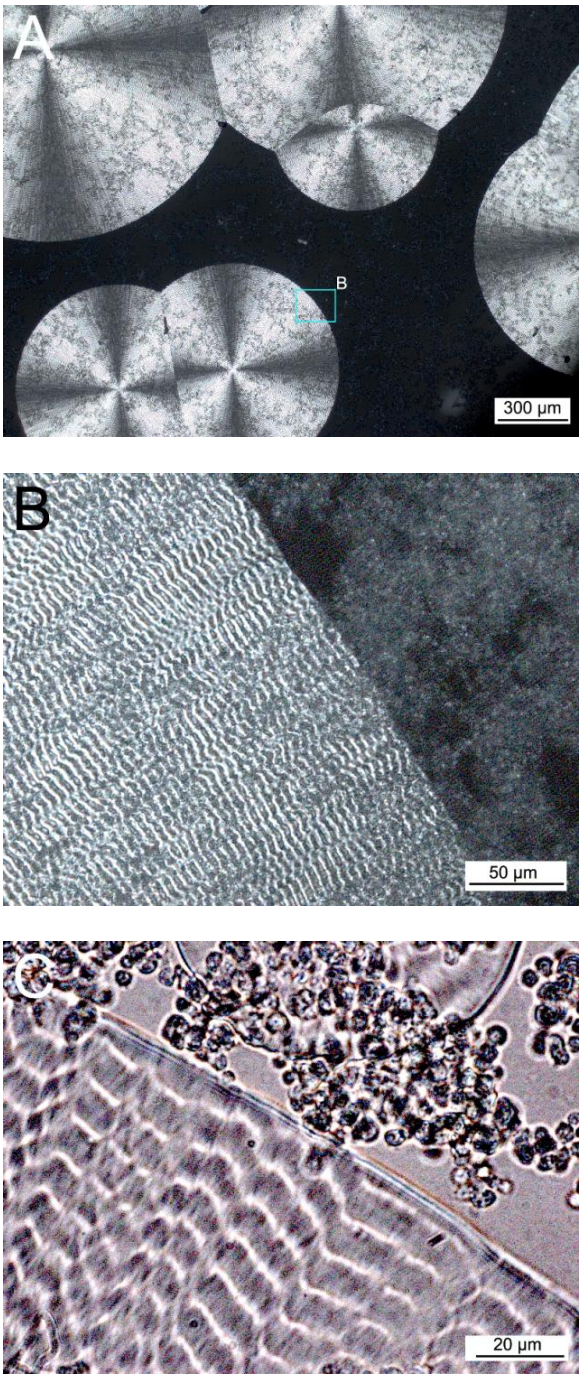

PHBV 90

Figure 6.13 (a) Figure show decreased size of PHBV90 shpherulites compared to neat PHBV spherulite, (b) show growing spherulites edge and (c) show the tiny PBAT spherulites penetrating into big PHBV spherulites.

PHBV80

Figure 6.14 (a-c) show growing PHBV80 spherulites and presence of tiny PBAT spherulites in the background.

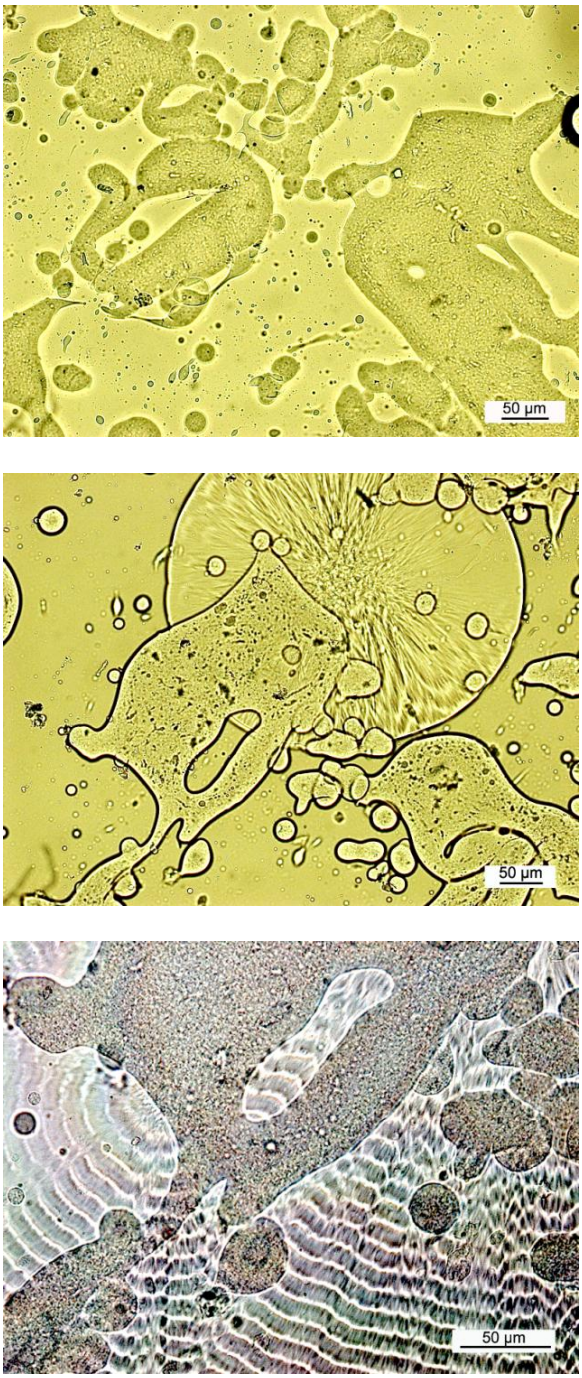

PHBV 70

Figure 6.15 (a) liquid-liquid phase separation in the melt state of PHBV70 blend. (b) Aggregated PBAT phase and growing PHBV spherulite without maltese birefringence pattern and increased band spacing distance. (c) Complete crystallized PHBV70 blend sample with presence of PBAT phase islands.

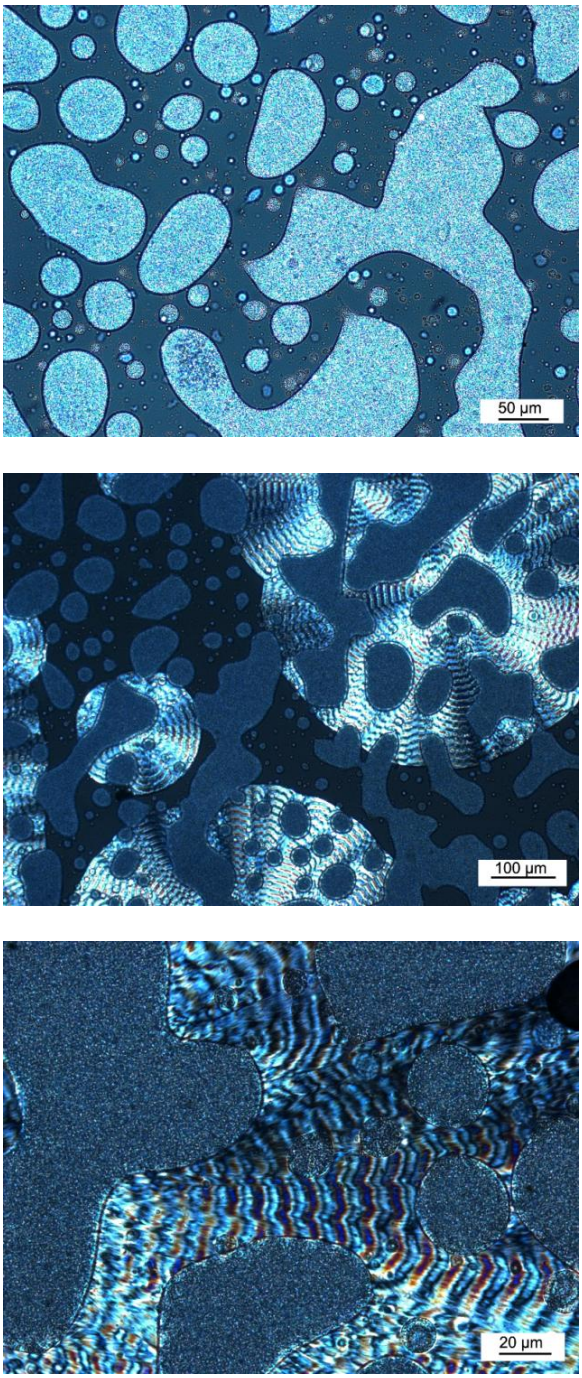

PHBV 60

Figure 6.16 (a) Phase separated PHBV60 blend (crystallizing PBAT phase is bright) (b) PHBV spherulites growing in the background (c) banded structure of PHBV phase

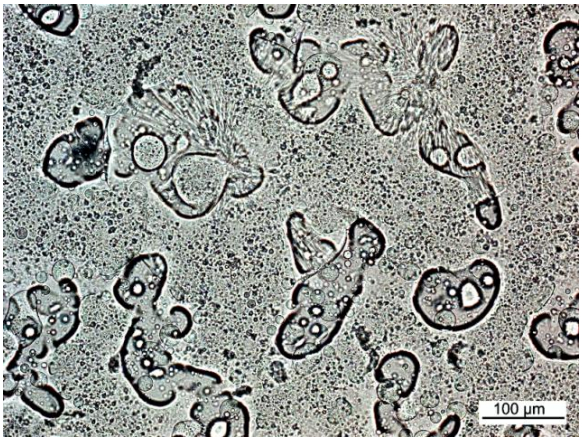

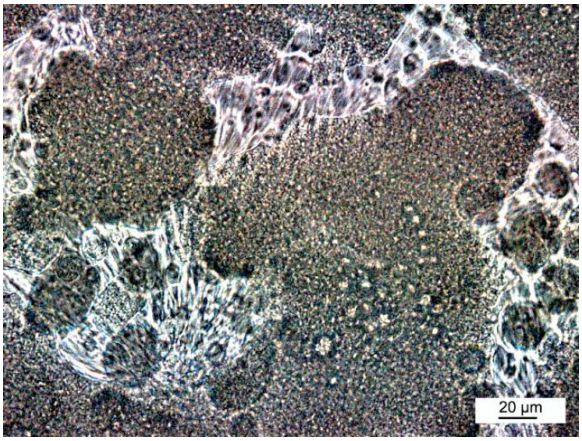

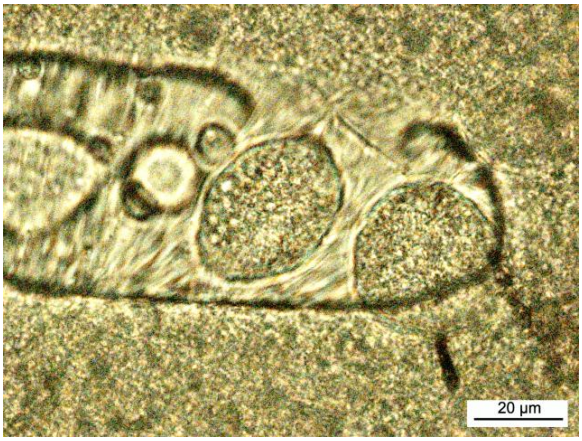

PHBV 50

Figure 6.17 Co-continues morphology of PHBV50 blend with distorted banded structure of unevenly grown PHBV spherulites.

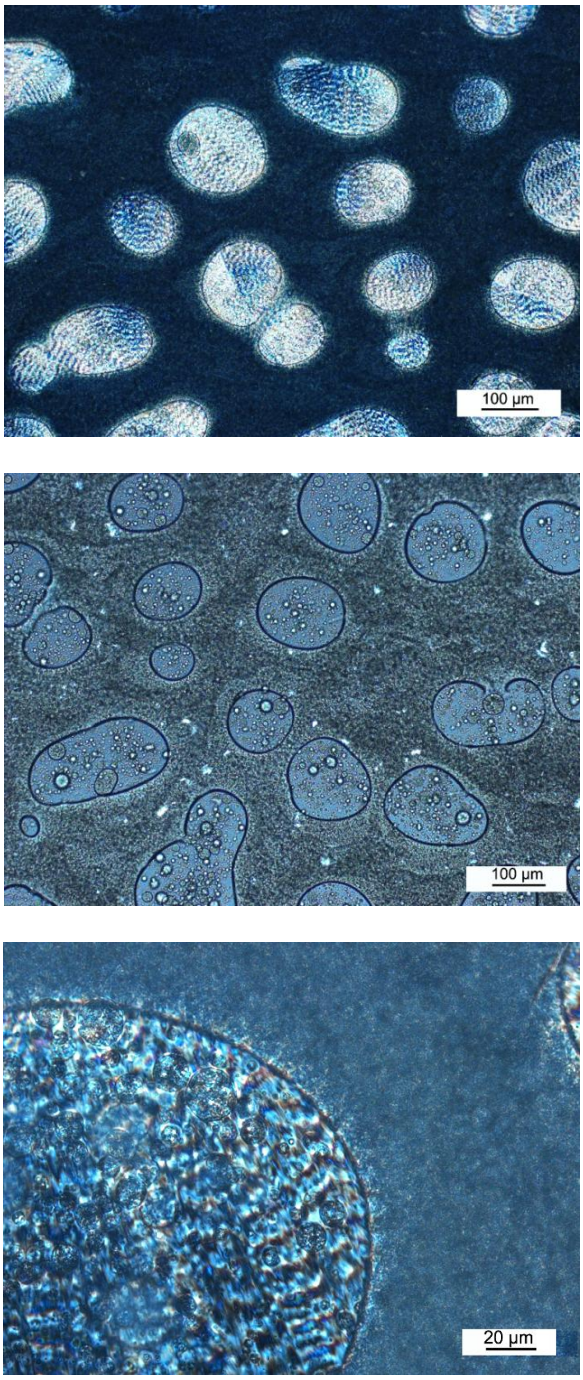

PHBV 40

Figure 6.18 (a) dispersed PHBV phase in PBAT matrix of PHBV40 sample (b) and (c) show PBAT spherulites grown inside the PHBV phase.

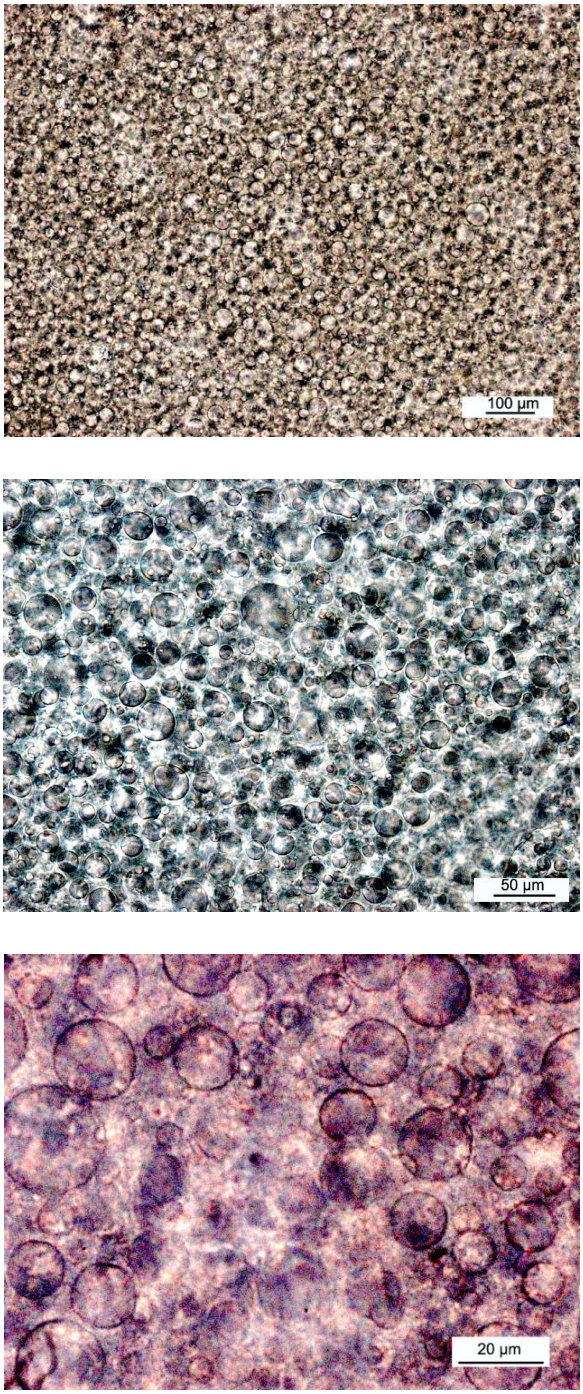

PHBV 30

Figure 6.19 PHBV spherulites in PBAT matrix of PHBV 30 sample

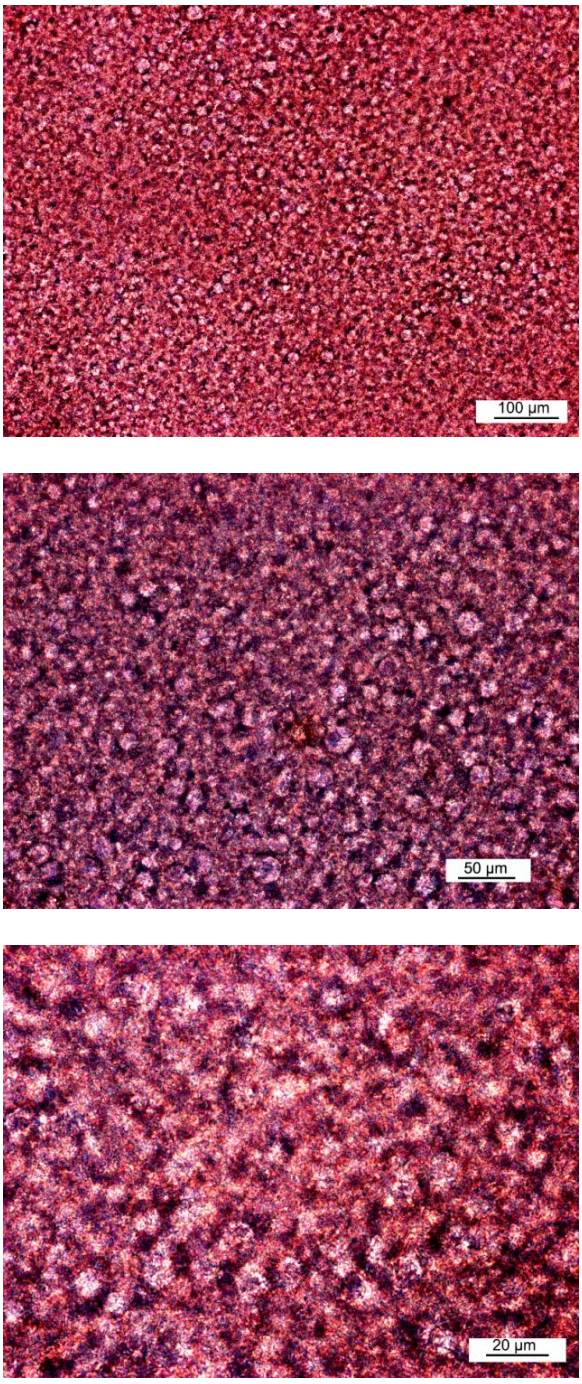

PHBV20

Figure 6.20 Well dispersed PHBV phase in PBAT matrix of PHBV20 sample. PHBV spherulites are bigger and bright compared to PBAT spherulites.

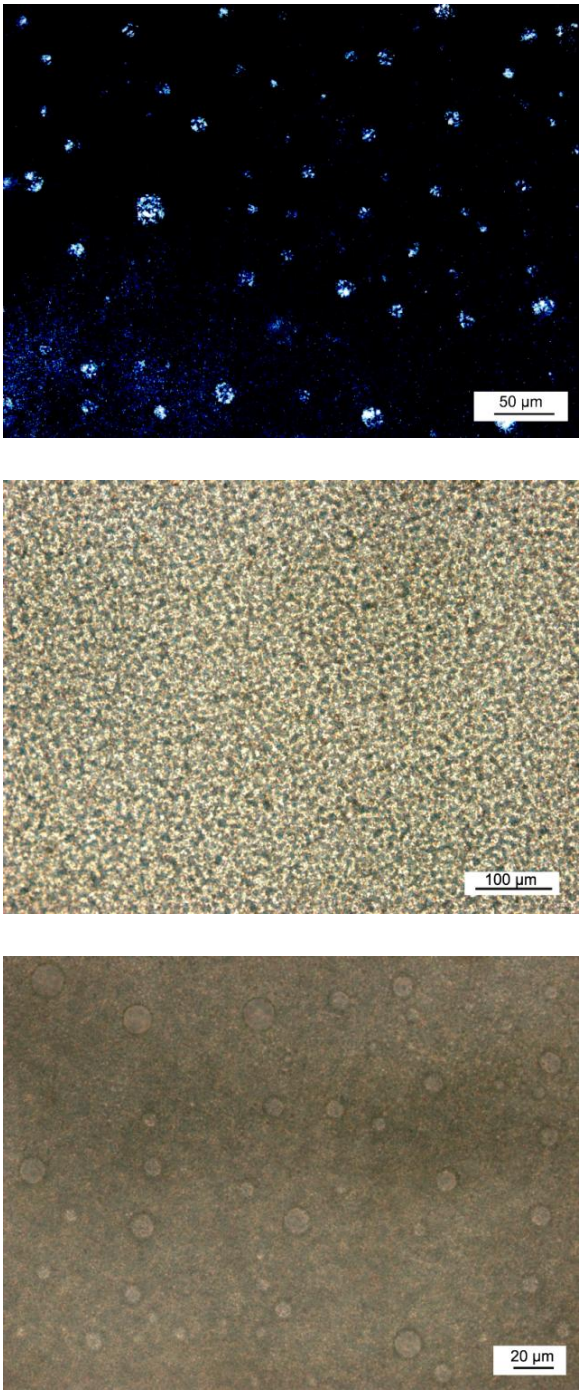

PHBV10

Figure 6.21 Well dispersed and sparkling PHBV spherulites in PBAT matrix of PHBV10 samples.

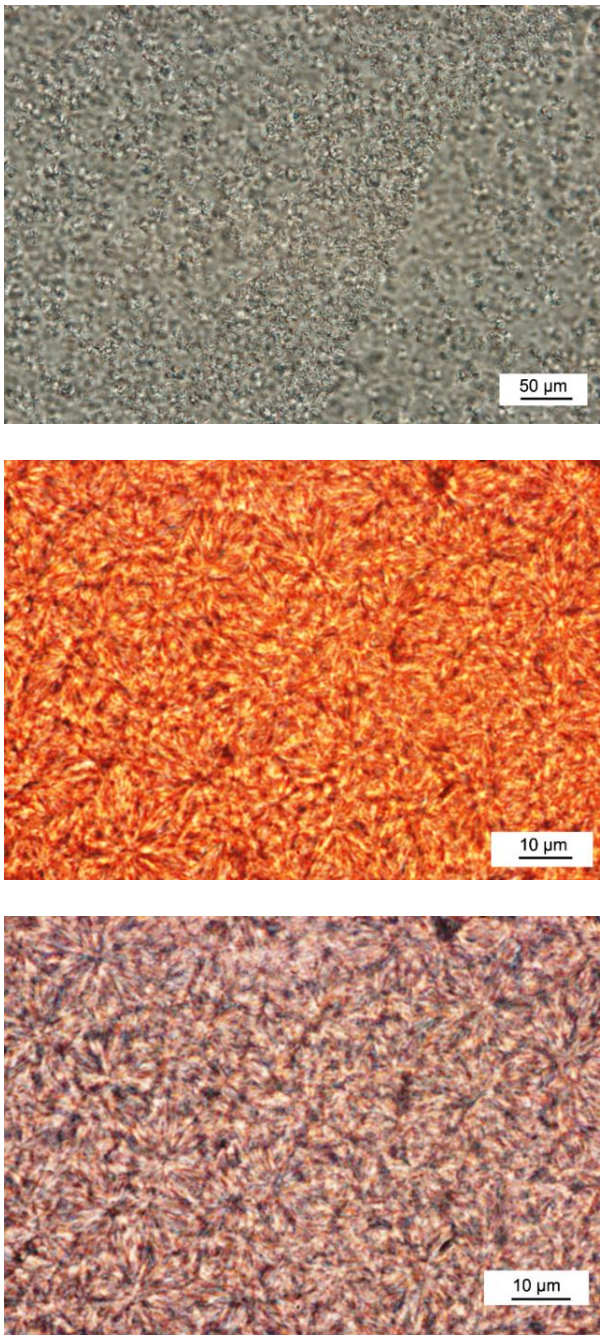

PHBV0

Figure 6.22 Spherulitic morphologies of neat PBAT at 80 °C after complete crystallization.

6.5 Conclusion

The observed bimodal endothermic peak in the PHBV and PHBV/PBAT blends was the result of melting and recrystallization of the crystallites which was confirmed from by the WAXD results. The melting point elevation in the PHBV/PBAT blends was observed with the addition of PBAT. A Single crystallization peak for all the compositions was observed that indicated co-crystallization. One can that PBAT restricted crystallization by interfering with growing PHBV crystals. Overall composition dependent melting and crystallization was observed for PHBV/PBAT blends. Multiple peaks in SAXS diffractograms indicated lamellar stacking in the samples. DSC and SAXS results indicated increased degree of supercooling which resulted in crystal perfection, increased crystal size, and elevation in melting point temperatures. Further, Nishi Wang and Hoffman Weeks equations were used to describe the experimentally observed melting point elevation in binary crystalline/crystalline blends in terms of thermodynamic melting elevation and changes in the lamellar thickness. Morphological structures of blend system were observed by POM and SEM. The results showed phase separation between two polymers but both components affected the microstructure of each other. This supported an inference that there was some interaction between two phases.

Based on composition dependent thermal behavior, change in crystal thickness, effect of surface energy, and phase seperation affecting the macroscopic morphological structure indicated that PHBV/PBAT blend system moves from immiscible (PHBV10-40) to partially miscible (PHBV50-70) to a completely miscible (PHBV80-90) blend system.

6.6 References

[1] Ren J, Fu HY, Ren TB, Yuan WZ. Carbohydr Polym 2009;77:576–582.

[2] Noguchi K, Kondo H, Ichikawa Y, Okuyama KW. J Polymer 2005;46:10823–10830.

[3] Penning JP, Manley RS. J Macromolecules 1996;29:77.

[4] Penning JP, Manley RS. J Macromolecules 1996;29:84.

[5] Liu L, Chu B, Penning JP, Manley RS. J Macromolecules 1997;30:4398.

[6] Lee J, Tazawa H, Ikehara T, Nishi T. Polym J 1998;30:327.

[7] Lee J, Tazawa H, Ikehara T, Nishi T. Polym J 1998;30:780.

[8] Liu A, Liau W, Chiu W. Macromolecules 1998;31:6593.

[9] Chen H, Wang S. Polymer 2000;41:5157.

[10] Hirano S, Nishikawa Y, Terada Y, Ikehara T, Nishi T. Polym J 2002;34:85.

[11] Qiu Z, Ikehara T, Nishi T. Macromolecules 2002;35:8251.

[12] Buzarovska A, Bogoeva-Gaceva G, Grozdanov A, Avella M, Gentile G, Errico M, J Mater Sci 2007;42:6501.

[13] Paital S, Cao Z, He W, Dahotre N. Biofabrication 20010;2:5001.

[14] Van Oss CJ, Good RJ, Chaudhury MK. Langmuir 1988;4:884.

[15] Randeniya LK, Bendavid A, Martin PJ, Amin MS, Preston EW, Ismail FS, Coe S. Acta Biomaterialia 2009;5:1791–7.

[16] Van Oss CJ, Giese RF, Good RJ. Langmuir 1990;6:1711–3.

[17] Morra BS, Stein RS. J Polym Sci Polym Phys Ed 1982;20:2243e59.

[18] Krache R, Benavente R, López-Majada JM, Pereña JM, Cerrada L, Pérez E. Macromolecules 2007;40:6871e8

[19] Galego N, Rozsa C, Sánchez R, Fung J, Vásquez A, Tomas JS, Polymer Testing 2000;19:485-492.

[20] Kunioka M, Tamaki A, Doi Y, Macromolecules 1989;22:694.

[21] Chen GX, Hao GJ, Guo TY, Song MD, Zhng BH. Journal of Materials Science Letters 2002;2 1:1587 –1589.

[22] Qiu Z , Yan C, Lu J, Yang W. Macromolecules 2008;41:141-148.

[23] Maglio G, Malinconico M, Migliozzi A, Groeninckx G. Macromol. Chem. Phys. 2004;205: 946–950.

[24] Tuncer C, Alaslan A, Mehmet SErog, Olgun G. Applied Surface Science 2006;252: 7430–7435.

[25] Keith HD, Padden FJ, Russell T P. Macromolecules1989;22:666.

[26] Keith HD, Padden FJ. Polymer 1984;25:8.

[27] Keith HD, Padden FJ, Lotz B, Wittmann JC. Macromolecules 1989;22:2230.

[28] Bassett DC and Hodge AM. Polymer 1978;19:469.

[29] Barham PJ, Keller A, Otun EL, Holmes P. J Mater Sci 1984;19:2781.

[30] Scott RL. J Chem Phy 1949;17:179.

[31] Nishi T, Wang TT. Macromolecules 1983;16:762.

[32] Runt J, Rim PB, Howe SE. Polymer Bulletin 1984;11:517-521.

[33] Rim PB, Runt J, Macromolecules 1984;17:8.

CHAPTER 7

MECHANICAL AND RHEOLOGICAL BEHAVIOR OF PHBV/PBAT BLENDS

7.1 Introduction

Bacterially synthesized PHBV is being widely studied by researchers due to its potential for a wide range of applications and as a candidate for non petroleum based biodegradable polymers [1]. PHBV is a linear aliphatic biodegradable thermoplastic polyester. Commercial use of PHBV is still limited due to its high cost, brittleness, and low processing window. For many applications flexibility of polymer at low temperature is required. The incorporation of hydroxyl valerate (HV) units during the fermentation process improves flexibility and processing window. Thus by controlling the number of HV units in PHBV copolymer, the polymer can be tailored for specific applications [2]. The second approach to improve the above properties is by making blends of PHBV with another suitable polymer [3, 4]. As discussed in previous chapters, PBAT is chosen as a suitable flexible and high impact polymer to make blends with PHBV. PBAT is an aliphatic aromatic polyester, which is also biodegradable like PHBV. The tensile testing showed the blends have decreased tensile strength and modulus; however, elongation and toughness were dramatically increased. The failure mode changed from brittle fracture of the neat PHBV to ductile fracture of the blends. PBAT also degrades under suitable conditions with the aid of micro-organism enzymes [5]. PHBV and PBAT polymers and their blends can be processed by extrusion and injection molding to form usable products. Therefore their rheological properties, especially its viscosity, have important effect on thermal processing. Rheological parameters such as viscosity, elastic, and loss modulus of blend components have remarkable influence on the phase

structure of the blends [6]. In this work, mechanical, dynamic mechanical and rheological studies on PHBV/PBAT blends are conducted. The studies of melt rheological properties are not only important to understand the knowledge of the processability of these materials, but also are helpful to find out the structure–property relationship in blends.

Time-Temperature Superposition

In order to estimate the thermorheological state of the system, rheological analysis of the system has been done. This includes the utilization of viscoelasticity for the property prediction, the basis for the superposition and derivative classes of thermorheological systems. Since polymers have an elastic and viscous component in their deformation response the theory of viscoelasticity evolves to account for both effects.

$\sigma_{xy} = \eta\ (\partial e_{xy} / \partial t)$……. viscous contribution (7.1)

$\sigma_{xy} = G\ e_{xy}$……..…….elastic contribution (7.2)

In 1874, Boltzmann presented the fundamental linear equation of viscoelasticity. Mathematically the strain response to an applied load is given by the equation 7.3 and the stress response to an applied strain is given by the equation 7.4.

$$\gamma(t) = \left[\frac{\sigma}{Gu}\right] + \int_{\infty}^{t} J\ (t-\tau)\frac{d\sigma(\tau)}{d\tau}dt \quad (7.3)$$

$$\sigma(t) = [Gr\ \gamma] + \int_{\infty}^{t} G\ (t-\tau)\frac{d\gamma(\tau)}{d\tau}dt \quad (7.4)$$

where J(t) is the creep compliance, Gu is the unrelaxed storage modulus, Gr is the relaxed storage modulus, $\frac{d\sigma(\tau)}{d\tau}$ represents the incremental stress corresponding to

the time increment $\tau.\sigma(t)$is given by the equation 7.4. The elastic and viscous contributions are separated by using complex variables of

G* =G'+I G" where G' is the elastic contribution and G" is the viscous contribution. Based on a simple Maxwell model, a spring and dashpot in series G' and G" are expressed as equation 7.5 and 7.6 where τ is the relaxation time, ω is the frequency and Em corresponds to the modulus of the spring element in the Maxwell model.

$$G' = Em\,\frac{\omega^2\tau^2}{1+\omega^2\tau^2} \tag{7.5}$$

$$G'' = Em\,\frac{\omega\tau}{1+\omega^2\tau^2} \tag{7.6}$$

The molecular basis for tTs using the Rouse bead and spring model which is given by

$$G' = \frac{\rho RT}{M}\sum_p \frac{\omega^2\tau_p^2}{1+\omega^2\tau_p^2} \tag{7.7}$$

$$G' = \frac{\rho RT}{M}\sum_p \frac{\omega\tau_p}{1+\omega^2\tau_p^2} \tag{7.8}$$

$$tan\delta = \frac{1}{\omega\tau_p} \tag{7.9}$$

$$\tau_p = \frac{6n_0M}{(\pi p)^2\rho RT} \tag{7.10}$$

where ρ is the density, G' is the storage modulus, G" is the loss modulus, and tanδ is the ratio of G"/ G'.

Activation Energy

For the thermorheologically simple materials at temperatures less than the glass transition, the shift factor temperature curve follows an Arrhenius relationship as

indicated by the equation 7.11. Above the glass transition, substantial effects of free volume make the activation energy a function of temperature and the relationship is expressed by Williams- Landel and Ferry equation (equation 7.12).

$$\ln aT = \frac{Ea}{R}\left(\frac{1}{T} - \frac{1}{T_{ref}}\right) \tag{7.11}$$

$$\ln aT = \frac{c1(T-Tr)}{(c2+T-Tr)} \tag{7.12}$$

The constants c1 and c2 are dependent on the choice of the reference temperature for shifting.

7.2 Experimental

7.2.1 Materials and Blends Preparation

PHBV (Enmat® -Y1000) was supplied by Tianan Biologic Material Co., Ltd. Ningbo, China and and PBAT (Ecoflex® F BX 7011) was supplied by BASF. The details of materials and blend preparation by melt blending are given in Chapter 6. Rheology sample disks of 25 mm diameter were prepared by compression molding at 180 ^{o}C and then vacuum dried at 50 ^{o}C for 24 hours before testing.

7.2.2 Dynamic Mechanical Analysis (DMA)

The dynamic mechanical properties of the PHBV/PBAT blends were measured using a DMA (Rheometric Solid Analyzer 3, TA instruments, USA) with a rectangular measuring system, operating in the tensile mode. Compression molded film samples were used for testing. In phase storage modulus (E') and out of phase loss modulus (E") were measured at fixed frequency of 1 Hz with a strain amplitude of 0.1% (determined from the strain amplitude sweep test) and the heating rate of 3 ^{o}C/min. The gauge length of 10 mm was maintained for all the samples and the temperature was ramped

from -60 ^{o}C to 60 ^{o}C while testing. Three samples of each composition were tested to see reproducibility of viscoelastic response.

7.2.3 Tensile Testing

The uniaxial tension tests were performed on a MTS 810 Material Test System (MTS, Eden Prairie, MN, USA), in which the upper platen was fixed and the lower platen was mobile. The tests were done at a strain rate of 5 mm/min. The axial force and the displacement data were recorded. Tensile properties were measured using films of 50x5x0.2 mm3. An average of 3 tests was chosen as the tensile test value.

7.2.4 Rheological Measurement

Rheological testing was done using a TA instrument Ares strain controlled rheometer. Rheological experiments were performed at 150 to 160 ^{o}C temperature range using 25 mm parallel plate geometry. To determine the limits of linear viscoelastic properties of the melts, dynamic strain sweeps were performed. To determine the linear viscoelastic limits of PHB/PBAT blends, the dynamic strain sweep measurements were performed at 160 ^{o}C and a frequency of 6.25 rad/s. During the frequency temperature sweep, frequency sweeps ranged from 0.1 to 100 rad/sec was used by conducting three sequential sweeps at different temperatures. The gap between parallel plates was set at 0.5 mm. To obtain reasonable signal intensities even at evaluated temperature or low frequency and avoid non-linear response, the strain amplitude for dynamic measurements was fixed at 10%, and elastic moduli (G'), loss moduli (G"), and complex viscosities (η*) were obtained.

7.3 Results and Discussion

7.3.1 Dynamic Mechanical Analysis

E' Vs Temperature

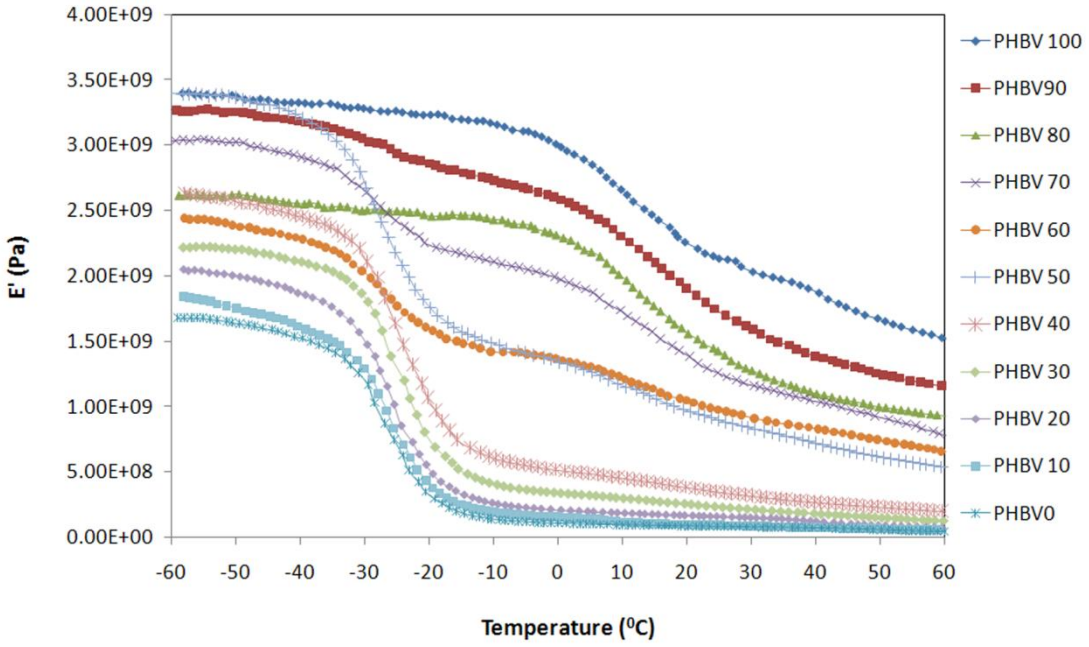

Figure 7.1 E' vs temperature for PHBV/PBAT blend

Fig. 7.1 shows an elastic response (E') of the PHBV/PBAT blends with temperature under dynamic conditions. PBAT rich blend compositions display a sudden fall in elastic modulus at a temperature around -22 ^{o}C, which corresponds to the glass-rubber transition of butylene adipate segments of the aromatic triblock PBAT copolymer. The presence of PHBV exerts strong influence on the modulus in the rubbery region. With an increase in the PHBV concentration increased modulus was observed due to presence of rigid aliphatic PHBV chains.

E'' and Tan δ Vs Temperature

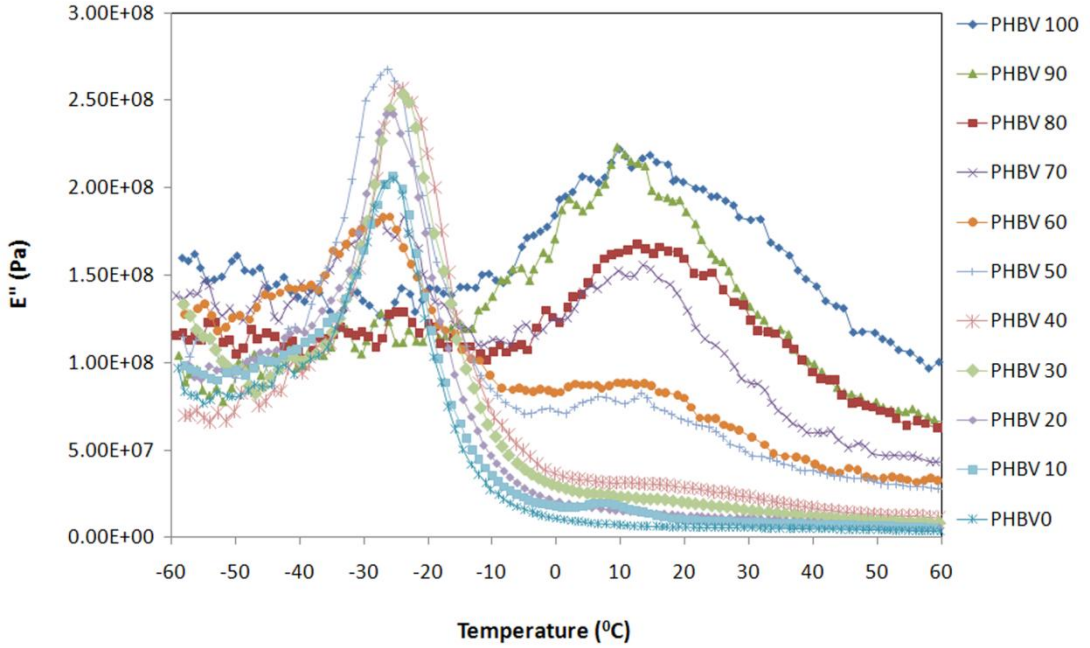

Figure 7.2 E" vs temperature for PHBV/PBAT blend

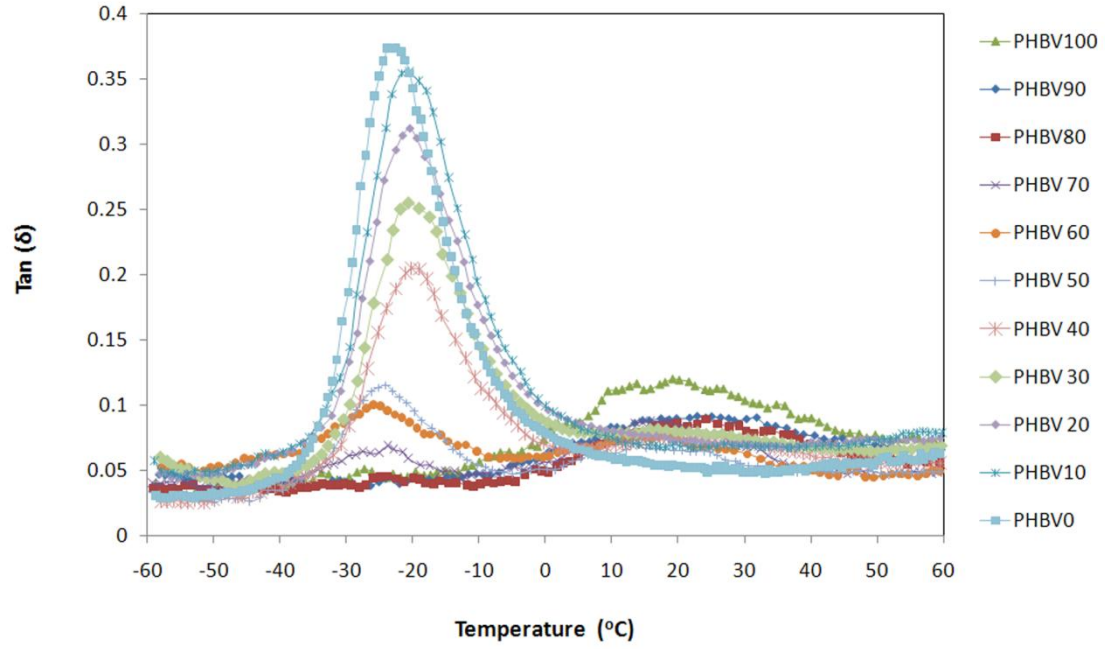

Figure 7.3 Tan δ vs temperature for PHBV/PBAT blend

The E" and loss tangent (tan δ) values of the PHBV/PBAT blend compositions as a function of temperature (-60 to 60 ^{o}C) at 1 Hz are presented in Fig. 7.2 and 7.3 respectively. The values of glass transition temperature (T_g) are obtained from the temperature corresponding to peak tan d_{max}. In this study, the difference in T_g values of blends components viz., PBAT – 23 ^{o}C and PHBV 20 ^{o}C respectively is higher than the 20 ^{o}C and hence miscibility of the blends can be ascertained using this T_g values. In the case of PHBV0 to PHBV30 blends, a single T_g temperature was observed indicating miscibility of blends (Fig. 7.4). Also, it was observed that T_g increased with increase in PHBV concentration due to miscibility of blends and the absence of any phase inversion in these blend compositions. The decreased values of tan δ peak with increase in concentration of PHBV suggested a change in the crystallinity of the blends in this composition range.

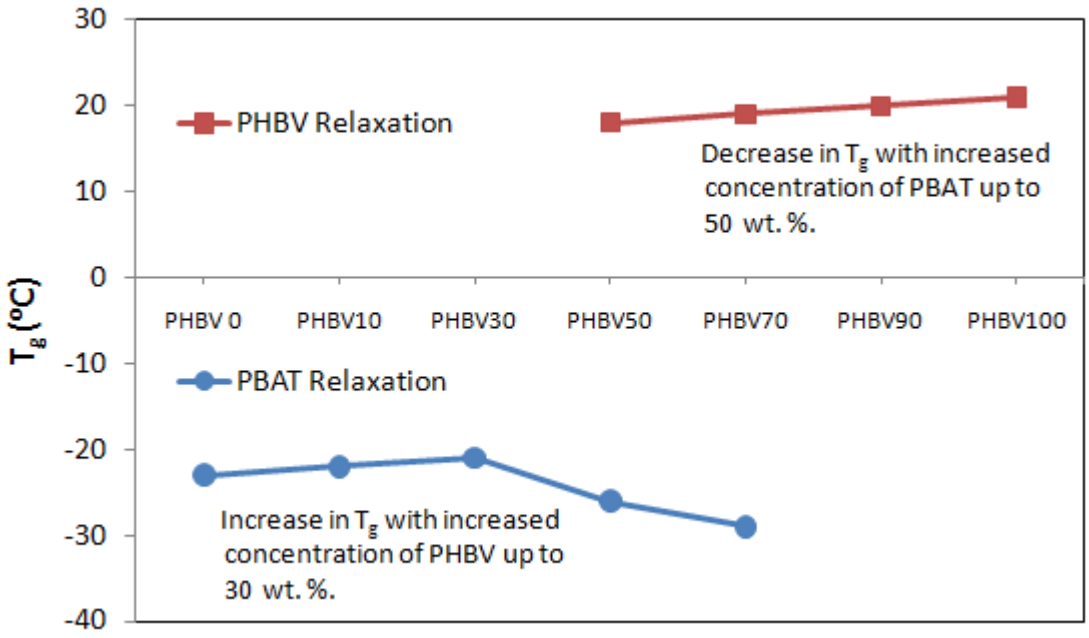

Figure 7.4 PHBV/PBAT blends concentration dependence of T_g

The blend compositions containing more than 30 wt % of PHBV showed two distinct transitions: one near -25 ^{o}C, which corresponds to the glass-rubber transition of the flexible elastomeric PBAT phase and the other at around 20 ^{o}C, related to the transition of the hard rigid PHBV phase. The presence of PHBV in blends significantly dropped the tan d peak values with its increase in the concentration and also affected the corresponding temperature where this transition took place. The effect of PHBV concentration on damping values of the PBAT phase is shown in Fig. 7.5.

The circular symbol line represents the theoretical values, calculated by adopting the mixing rule, as follows.

$$\tan \delta_{mixture} = \tan \delta_{PBAT} \times X \qquad (7.13)$$

where tan δ_{PBAT} and tan $\delta_{mixture}$ are the damping values of pure PBAT phase and the mixture, respectively, and X is the weight fraction of PBAT in the mixture.

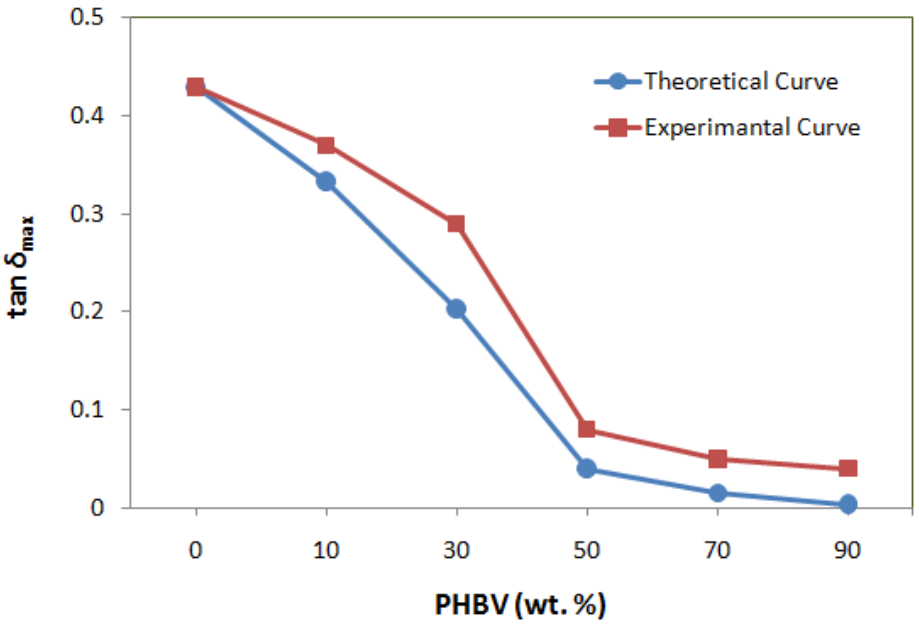

Figure 7.5 Theoretical and experimental Tanδ values for PHBV/PBAT blends

In both theoretical and experimental curves, the damping value decreased as the amount of PHBV increased due to an increase in concentration of rigid PHBV chains. However, the experimental values of damping were higher than the theoretical, indicating increased mobility of the PBAT phase in the presence of PHBV, which exhibits a glass transition at a temperature much higher than the T_g of the PBAT segment. Concerning the transition of the PHBV segments the damping values were not significantly affected by the presence of PBAT as in the case of PBAT relaxation. Only a small decrease on damping (around 0.02) with the addition of 50 wt % of PBAT was observed. This indicates that the PHBV influenced PBAT amorphous regions more than the PBAT influenced PHBV's amorphous fractions.

The heterogeneous distribution of PHBV inside the PBAT matrix can be estimated using the normalized plot of the relaxation process associated to the PBAT phase, taken at different blend compositions [7]. The extent of broadening of these plots with the addition of PHBV can be correlated to the degree of heterogeneity of the corresponding phase. The normalized plots of tan δ/tan δ_{max} against T/T_{max} for glass–rubber transitions of both PBAT segments at different blend compositions are presented in Fig. 7.6 (a), where tan δ represents the value of loss tangent at any temperature T and tan δ_{max} represents the loss tangent value at the corresponding T_{max} temperature. The width of these normalized plots indicates the heterogeneity of the phases. It can be observed from the Fig. 7.6 (a) that the presence of the PHBV phase in PBAT has resulted in a broadening of the normalized glass-rubber transition of PBAT segments. The addition of PHBV up to 30 wt. % into PBAT has not affected the broadening of the peak indicating the homogenous blend system. The broadening of the peak can be

seen above the 30 wt. % concentration of PHBV, suggesting the heterogeneity of the system.

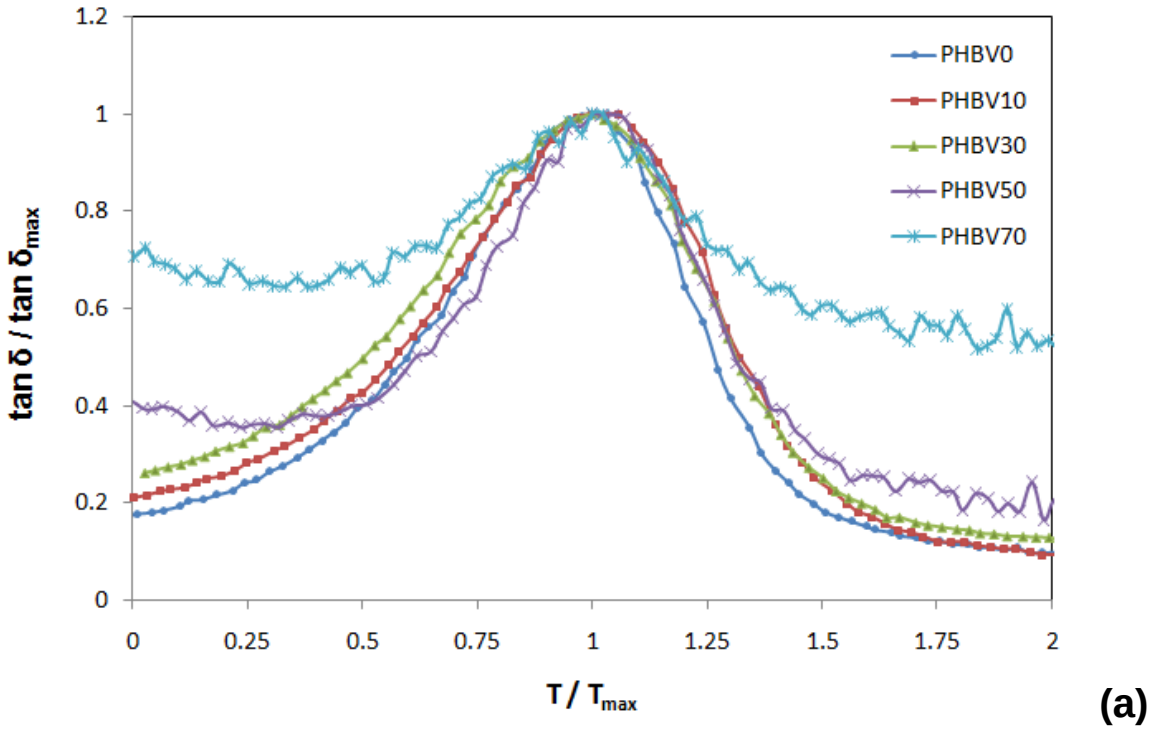

(a)

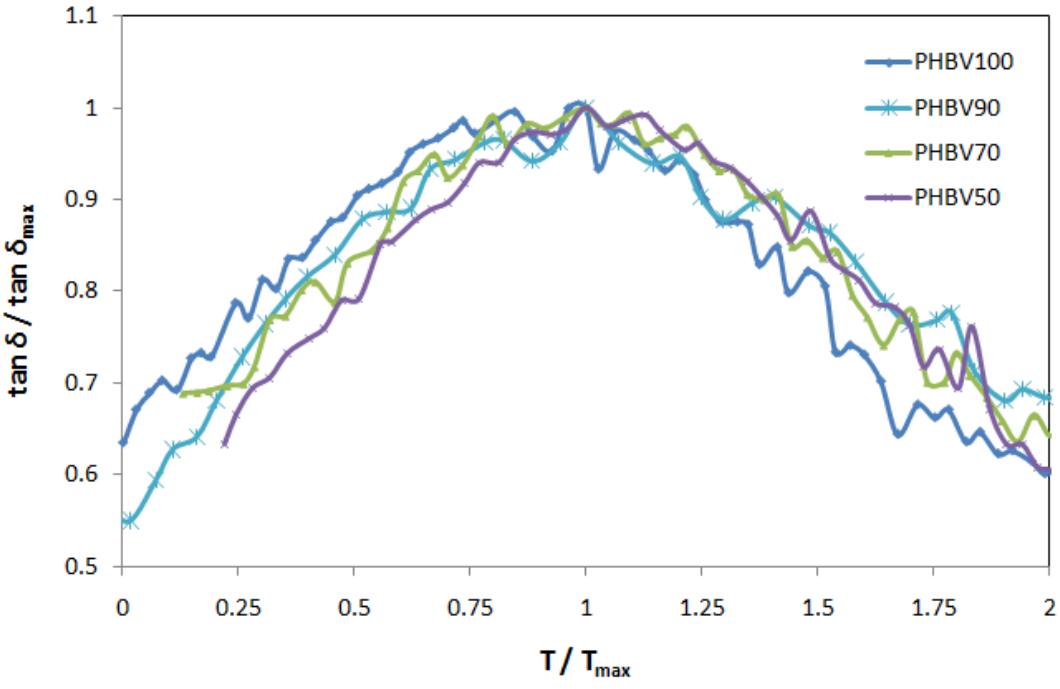

(b)

Figure 7.6 Normalized plots of the (a) PBAT (b) PHBV relaxation process

The normalized plots of tan δ/tan δ_{max} against T/T_{max} for the relaxation processes of PHBV phase of at different compositions are shown in Fig. 7.6 (b). The profile of the normalized curves related to PHBV does not show any considerable broadening effect by addition of PBT phase in PHBV indicating good affinity and compatibility between two phases.

7.3.2 Tensile Testing

Fig 7.7 and Table 7.1 shows the tensile strength and modulus of the PHBV/PBAT blends. The Young's modulus was determined as the slope of the linear region of the stress-strain curve at very small elongations. Polymers at small elongation are considered to be at equilibrium condition with isotropic or randomly arranged chain structure. Beyond this region the slope of the stress-strain curve becomes non-linear and becomes independent of the sample's elasticity. PHBV and PHBV rich blend samples showed highly brittle behavior with high yield stress values but very low elongation at break. With the addition of rubber like (low slope of stress-strain curve and very high elongation) PBAT in PHBV, the elongation at break improved considerably from 2% for pure PHBV to 380% for PHBV50 sacrificing yield stress and modulus values. The yield stress values reduced from ~30 MPa for pure PHBV to ~20 MPa for PHBV 50. The Young's modulus reduced from ~2934 MPa for pure PHBV to ~263 MPa for PHBV50. The yield stress values further increased to ~34 MPa for pure PBAT from ~20 MPa for PHBV50 while modulus continuously went down with increase in rubbery PBAT content. The elongation at break for the samples having more than 50% or more PBAT content was more than 800% which crossed the measuring ability of the machine. The crystallization of PBAT component within the confinement of PHBV

crystals was important with respect to improved mechanical properties of crystalline/crystalline polymer blend.

Table 7.1 Tensile properties of PHBV/PBAT blends

Composition	Yield Strength (MPa)	Modulus (MPa)	Elongation at break (%)
PHBV 100	29.3 ± 1.6	2934 ± 52	2
PHBV90	29.8 ± 1.2	1680 ± 63	3
PHBV80	27.3 ± 0.8	1260 ± 46	12
PHBV70	24 ± 1.3	367 ± 24	13
PHBV 60	20.3 ± 1.4	338 ± 20	200
PHBV 50	19.9 ± 1.2	263 ± 10	380
PHBV 40	24.5 ± 0.9	113 ± 13	>800
PHBV 30	25.9 ± 1.2	80 ± 6	>800
PHBV 20	30 ± 0.8	148 ± 8	>800
PHBV 10	31.6 ± 0.9	160 ± 4	>800
PHBV 0	32.9 ± 1	89 ± 7	>800

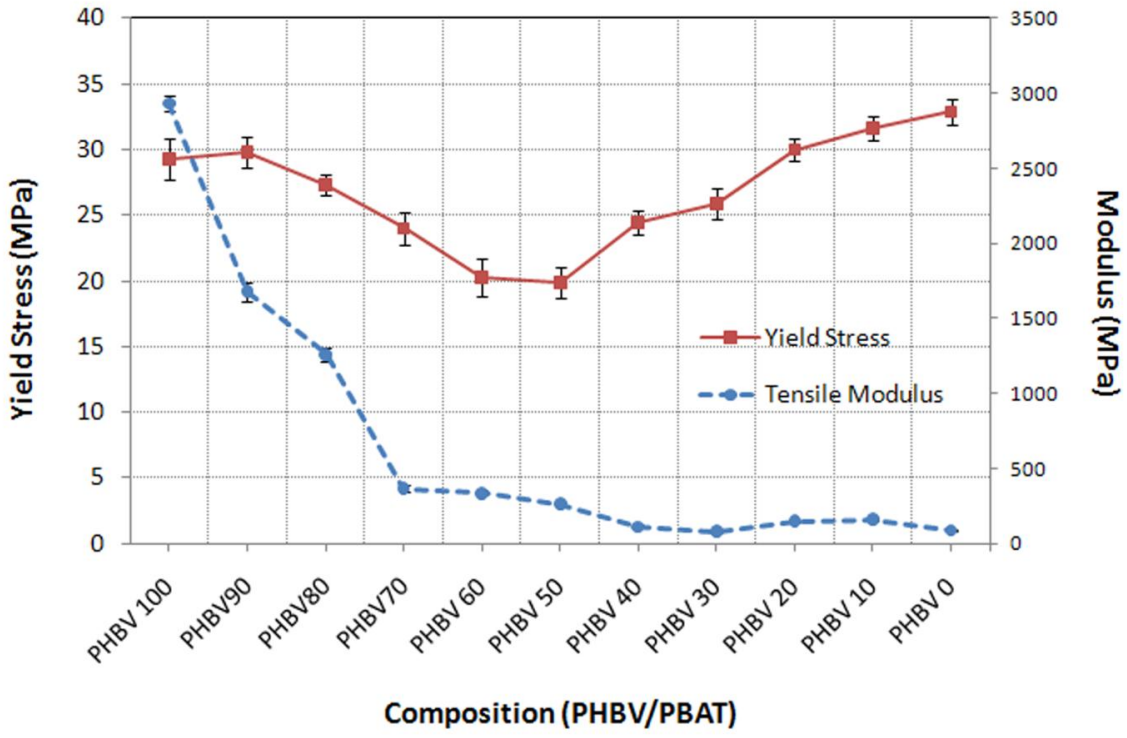

Figure 7.7 Tensile yield strength and modulus of PHBV/PBAT blends

7.3.3 Rheology

7.3.3.1 Dynamic Modulus Analysis

The results of storage modulus (G'), and loss modulus (G") as a function of angular frequency (ω) obtained for PHBV/PBAT blends are shown in Fig. 7.8. The incorporation of PBAT showed an effect on the storage moduli (G') and loss moduli (G") of melts over whole range of frequencies. PBAT is a copolymer of butylenes, adipate, and terephthalate. The molecular chains of PBAT are more flexible than PHBV and are easier to entangle. The entanglement density of PBAT is higher than that of PHBV, leading to high reversible elastic deformation (G') of the melts. All the blends compositions behave more or less solid-like (elastic) or liquid-like (viscous) depending on the rate at which they are deformed. When the molecules are strained they tend to pull back. The dynamic storage modulus (G') is related to the energy storage and dynamic loss modulus (G") represents energy dissipated. The G' and G" values of all the blends increase with increase in frequency.

PHBV10 to 30 shows higher G' and G" values than pure PBAT. Smaller dispersed phase could store more recoverable energy than continuous phase. Therefore total recoverable energy is greater in the two phase PHBV10 to 30 compositions. The higher interaction between these two phases would also have increased G'' values.

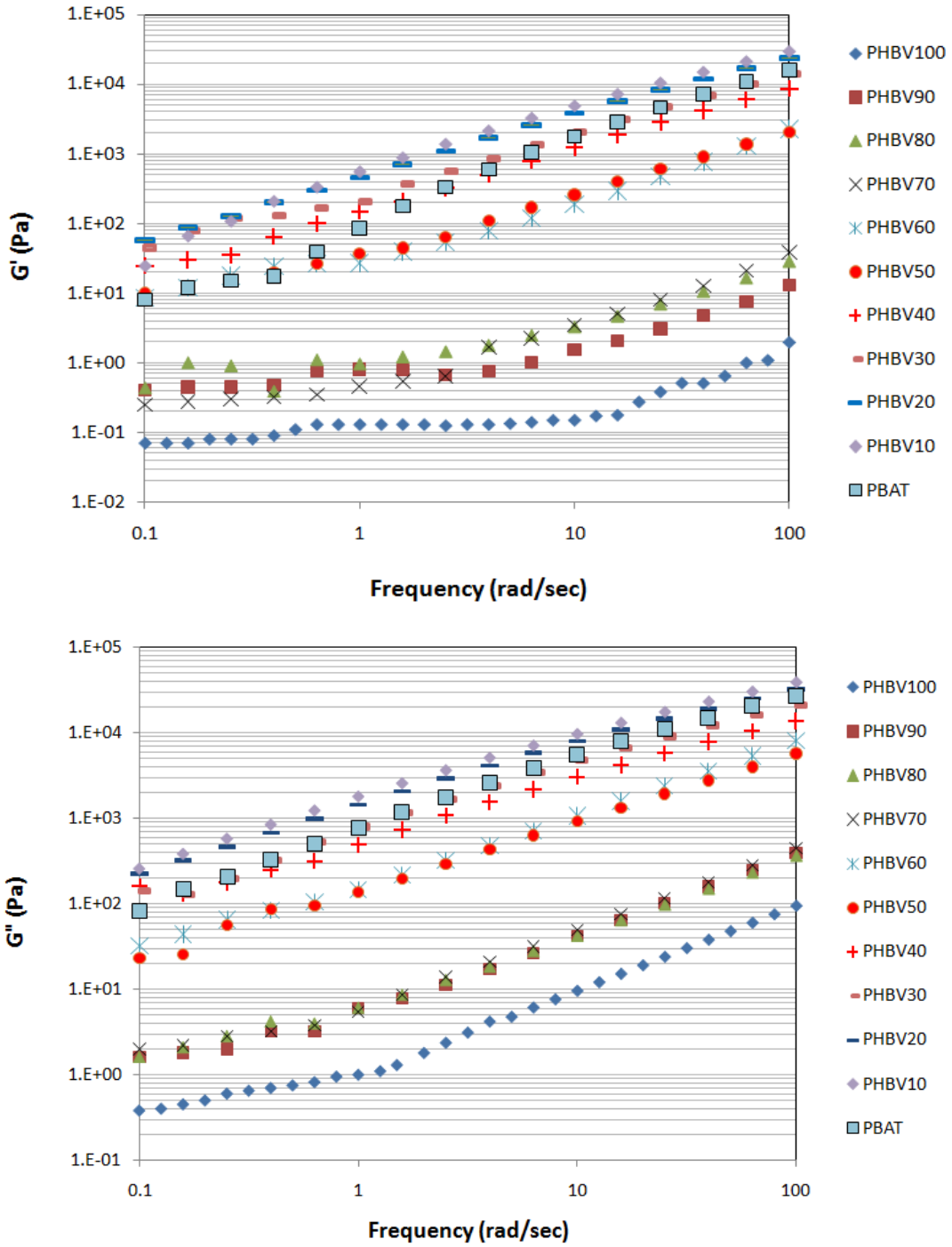

Figure 7.8 Concentration dependence of (a) G' and (b) G"

7.3.3.2 Dynamic Complex Viscosity Analysis

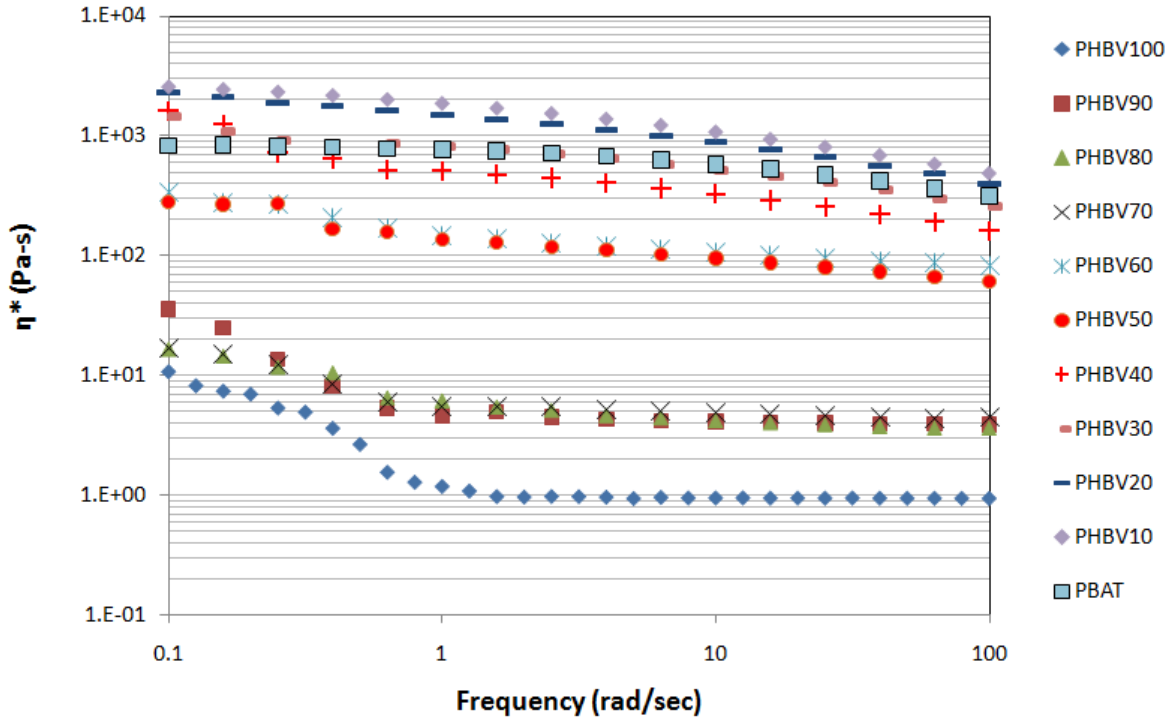

Figure 7.9 Influence of PBAT on η of PHBV/PBAT blend melt (T = 160 °C).

The onset and end melting curve temperatures of PHBV are 150 10 172 °C. Considering the low thermal stability and very low viscosity of PHBV, 160°C temperature was selected as a reference temperature for rheological measurements. The dependence of complex viscosity values (η*) on logarithm of frequencies is shown in Figure 7.9. All samples at low frequency range present higher complex viscosity values than that at high frequency range. It can be noted that the PHBV has significantly lower viscosity than the blend compositions with PBAT. Complex viscosity of pure PHBV and PHBV90, PHBV80 displays a Newtonian liquid behavior at the frequency of

1 to 100 rad/sec. PBAT rich compositions show higher viscosity at all the frequency ranges.

The higher the frequency, the higher is the shear rate. According to Graessley and co-workers [8, 9] the viscosity at higher shear rate is given by following equation; $\eta = \text{constant} * M^{0.1} |\gamma|^{-3/4}$, which indicates at higher shear rate viscosity is weak function of molecular weight and is proportional to $|\gamma|^{-3/4}$. Therefore decrease in viscosity can be attributed to decrease in the entanglement of the polymer network.

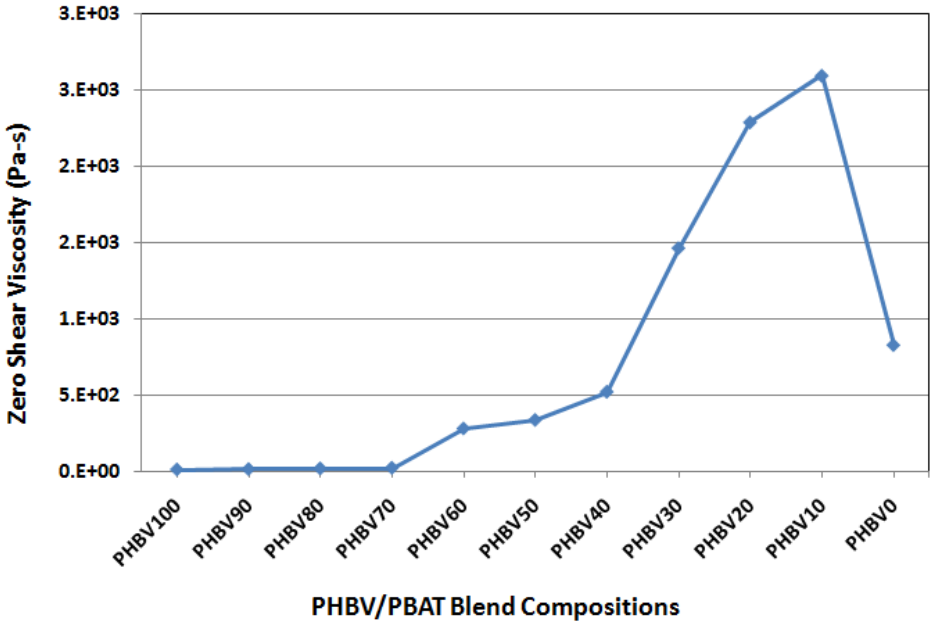

Figure 7.10 PHBV/PBAT blend concentration dependent zero shear viscosity

The results of linear viscoelastic studies, applied in small amplitudes, can provide reliable information on microstructure of the blends [10]. At low concentration of PBAT, dispersed phase form separate swollen coils that do not interpenetrate each other. The transition from dilute solution of independent moving coils to enlarged network is usually accompanied by a drastic increase in the concentration dependent viscosity. The increase in the viscosity indicates the onset of significant coil overlapping and

interpenetration. Figure 7.10 show the concentration dependence of zero shear viscosity. At PHBV40 zero shear viscosity shows a remarkable increase at PHBV40 concentration. Utracki has showed that this type of behavior is observed for the blends in which the interfacial interaction between phases is affected by the blend composition [11]. The viscosity at this composition deviates from linearity and the slope change significantly as a consequence of the great interpenetration of the polymer macromolecules.

In polymer blends, in addition to the characteristics of the component polymers, the rheological behavior also depends on the interfacial adhesion [12]. The inter layer adhesion or interfacial properties of the components determines the rheological properties of the blends. The individual PHBV and PBAT has different chain entanglements. From the rheological measurements and structural point of view PBAT rich blends show higher chain entanglement and higher viscosities. When shear stress is applied to a blend, it undergoes elongational flow. If the interface is strong, the deformation of the dispersed phase is effectively transferred to the continuous phase. In the same way if the interface between two components is weak then interlayer slip occurs as a result, the viscosity of the system decreases [13, 14]. Thus when the PHBV content is higher than 30 wt%, the blends show immiscibility and the interaction between PHBV and PBAT is small. Therefore, the viscosity of PHBV/PBAT blends decreased with PHBV content. Another perspective is that as the PHBV % increased, end to end distance between PBAT coils increased, reducing the occurrence of interaction between PBAT molecules, and the viscosity of the blends decreased.

The blends with 10 to 30 wt% of PHBV present a different rheological behavior in relation to others. It was observed that these blends have higher viscosities than pure PBAT at applied frequency. It can be inferred from the present data that there should be certain degree of miscibility between two components at this compositions. In these PBAT rich compositions particles size of the PHBV dispersed phase is smaller enough that PHBV could infiltrate into the matrix phase. Then the interaction and entanglement between the two polymers would have improved to some extent, increasing the melts viscosities. It can be also observed that the viscosity gap of the blends decreased as the frequency increased. At higher frequency range the chain segments align in the shear direction and then viscosity gap of the blends decreased as the frequency increased.

7.3.3.3 Flow Activation Energy

In polymer melt flow, temperature dependence of viscosity is one of the most important parameters. The temperature dependence can be expressed in the Arrhenius form, in a certain range of temperature.

$$\eta_0 = A \exp(E_a/RT)$$

where η_0 is the zero shear viscosity, R is the gas constant, A is a constant, and E_a is called the flow activation energy [15]. The values of activation energy obtained from Arrhenius fit are presented in Figure 7.11. The data obtained at temperature 150-160 ^oC was used for Arrhenius fit. The correlation constant for each fit was better than 0.99. The result indicated that addition of highly viscous PBAT in PHBV increased the activation energy and melt flow became difficult. PHBV50 and PHBV60 composition presented highest activation energy probably due to formation of co-continuous

morphology. When PHBV was present as a dispersed phase in PBAT, lower activation energy was observed. In other words, lower activation energy represents less temperature dependence of viscosity. PBAT rich composition also represented broader processing temperature window due to the less viscosity sensitivity to temperature.

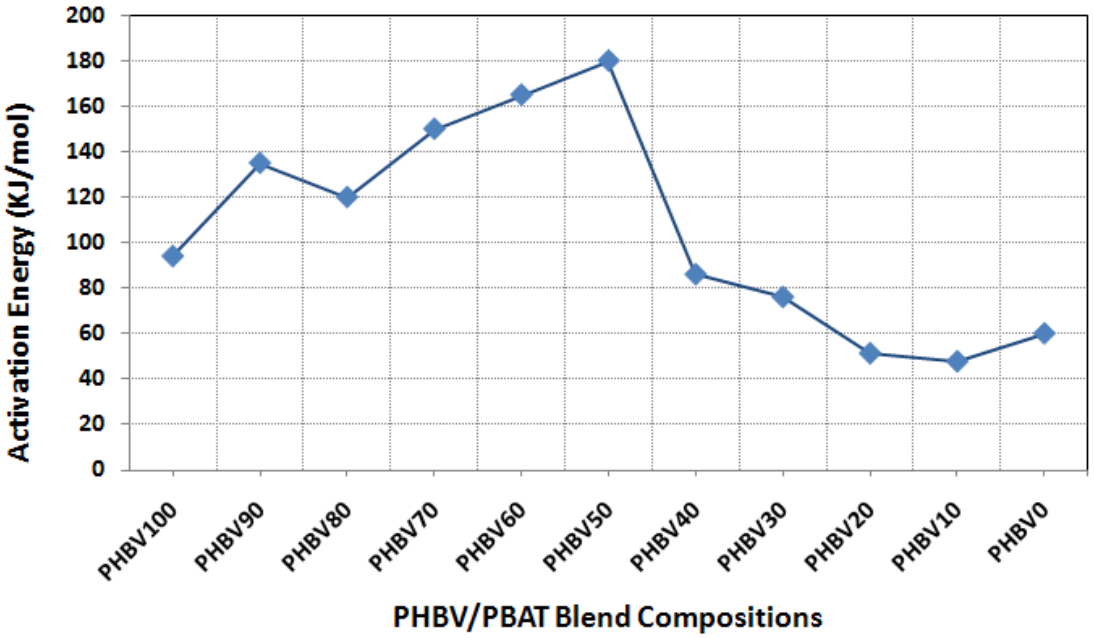

Figure 7.11 Activation energy-composition relationship for PHBV/PBAT blends

7.4 Conclusion

In tensile testing, the elongation at break improved considerably with addition of PBAt. The yield stress values reduced from ~30 MPa for pure PHBV to ~20 MPa for PHBV 50. The Young's modulus reduced from ~2934 MPa for pure PHBV to ~263 MPa for PHBV50. The yield stress values further increased to ~34 MPa for pure PBAT from ~20 MPa for PHBV50 while modulus continuously went down with increase in rubbery PBAT content. Rheological study indicated the immiscible behavior of PHBV/PBAT blends up to PHBV40 composition. However PHBV30 to 10 blends showed miscibility

and increase in the viscosity was observed for these compositions. The storage moduli (G') and loss moduli (G") of the blends increased with the PBAT content. The complex viscosity showed shear thinning behavior of the blends and increased with PBAT content. The viscosity of PHBV30, 20, and 10 compositions showed higher viscosity values than the individual components that indicated the miscibility of the two phases at these compositions. The incorporation of PBAT resulted in gradual increase in activation energy and then reduced at high wt% of PBAT representing compositions with broad processing window and less sensitive towards temperature change.

7.5 References

[1] Laiquan M, Zhaobin Q, Wantai Y, Takayuki I. Reactive & Functional Polymers. 2008;68:446–457.

[2] Hui L, Pancholi M, Stubbs J, Raghavan D. Journal of Applied Polymer Science. 2010;116:3225–3231.

[3] Utracki LA. Commercial polymer blends. New York: Chapman and Hall. 1998; p. 83–94.

[4] Folkes MJ, Hope PS. Polymer blends and alloys. London: Chapman and Hall; 1993.

[5] Kasuyaa K, Ishiib N, Inoueb Y, Yazawab K, Tagayaa T, Yotsumotoa T, Kazahayaa J, Nagaia D. Polymer Degradation and Stability 2009; 94:1190–1196.

[6] Utracki LA. Polymer alloys and blends. Munich Vienna Munich, Vienna, New York: Hanser; 1989.

[7] Olabisi O, Robeson LM, Shaw MT. Polymer–polymer miscibility. New York: Academic Press; 1979. Chapter 5, p. 219

[8] Graessley WW. J Chem Phys. 1965;43:2696.

[9] Graessley WW. J Chem Phys. 1967;47:1942.

[10] Peon J, Vega JF, Amo BD, Salazar JM. Polymer 2003;44(10):2911–8.

[11] Utracki LA. J Rheol 1991;35(8):1615–37.

[12] Ajji A, Utracki LA. Polym Eng Sci 1996;36(12):1574–85.

[13] Asthana H, Jayaraman K. Macromolecules 1999;32:3412.

[14] Shi D, Ke Z, Yang J, Gao Y, Wu J, Yin J, Macromolecules 2002;35:8005.

[15] Gu S, Zhang K, Rena J, Zhan H. Carbohydrate Polymers 2008;(74):79-85.

CHAPTER 8

PIEZORESISTIVE PROPERTIES OF CONDUCTIVE PHBV/PBAT BLEND WITH MULTIWALL CARBON NANOTUBES

8.1 Introduction

One of the current goals of materials research is to create materials with properties tailored to a particular application and to understand how processing determines morphology and end properties. At present, there is a great need to produce polymers with relatively higher conductivity without compromising the desirable mechanical and processing properties [1-5]. Conducting polymers have applications in electronics, smart structures, drug release system, antistatic clothing, etc. Compared to single-polymer composites, the introduction of CNTs into immiscible or compatible polymer blends offers a much higher potential for the development of conductive composites with significantly lower filler concentrations by melt processing.

At some critical concentration of conductive fillers, conductivity in the mixture occurs i.e. the insulative-conductive transition which is of special interest. The common explanation for this drastic mode is formation of conductive path. The filler concentration dependent resistivity response of the polymeric material has been well studied and understood. The addition of conductive fillers increases the conductivity of polymer matrix. The filler concentration dependent conductivity of polymer increase rapidly till concentration reaches to percolation threshold. Upon formation of a conductive network at percolation threshold addition of more filler does not cause further increase in conductivity.

Two morphological scenarios in the blend system can occur by addition of CNTs: either CNTs would localize at the interface of the two polymers or selectively get filled in one of the blend phases. The localization of conductive filler at the interface of two phases is ideal for achieving the lowest possible percolation threshold but it is difficult to achieve this with high aspect fillers like CNTs [6]. The high aspect ratio of CNTs would always make them to reside in one or both the phases while smaller particles can easily stay at the interface between two phases. The localization of smaller particles at the interface can for conductive path easily than the particles mixed in phases. Previous work on polymer/MWCNT composites showed various outstanding properties like, low percolation threshold for electrical conductivity [7], improved piezoresitivity [8], improved strain sensing ability [9], good interfacial adhesion between nanotubes and polymer [10], improved crystallinity [11], etc. In this work, my study is focused on how selective dispersion of CNTs affects the piezoresistivity of the material. So to investigate this, multiwalled carbon nanotubes (MWNTs) were introduced in the blend of poly(hydroxylbuterate-co-valerate) (PHBV) and poly(butylene adipate-co-terephthalate) (PBAT) by melt mixing in a Brabender batch mixer. Blends with dispersed phase of PBAT were prepared by preparing masterbatch of PBAT and CNT and later diluting with PHBV and by mixing all three components together. In both the compositions the 70/30 weight ratio of PHBV/PBAT was used. As noted in Chapter 6, this composition marks a miscible PHBV/PBAT blend that has the best mechanical performance. The CNT content in all compositions was 10 weight %.

8.2 Experimental

8.2.1 Materials

PHBV (ENMAT-Y1000, pure PHBV powder) was supplied by Tianan Biologic Material Co., Ltd. Ningbo, China. PHBV was dried in an oven for 48 hours at 40 ^{o}C. PBAT is available under the trade name of Ecoflex® FBX 7011 was supplied by BASF. MWCNTs (Baytubes® C150 P) were obtained from Bayer MaterialScience (Leverkusen, Germany), with outer number of walls 3-15, outer mean diameter 13-16 nm, inner mean diameter 4 nm, length 1-10 μm and bulk density 140-160 kg/m3. MWCNTs were used as received without further purification. Prior to melt mixing, MWCNTs were vacuum dried at 100 ^{o}C for 4 hours.

8.2.2 Composite Sample Preparation

Three compositions were made using PHBV, PBAT, and MWNTs. 1) PHBV was melt blended with 10 wt. % MWCNTs. 2) PHBV PBAT were taken in the ratio of 70:30 and then MWCNTs with 10 wt. % of the total composition were melt blended together. 3) The masterbatch of PBAT and MWCNTs was prepared and then the masterbatch was diluted in PHBV by melt blending. These three compositions were coded as PHBVCNT10, PHBVPBATCNT10, and MBCNT10, respectively.

Compression molding was used to make samples for electrical measurements. It was done at 190 °C under 10 MPa pressure for 10 min to form samples with a size of 25 × 25 × 3 mm^3. After natural cooling to room temperature (~3 hours), the samples were removed from the metal template. Silver paste and copper mesh was mounted on both surfaces to make better electrical contact.

8.2.3 Resistance Measurements

The compression tests were performed on a MTS 810 Material Test System (MTS, Eden Prairie, MN, USA), in which the upper platen was fixed and the bottom platen was mobile. The two-probe method was used to measure the volume resistance by using Agilent 34410A multimeter. The two-probe method is based on Ohm's law, i.e., V = IR with V, I and R being voltage, current, and resistance between the two electrodes respectively. Since the copper electrode and sample material resistivity difference was significant, a two point over four point measurement configuration was found to be equitable. The compression test was done at the speed of 0.5 mm/min. The axial compressive force and the displacement data were automatically recorded in a computer. For creep testing under compression, the specimen was compressed with a certain axial stress which was maintained during the creep period. Compressive creep tests on the composite samples were performed under axial stress of 32 MPa which is within the elastic limit of all the sample compostions.

8.2.4 Scanning Electron Microscopy (SEM)

The blend morphology of the specimens was observed using FEI Quanta Environmental Scanning Electron Microscope (ESEM; FEI Company, Oregon, USA) at an accelerating voltage of 15 to 20 kV. The SEM samples were prepared by cryo fracturing the compression pressed samples. The fractured surface was then gold coated for better resolution of morphological structure.

8.3 Results and Discussion

8.3.1 Mechanical and Electrical Response under Compression

Compression tests were performed to first determine the maximum yield stress value of the sample. The compression test results for all compositions are shown in Figure 8.1 (a) and (b). It was observed that with 10 Wt. % of CNT compositions the yield stress values did not change significantly. The modulus values showed some changes in the result. The yield stress values for all the composition reached to 105 ± 3 MPa while modulus values for PHBVCNT10, PHBVPBATCNT10, MBCNT10 were 201, 195, and 198, respectively. Even though, the mechanical properties of these three compositions were similar, the electrical response was significantly different. PHBVCNT10 showed electrically conductive behavior while CNT filled PHBV/PBAT compositions showed electrically resistive response. Furthermore the effect of processing can be seen on the resistive response of these two compositions. The composition which was prepared by a masterbatch approach showed more conductivity than the composition which was prepared by mixing all the components together.

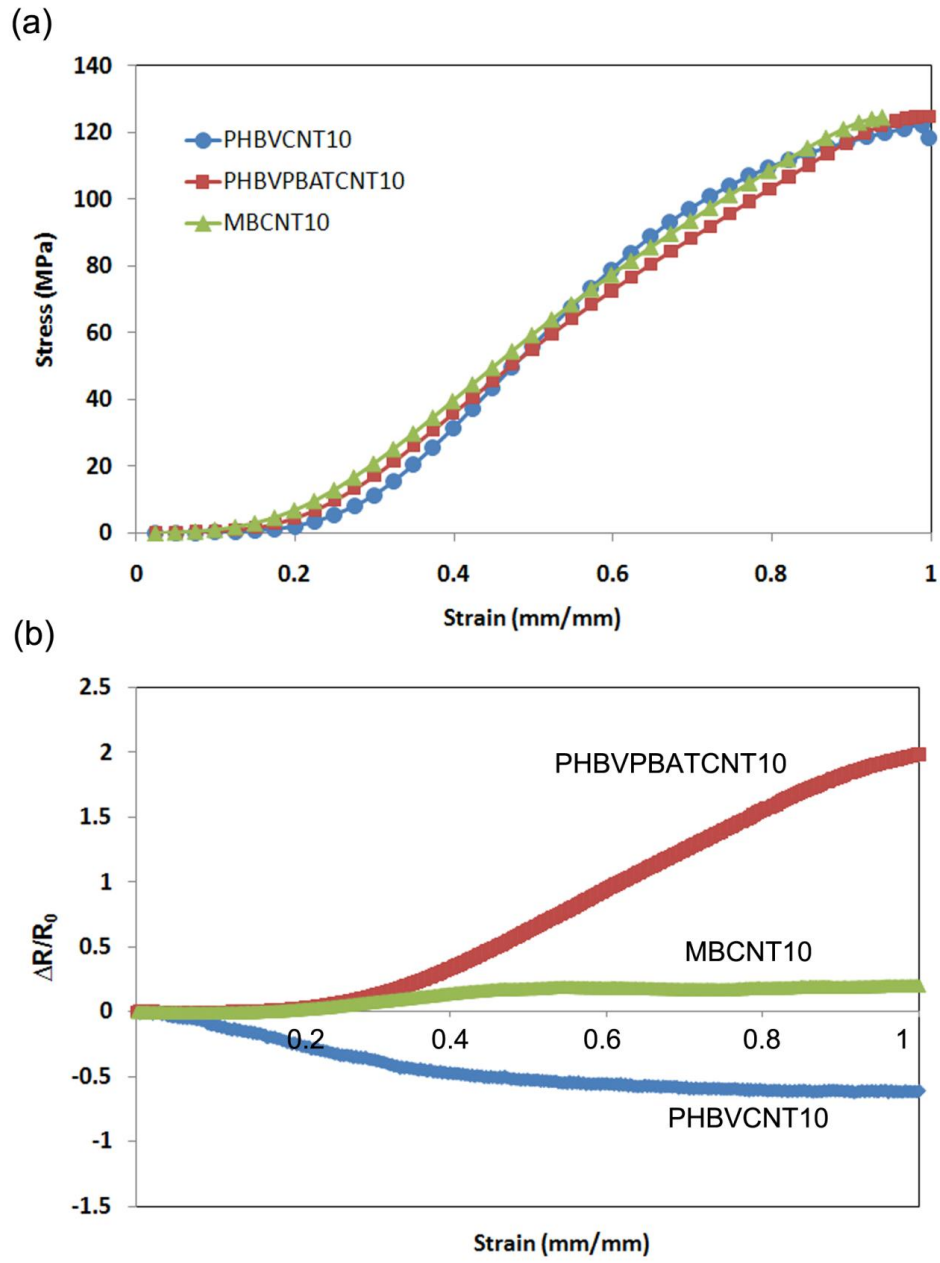

Figure 8.1 (a) Stress strain curves of compositions under compression, (b) electrical response under the same mechanical force.

8.3.2 Resistance Response for Creep and Relaxation

Transient tests were performed using the method of Fotheringham and Cherry [12] which involves stressing a sample and then immediately removing the applied stress and allowing the sample to relax at zero stress. The initial stress ramp up rate of 5MPa per min was used to apply predetermined 32 MPa constant stress on the sample. Once the stress reached to 32 MPa, the load was kept constant for 1 hour. The strain was monitored for 1 h during the period of constant load application (creep segment), as well as for an hour after the release of the constant load (recovery segment). Creep compliance was calculated by dividing the obtained strain values by a constant stress. All tests were performed at an ambient temperature. Figure 8.2 shows the effect of sample composition on creep compliance. It can be clearly seen that the presence of the PBAT phase in PHBV/CNT matrix transforms a conductive composite into a resistive composition. The observed creep resistance increased for the composition prepared by mixing all components together. The composition prepared by the masterbatch approach showed lower creep resistance. In all the cases, both conductive and resistive electrical response under creep remained constant. During recovery following creep, when all stress is removed, a sudden increase in resistance was observed. This corresponds to the instantaneous response of the polymer. Dimensional recovery resulted in an increased resistance. With time, polymer recovery led to a gradual relaxation of the polymer matrix, causing a decrease in resistivity as the material approached the architecture that was present before the application of stress.

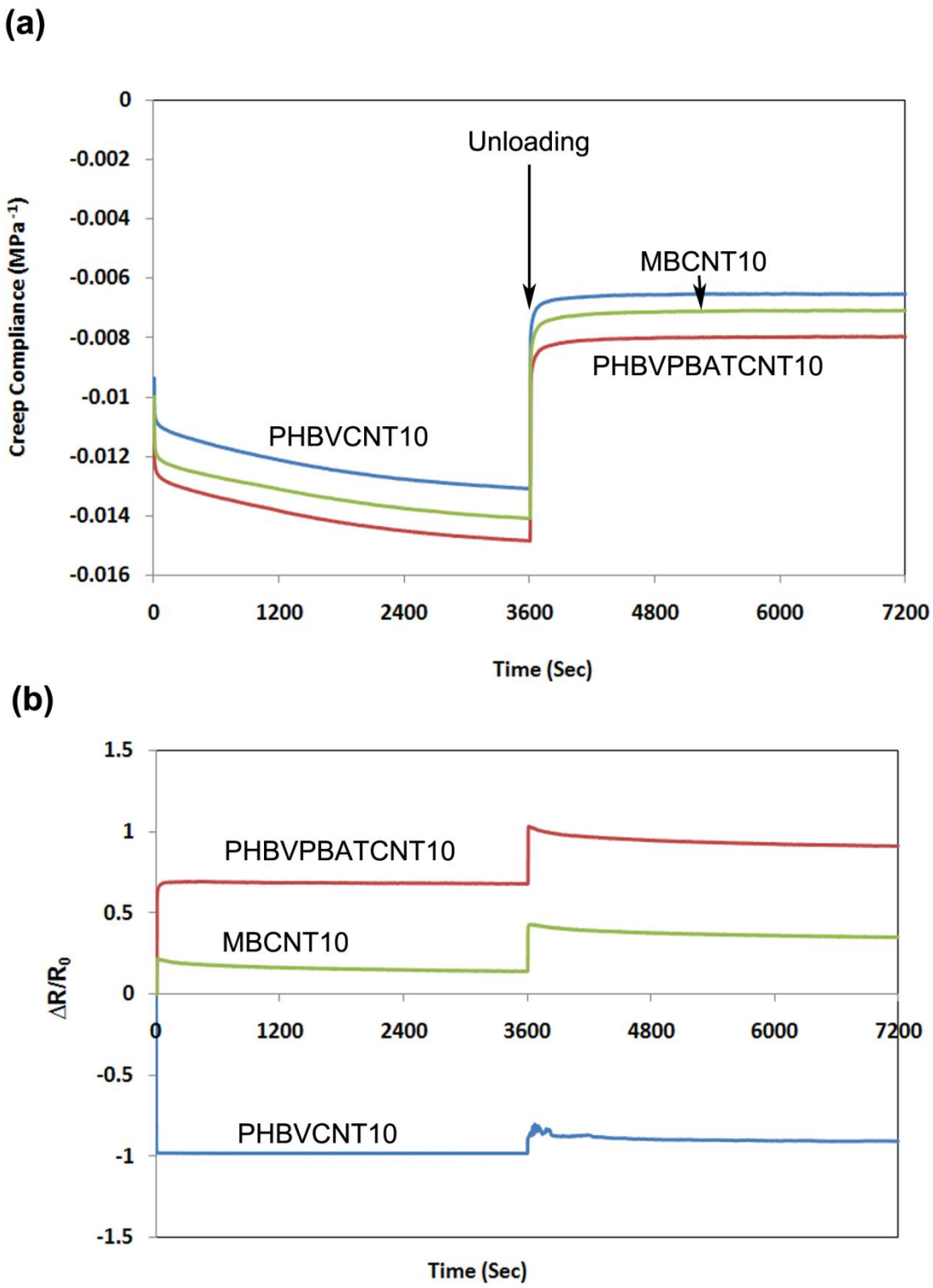

Figure 8.2 Time dependent (a) creep compliance and (b) simultaneously measured resistance response.

8.3.3 SEM

SEM images (Figure 8.3) helped to explain the electrical behavior of these compositions. It can be seen that in PHBVCNT10, nanotubes were well dispersed which helped to the composition to conduct electrons effectively. However, addition of PBAT increased the distance between conductive domains. In MBCNT10 composition PBAT phase is well dispersed and resulted in lower resistance than PHBVPBATCNT10. The selective dispersion of MWCNTs in the PHBV matrix can be observed from the SEM images.

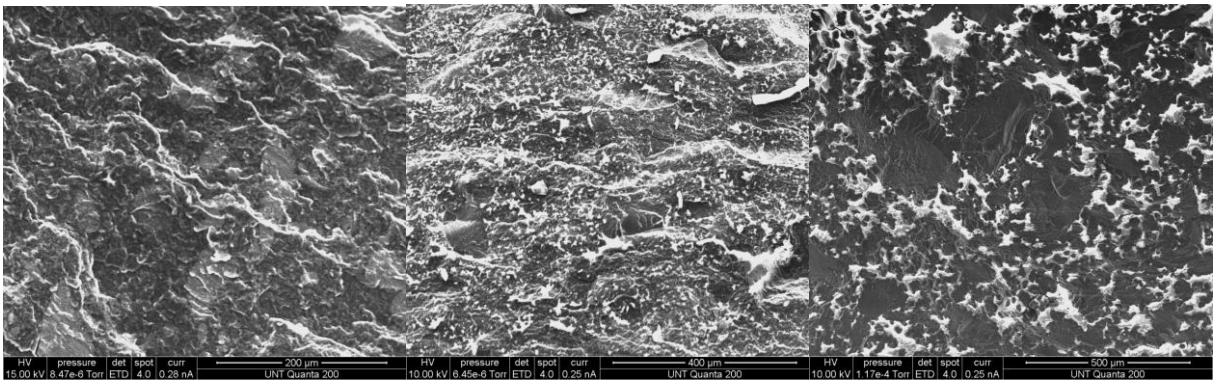

(a) (b) (c)

Figure 8.3 Scanning electron microscopy of fractured (a) PHBVCNT10 (b) MBCNT10 (c) PHBVPBATCNT10

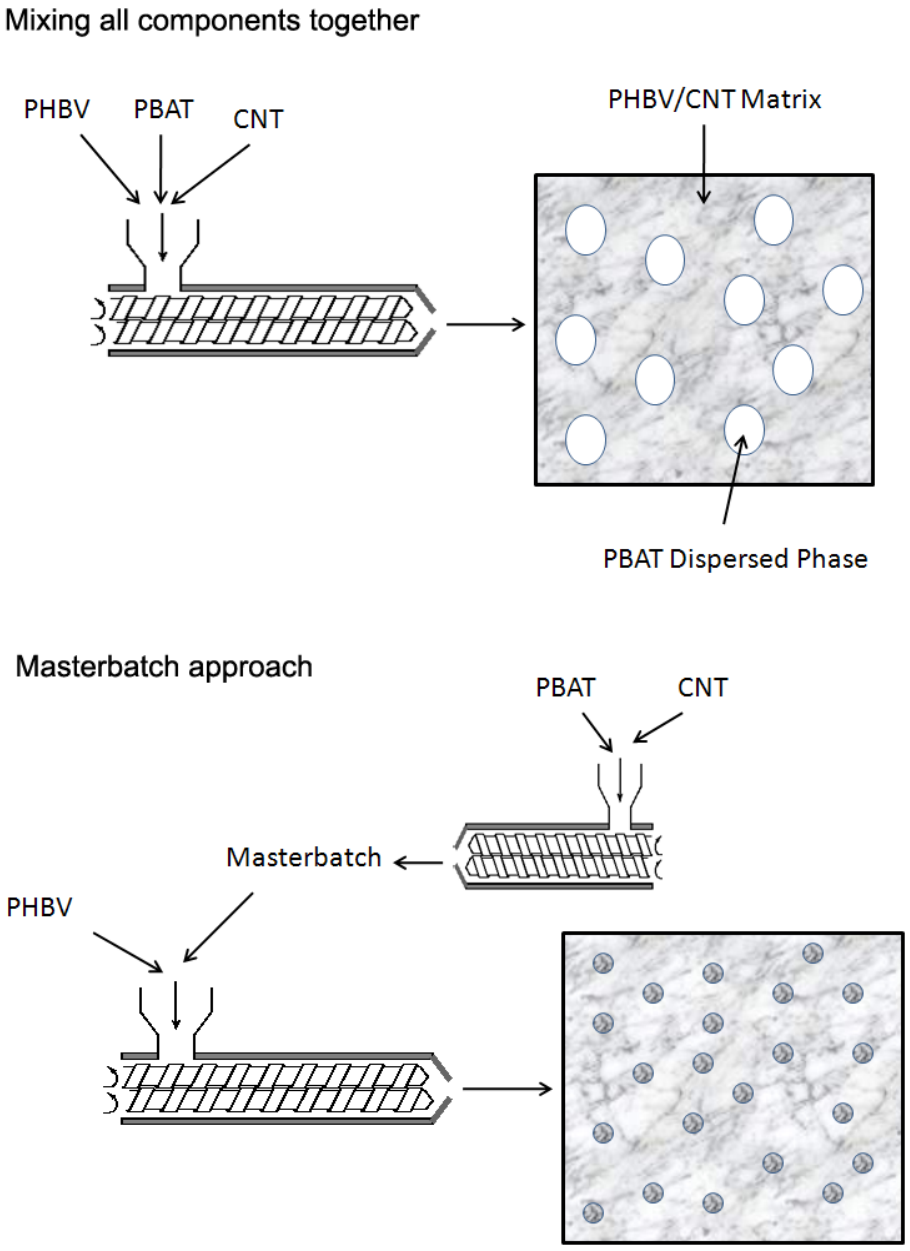

Figure 8.4 Schematic showing two approaches of processing and resultant morphology of CNT filled PHBV/PBAT blend.

8.4 Conclusion

The mechanical properties of the compositions were affected by the single stage or sequential addition of MWCNTs and PBAT components. Compressive yield values did not change significantly but modulus variations were a function of process method. PHBVCNT10 showed the highest modulus and highest electrical conductivity which is evident from the well dispersed CNTs in PHBV matrix. The presence of PBAT phase caused increased CNT-CNT distance and the electrical resistance increase for PHBVPBATCNT10 and MBCNT10 compositions. Overall it was observed that CNT has more affinity towards PHBV and dispersed well in PHBV phase (Figure 8.4). The creep response also showed the effect of selective dispersion of CNT in PHBV phase which resulted in highest electrical resistance response of PHBVPBATCNT10 composition in quasi-static compressive as well as time dependent creep tests. Thus, from the results it can be concluded that by selecting the particular composition and melt compounding approach the electrical response of the material can be controlled.

8.5 References

[1] Vipulanandan C, Garas V. J. of Materials in Civil Engg. 2008;20:93-101.

[2] Ponomarenko A, Shevchenko V, Klason C, Pristupa A. Smart Mater Struct. 1994;3:409-15.

[3] Suhr J, Koratkar N, Keblinski P, Ajayan P. Nature Materials 2005;4:134-37.

[4] Veedu V, Cao A, Li X, Ma K, Soldano C, Kar S, Ajayan P. Nat. Mater.2006;5:457-62.

[5] Xia H, Wang Q. Chem. Mater. 2002;14:2158-65.

[6] Bose S, Bhattacharyya AR, Kodgire PV, Misra A. Polymer 2007, 48, 356.

[7] Dang Z, Wu J, Xu H, Yao S, Jiang M, Bai J. Applied Phy. Lett. 2007;91:0729121-3.

[8] Kim J, Loh K, Lynch J. Proceedings of SPIE –15th Annual International Symposium on Smart Structures and Materials 2008;693232-1.

[9] Laxminarayan K, Jalili N. Text. Res. J. 2005;75:670-80.

[10] Owens F, Jayakody J, Greenbaum S. Composites Sci. and Tech. 2006;66:1280-84.

[11] Kang I, Schulz M, Kim J, Shanov V, Shi D. Smart Mater. Struct. 2006;15:737-48.

[12] Fotheringham, D. & Cherry, B. Comment on the compression yield behaviour of polymethyl methacrylate over a wide range of temperatures and strain-rates. Mater. Sci. Lett. 11, 1368–1371 (1976).

CHAPTER 9

EFFECT OF POLY (BUTYLENE ADIPATE-CO-TEREPHTHALATE), CARBON NANOTUBES ADDITION ON AEROBIC BIODEGRADABILITY BEHAVIOR OF POLY (HYDROXYBUTYRATE-*CO*--HYDROXYVALERATE) IN A LABORATORY AUTOMATED MULTI-UNIT COMPOSTING SYSTEM

9.1 Introduction

Growing awareness about environmental hazards of non-biodegradable polymers has led to the development of biodegradable polymers. Biodegradable polymers can be composted with organic wastes and returned to enrich soil. Biodegradable polymers will also help to reduce environmental pollution, adverse effects on animals, and fertile land. It will also reduce the cost of recycling, labor cost of plastic separation, etc. These bioplastics can also be recycled to useful monomers by enzymatic and microbial treatment [1].

Bioplastics must be designed to meet the requirements of usage and should be able to degrade easily after their valuable use [2]. The study of biodegradation of biopolymers is a vital need in order to expand their use and for clear understanding of their life cycle. For a biodegradation study of polymers, composting has been recognized as one of the most valuable method because it is the most environmentally friendly, and a recommended method for treating organic solid wastes [3, 4].

To evaluate the biodegradation of polymers standard methods like American Standardization for Testing and Materials (ASTM); and International Organization for Standardization (ISO) are used [5, 6]. These tests measure the carbon dioxide, water and other gases released through bio-oxidation of organic materials. The quantity of

CO_2 can be measured and considered as a measure of biodegradation. The composting of the biopolymers takes place under specified conditions of soil pH, moisture, oxygen, and temperature. The carbon dioxide produced during the composting is related to the total carbon content of the material. According to ASTM D-5338-98 (2003) standard even supply of oxygen into the bioreactors is required during composting [7]. The released CO_2 from the reactors can be measured either by using CO2 trapping equipment and titration method or gas flow meter and CO_2 analyzer.

Our group at University of North Texas has developed a multi-unit composting system following requirements of of ASTM D-53338-98 (2003). In this work, biodegradation PHBV, PHBV/PBAT blend composition and CNT filled PHBV/PBAT blend has been done using this unit. To measure the concentration of CO_2 in the outlet gas of each bioreactor, a nondispersive infrared (NDIR) gas analyzer was integrated into the system. The detailed description of the composting unit is given in this chapter. The results showed the comparison of degradation among the individual polymer material, blend, and CNT filled composition.

9.2 Experimental [10]

9.2.1 Materials

Three compositions were used for the degradation investigation. They were 1) PHBV, 2) PHBV/PBAT blend (70:30 wt ratio), and 3) 10 wt% CNT filled PHBV/PBAT (70:30) blend. The melt blended compositions were ground into fine powder before using. The material details and blending method is described in chapter 2 and 3 res. The physical, thermal, and mechanical properties of the biopolymer and its nanocomposite samples are discussed in chapter 3, sections 3.3.1 to 3.3.5. The carbon

content of the compositions was determined by CHN elemental analysis (Elemental Analysis Inc., Lexington, KY). The samples were ground into fine powder before using for degradation test.

9.3 Automated Multi-unit Composting System (AMUCS)

The composting system is designed according to ASTM D-5338-98 (2003) standard [7]. The block diagram and actual picture of this composting unit is shown in Figure 9.1 and Figure 9.2 respectively. This ASTM standard allows twelve composting bioreactors in the system. The AMUCS unit is divided into three subsystems which are 1) water bath system (WBS), 2) the gas distribution system (GDS), and 3) the hardware control and data acquisition system (HCDAQS).

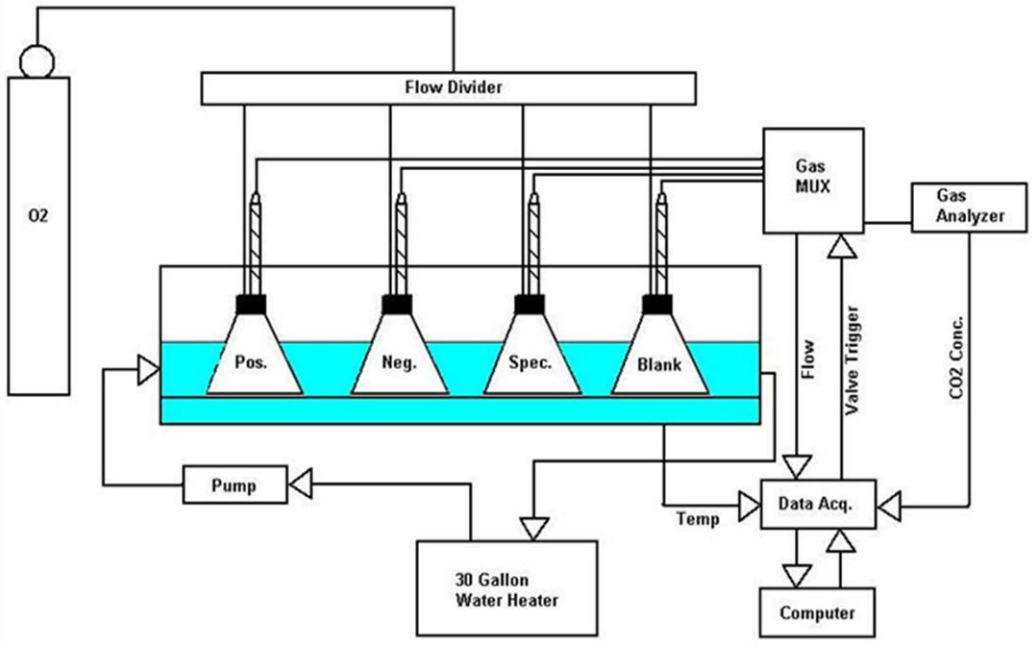

Figure 9.1 Block diagram of the automated multi-unit composting system (AMUCS).

Figure 9.2 Actual picture of the automated multi-unit composting system (AMUCS).

Water Bath System (WBS)

Composting bioreactors are held in WBS. The bioreactors are required to keep at incubation temperature range of 58ºC (±2 ºC) for the entire duration of the composting experiment. This temperature provides suitable temperature for growth and reproduction of thermophilic microbes. The WBS is made up of acrylic sheets with 30 gallon water capacity. WBS contains water heater, transfer pump and three resistance temperature detectors (RTD's).

In composting system twelve Erlenmeyer flasks of 500 ml capacity were used as bioreactors. The fish tank is used as a water bath to hold twelve composting bioreactors which are. They were wrapped in foam duct board and placed inside of a stainless steel box. This helps to maintain the water temperature more efficiently during the experiment and provides safety and structural integrity.

A water heater is used as a heating source due to its large heating capacity and relatively low cost compared to water temperature controllers on the market. Most water

heaters are advertised to have a maximum temperature of approximately 65.5°C, which exceeds the temperature requirements of the ASTM 5338-98(2003) standard. Resistance temperature detectors or RTDs are placed in the water bath to measure the average temperature and are monitored with the hardware control and data acquisition system (HCDAQS).

The transfer pump is also monitored by HCDAQS and is used to pump water from the water heater into the water tank as follows: during composting experiments HCDAQS triggers the transfer pump to circulate water through the water tank and the water heater to maintain the required composting incubation temperature.

Gas distribution System (GDS)

The GDS system is required to keep supply of oxygen to the microorganisms and to measure CO_2 release through degradation process. ASTM standard specifies to maintain O_2 supply evenly to all composting bioreactors. The GDS system is connected to CO2 analyzer which measures the quantity of released CO_2. GDS is designed to supply compressed air to the twelve composting bioreactors at a defined rate via a flow divider shown in Figure 9.3. The flow divider consists of a nylon manifold that splits the compressed air into twelve inlet channels (one for each composting bioreactor). A dial flow controller is placed on each inlet channel to control and verify that each composting bioreactor is receiving the same volumetric flow rate of compressed air.

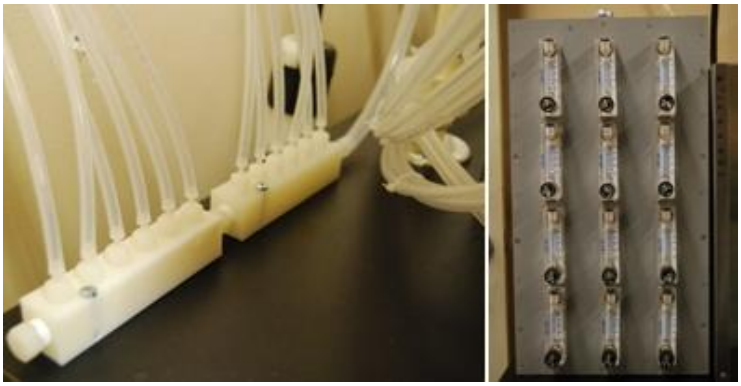

Figure 9.3 Nylon manifold (left) and flow controller (right).

Each inlet channel is connected to a composting bioreactor through a stainless steel tube that passes through a rubber stopper sealing the bioreactor to the bottom of the bioreactor. This to ensure that the compost is thoroughly aerated from the bottom as displayed in Figure 9.4. The inlet compressed air passes through the flow controller to the bottom of each bioreactor by the means of fully enclosed, air-tight inlet channel, stainless steel tube and bioreactor.

Figure 9.4 Composting bioreactor showing the inlet channel connected to a stainless steel tube.

An outlet, an air-cooled Graham condenser, is placed on the top of each composting bioreactor as indicated in Figure 9.5. In addition to being an outlet, the

condenser is used to remove the water vapor from the outlet gas released from each bioreactor. It causes the water vapor to condense and drain back into the composting bioreactor. Each condenser is connected to a gas multiplexer to form an outlet channel. Figure 6.6 shows the picture of the gas multiplexer. Indeed, in order to sample all twelve outlet channels with a single CO_2 gas analyzer, a multiport valve or gas multiplexer is designed so that each of the twelve outlet channels (of each composting bioreactor) can be sampled by the CO_2 gas analyzer individually.

To construct the gas multiplexer, twelve three-way solenoid valves, twelve check valves and a nylon manifold are used to reduce the twelve outlet channels down to one sample channel. The sample channel is then connected to a mass flow meter and a NDIR gas analyzer as shown in the Figure 9.6. The outlet gas released by each bioreactor passes through each condenser into the gas multiplexer by the means of fully enclosed, air-tight condenser, outlet channel and gas multiplexer.

Figure 9.5 Composting bioreactor showing the air-cooled Graham condenser.

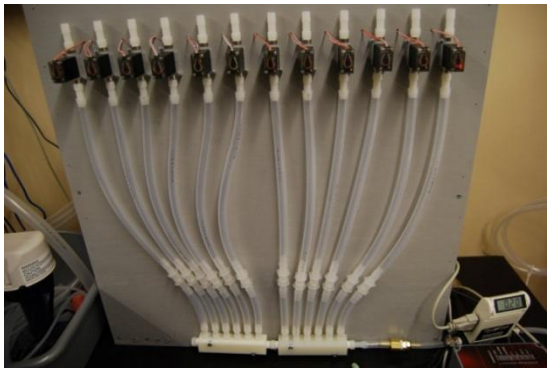

Figure 9.6 Gas multiplexer showing 3-way solenoid valves, check valves and nylon manifolds.

After the outlet gas (released by each composting bioreactor) is dehydrated by the condenser, its flow rate is measured using a Sierra-820 mass flow meter (Sierra Instruments, Inc.: CA, USA) and the CO_2 concentration within the outlet gas is sampled by the Li-COR 820 CO_2 NDIR gas analyzer (Li-COR Biosciences, Inc.: NE, USA). Figure 6.7 shows a picture of the mass flow meter and the CO_2 gas analyzer.

Figure 9.7 Mass flow meter and gas analyzer.

The three-way solenoid valves are sequenced using LabVIEW 8.6 software to pass the outlet gas of only one of the composting bioreactors to the mass flow meter and CO_2 NDIR gas analyzer at a time. After a solenoid valve is activated to be measured, the outlet gas flows through a check valve. This latter then leads the outlet gas to the mass flow meter and the CO_2 NDIR gas analyzer for measurements. Check valves allow the outlet gas to flow only in one direction and are placed between the solenoid valve and the nylon manifold (Figure 9.6). Non-activated solenoid valves exhaust their outlet channel's contents. The activation of the solenoid valves and the measurement of the outlet gas are operated using a cyclic procedure and Table 9.1 illustrates the first four steps in the valve cycling.

Table 9.1 Representative first four steps in the valve sequence

Valve #	**Step 1**	**Step 2**	**Step 3**	**Step 4**
	Status	**Status**	**Status**	**Status**
1	**Sampling**	Exhausting	Exhausting	Exhausting
2	Exhausting	**Sampling**	Exhausting	Exhausting
3	Exhausting	Exhausting	**Sampling**	Exhausting
4	Exhausting	Exhausting	Exhausting	**Sampling**
5	Exhausting	Exhausting	Exhausting	Exhausting
6	Exhausting	Exhausting	Exhausting	Exhausting
7	Exhausting	Exhausting	Exhausting	Exhausting
8	Exhausting	Exhausting	Exhausting	Exhausting
9	Exhausting	Exhausting	Exhausting	Exhausting
10	Exhausting	Exhausting	Exhausting	Exhausting
11	Exhausting	Exhausting	Exhausting	Exhausting
12	Exhausting	Exhausting	Exhausting	Exhausting

Hardware Control and Data Acquisition System (HCDACQS)

The computer program used in this work was LabVIEW 8.6 of the National Instrument CO. The hardware control and data acquisition system (HCDAQS) is an important component of the composting system. HCDAQS is powered by National

Instruments (NI) LabVIEW 8.6 software and compact data acquisition (cDAQ) hardware to create a user interface. It is in charge of acquiring and logging data from the RTDs, flow meter and gas analyzer as well as controlling the water bath temperature, transfer pump and cycling the solenoid valves. A valve and pump control interface (VPCI) was also used in order to interface the NI hardware with the solenoid valves and transfer pump.

GDS and CO_2 Gas Analyzer Validation

The gas distribution system was checked for gas leaks by use of a soap solution on each connection point. This is achieved by supplying all composting bioreactors with compressed air at a rate of 0.2 standard liters per minute (slpm) and dispensing a small amount of soap solution on each of the approximately 100 connection points on the system.

The Li-COR 820 gas analyzer was also validated. This was performed by flowing research grade oxygen O_2 (<0.1 ppm CO_2) through the gas analyzer for 10 min. The reading of the CO_2 measured on the gas analyzer was consistent with that of the research grade O_2. Once the reading stabilized, it was tared in the Li-COR software to set the zero point. A second validation point was also measured to confirm the accuracy of the CO_2 measurements. This was performed by passing compressed air through the gas analyzer. According to a 2008 study of the National Oceanic and Atmospheric Administration (NOAA), CO_2 measured in atmospheric air consist of approximately 385 ppm or 0.0385% [8]. The compressed air was allowed to flow through the gas analyzer for 10 min and measured an average of 402 ppm CO_2 or 0.0402% CO_2. Comparing this to the NOAA estimation resulted in 4.4% difference. This atmospheric CO_2

measurement was also compared with a study performed by Jayasekara *et al.* [4]. They determined the CO_2 concentration to be 400 ppm or 0.04% which resulted in 0.005% difference. From the above statement, it was concluded that the accuracy of the CO_2 gas analyzer was validated in our case.

Outlet Gas Flow Rate Reading and Carbon Dioxide Measurements

When an outlet channel is activated, its content first flows through the mass flow meter which measures the volumetric flow rate in standard liters per minute (slpm). The mass flow meter has two functions. First, it verifies and confirms that each composting bioreactor is supplied the same flow rate of compressed air. Second, for a composted material the flow rate is used to calculate the weight of carbon (CO_2-C) lost in grams.

After exiting the mass flow meter, the outlet channel content passes into the measurement chamber of the Li-COR 820 CO_2 gas analyzer where its CO_2 concentration is measured. This gas analyzer was chosen for the following reasons. It is inexpensive and does not require a carrier gas or external pump to pull the outlet channel gas into the sampling chamber to be measured as in the case of gas chromatographs. In addition, it does not require that a reference gas be added to the outlet channel content to increase the accuracy and precision of the CO_2 concentration measurement. Finally, Li-COR 820 reads the real-time CO_2 concentration as the gas is flowing through the measurement chamber. The CO_2 measurement range within this gas analyzer is 0-2000 ppm.

After an outlet channel is activated to be measured, its content flows first through the mass flow meter and the CO_2 gas analyzer for 1 min to flush both devices. Then, the reading of the volumetric flow rate of the channel content and the measurement of

the CO_2 within this channel content were recorded after the stabilization of the content flow for another 1 min.

For Li-COR 820 CO_2 gas analyzer, the mechanism of measuring the CO_2 is explained here after [9]. This gas analyzer is a single beam, dual wavelength NDIR sensor. The CO_2 measurement is a function of the absorption of IR energy as it travels through the optical path (shown in Figure 9.8). The IR source emits radiation into the optical path, where CO_2 absorbs photons of a certain wavelength. The CO_2 sampling channel uses an optical filter centered at 4.26 μm, corresponding to the absorption band for CO_2, while the reference channel uses a nonabsorbing band at 3.95 μm. A pyroelectric detector measures the absorption of the infrared beam passing through the optical path. The ratio of the sample and reference signals indicates the amount of light absorption by CO_2, and thus, the gas concentration. A heating element placed underneath the pyroelectric terminal regulates the detector temperature precisely at 50ºC so that the detector can determine the thermal gradient noise absorbed from the 4.24 μm band.

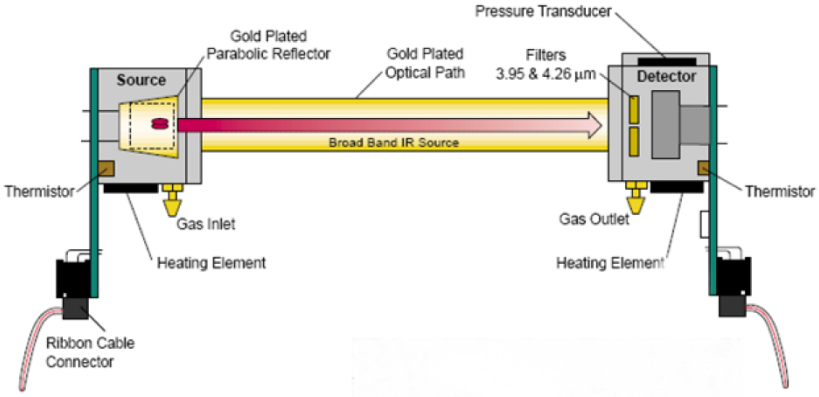

Figure 9.8 Optical path of the Li-COR NDIR CO_2 gas analyzer. Reproduced from Li-COR Biosciences-Li-820 CO2 Gas Analyzer Instruction Manual 2002 (Lincoln, NE).

The CO_2 concentration in the outlet channel content is obtained in part per million (ppm) using Equation 1. C is the CO_2 concentration in ppm, f_c is a 6^{th} ordered CO_2 calibration polynomial, α_c is the CO_2 absorptance, $g_c(\alpha_c, P)$ is the pressure correction, T is the temperature (ºC) of the sample gas and T_o is the temperature of the pyroelectric detector which is 50ºC [9].

$$C = 10 f_c(\alpha_c g_c(\alpha_c, P))(\frac{T+273}{T_0+273}) \quad (9.1)$$

9.3.1 Calculations

Degradation of materials is measured by calculating the amount of carbon or (CO_2-C) released. After C (Equation 9.1) is measured by the CO_2 gas analyzer, it is acquired and logged along with the outlet channel content flow rate obtained using National Instruments data acquisition hardware and LabVIEW 8.6. The mass flow meter and CO_2 gas analyzer data were obtained in slpm, and in ppm, respectively. These two units are used to calculate the total CO_2 (in g) metabolized by the materials using variants of the ideal gas laws and the methodology described here after.

First, the hourly flow rate or F_{Hourly} (l/hr) of the outlet channel content for each bioreactor is calculated. This is achieved by multiplying the flow rate F (l/min) obtained using the mass flow meter by (60 min/1 hr) to convert the flow rate to l/hr as shown by Equation 9.2.

$$F_{Hourly} = F\left(\frac{l}{\min}\right) \times \left(\frac{60\min}{1hr}\right) \quad (9.2)$$

The next step is to correct the CO_2 concentration or $CO_{2(meas)}$ of the outlet channel content for each bioreactor. The corrected CO_2 measurement denoted as $CO_{2\ (corr)}$ is achieved by subtracting the CO_2 present in the compressed air or $CO_{2\ (CA)}$ from the $CO_{2(meas)}$ as shown by Equation 9.3.

$$CO_{2(Corr)}(ppm) = CO_{2(meas)} - CO_{2(CA)} \tag{9.3}$$

$CO_{2\ (corr)}$ is then used to determine the weight of CO_2 per sampled liter of gas or CO_2 (g/l) by taking the product of the $CO_{2\ (corr)}$ and the ratio of the molecular weight of CO_2 or MW_{CO2} (44g/mol) to the molar volume of a perfect gas or MV_{PG} (22.414 L/mol at room temperature T_0=273.15 K and pressure P_0=1 atm). This obtained product is corrected by the ratio of the experimental temperature T_{Exp} to T_0 as shown by Equation 9.4.

$$CO_2(\frac{g}{l}) = CO_{2(Corr)}\left[\left(\frac{MW_{CO_2}}{MV_{PG}}\right)\times\left(\frac{T_0}{T_{Exp}}\right)\right] \tag{9.4}$$

The previous equation determined the CO_2 (g/l). However, biodegradation of materials is determined only by the carbon weight or (CO_2-C) (g/l) metabolized during the composting process. To negate the weight of the oxygen atoms, CO_2 (g/l) is multiplied by the ratio of carbon weight (12 $gmol^{-1}$) to the molecular weight of CO_2 (44 $gmol^{-1}$) as shown by Equation 9.5.

$$(CO_2 - C)\left(\frac{g}{l}\right) = CO_2\left(\frac{g}{l}\right)\times\left(\frac{12}{44}\right) \tag{9.5}$$

After calculating (CO_2-C) (g/l), the gross (CO_2-C) (g) metabolized from the degradation of material is determined by taking the product of (CO_2-C) (g/l), the hourly flow rate, and the time elapsed in hours since the last measurement as shown in Equation 9.6. For our

experiment, CO_2 measurements were recorded every 8 h. We then recorded 3 measurements per day.

$$(CO_2 - C)_{Gross}(g) = (CO_2 - C)\left(\frac{g}{l}\right) \times F_{Hourly} \times \Delta T_{Hour} \tag{9.6}$$

As mentioned earlier, only (CO_2-C) weight obtained during the degradation of the material samples is needed to calculate the percent biodegradation or mineralization. So, the (CO_2-C) weight metabolized by the compost medium needs to be negated from the $(CO_2\text{-}C)_{Gross}$. This is achieved by subtracting the average (CO_2-C) value of the compost medium of the blank bioreactors (containing only compost) from the $(CO_2\text{-}C)_{Gross}$ measurement of the material sample obtained using Equation 6 to obtain the average net (CO_2-C) or $(CO_2\text{-}C)_{net}$ as shown by Equation 9.7.

$$(CO_2 - C)_{net}(g) = (CO_2 - C)_{Gross} - (CO_2 - C)_{Compost} \tag{9.7}$$

$(CO_2\text{-}C)_{net}$ is then added together to determine the cumulative weight (CO_2-C) released or $(CO_2\text{-}C)_{Cum}$ over the entire duration n of the test as shown by Equation 9.8.

$$(CO_2 - C)_{Cum}(g) = \sum_{n=0}^{n}(CO_2 - C)_{net} \tag{9.8}$$

Once the $(CO_2\text{-}C)_{Cum}$ is calculated, the percent biodegradation or % biodegradation can be determined. To calculate the % biodegradation, the carbon content or %C of the material samples must be used. This can be obtained by conducting CHN elemental analysis. The total carbon content weight (C_{Tot}) can be obtained by taking the product of the %C and the original weight or m (in grams) of the material sample used for the composting experiment. The % biodegradation is obtained by dividing $(CO_2\text{-}C)_{Cum}$ by C_{Tot} and multiplying the result by 100% as shown in Equation 9.9.

$$\%\,Bio\,\deg radation = \left(\frac{(CO_2 - C)_{Cum}}{C_{Tot}}\right) \times 100\% \tag{9.9}$$

9.3.2 Compost Medium and its Characterization

A compost medium was purchased from Collin County Municipal Waste Facility (TX, USA) and is made of food waste and yard trimming including grasses, leaves, and sticks. The compost was ground and sieved on a screen of 10 mm to prepare homogenous sample.

The moisture content of the compost was determined following ASTM D 2974 Test Methods. Compost sample of 25 g was dried in an oven at 105ºC until constant weight was obtained. The measurements were conducted in triplicate and the moisture content result obtained was 56.49% (±1.5).

The procedure for the determination of total solids (TS) and volatile solids (VS) is described here after. First, compost sample of 25 g was dried in an oven at 105ºC overnight to obtain the % TS. The dried sample was then heated in a furnace at 550ºC for 1 h to obtain the % VS. The measurements were conducted in triplicate and the %TS and %VS were 43.51 (±1.5) and 20.60 (±1.5), respectively.

The pH of the compost was determined with an Oakton Acorn® pH 6 Meter. The measurements were done in triplicate on 5 g compost samples in 25 mL distilled water after homogenization for 5 min at room temperature. The pH result obtained was 8.81 (±0.3) which is above 7.

Carbon (16.13%) and nitrogen (0.71%) contents of the compost medium were determined by CHN elemental analysis (Elemental Analysis Inc., Lexington, KY). The ratio of C/N is 22.72 which is within the recommended range of 10-40.

9.3.3 Composting Procedure

The biodegradability test by composting using AMUCS was conducted on the basis of ASTM D 5338- 98 (2003) standard [7]. This test method determines the degree and rate of aerobic biodegradation of plastic materials on exposure to a controlled-composting environment under laboratory conditions.

200 g of homogenized compost was weighed into each glass bioreactor vessel and mixed with up 2 g of the biopolymer, blend, and its nanocomposite samples, and 4 g of microcrystalline cellulose. Three blank bioreactors were included in the biodegradation testing system. Each of them contained only 200 g of the compost medium without testing material. After mixing, all the bioreactors were weighted and incubated under optimal oxygen, temperature and moisture conditions for a test period of 45 days. The compressed air flows were regulated to the amount of 0.2 standard liters per minute (slpm) throughout the experiment to ensure enough oxygen for the biodegradation process. The temperature and moisture content were kept at 56.3ºC and 56.5%, respectively. The biodegradation of the testing materials, microcrystalline cellulose and the compost medium was done in triplicate.

The water content in the bioreactors was controlled every 4 days to adjust the moisture level to 56.5%. This is accomplished by first stopping the experiment and weighing each bioreactor to record its weight loss. Then distilled water of approximately 20 cm^3 corresponding to the amount of weight loss was added to each bioreactor contents to restore the initial weight. The contents were then mixed homogenously using a spatula.

9.4 Results and Discussion

Quality of the Compost Medium and Validation of the Composting Test Conditions

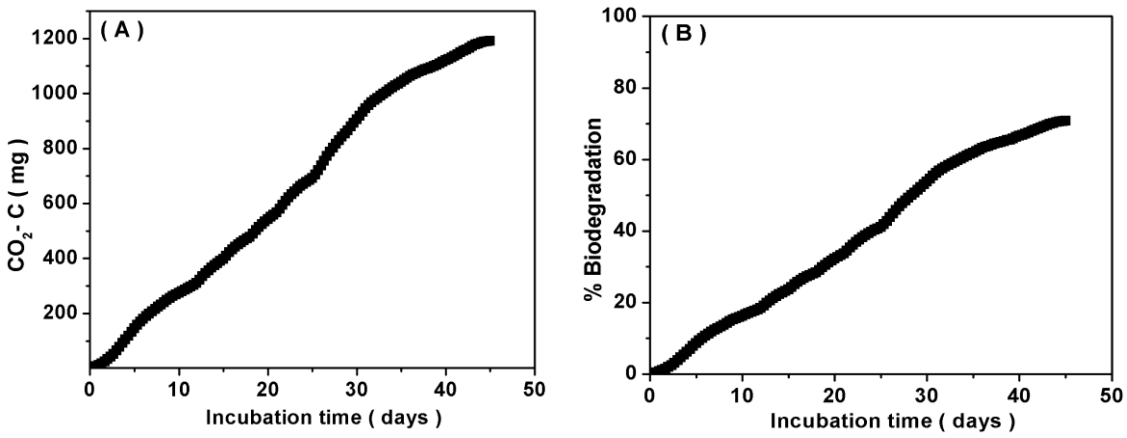

Figure 9.9 Net cumulative CO_2-C productions (A) and percentage biodegradation (B) of cellulose. [10]

To assess the quality of compost medium biodegradation of the cellulose was taken as a reference. According to ISO 14855, cellulose should undergo more than 70% degradation in 45 days in the composting condition which is to be used for testing. Figure 9.9(A) and (B) show the net cumulative carbon dioxide (CO_2-C) productions and the percentage mineralization of the microcrystalline cellulose, respectively. The obtained results indicated that the degree of biodegradation of the cellulose material was 72.05% in the compost medium after 45 days at 56.3ºC.

Biodegradation Behavior of PHBV, PHBV/PBAT, and CNT filled PHBV/PBAT

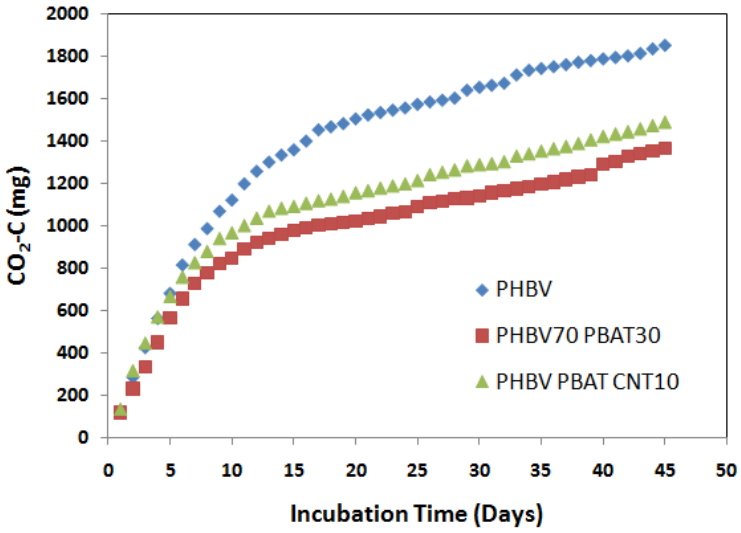

(a)

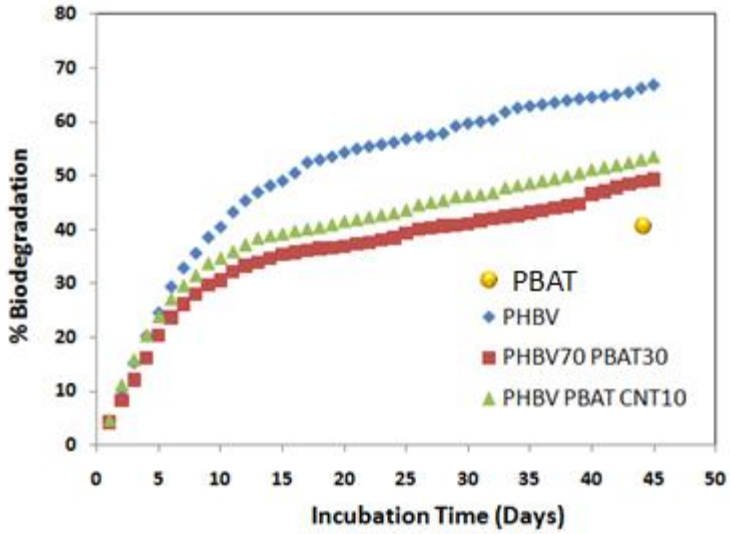

(b)

Figure 9.10 Net cumulative (CO_2-C) productions (A) and percentage biodegradation (B) of PHBV, PHBV/PBAT, and CNT filled PHBV/PBAT and PBAT.

The degradation rate of synthetic PBAT is far less than the natural PHBV. Kijchavengkul et al. [11] observed that PBAT degradation rate in compost is around 40% in 45 days. CO2 metabolized during the composting test is the measure of biodegradation of material. The net cumulative CO2-C production and % biodegradation

of above sample materials are shown in Fig. 9.10 (a) and (b), respectively. With initial lag of ~36 hrs, mineralization of all the samples increased rapidly till day 13. The rate of degradation decreased continuously after day 13. The degradation of all the samples seems continuous as no plateau was reached. The degradation rate of PHBV was faster than blend and CNT filled blend samples. The addition of PBAT significantly reduced the degradation rate of PHBV. However, CNT filled PHBV/PBAT system showed higher degradation rate than that of the PHBV/PBAT blend. In a previous study, it was inferred that addition of CNT in PHBV/PBAT system caused reduced domain size of the PBAT dispersed phase. So increased surface area of PBAT increased the degradation rate in CNT filled PHBV/PBAT composition than only PHBV/PBAT. The above analysis suggested that the overall biodegradability (i.e. rate, degree and ease of degradation) of the biopolymer PHBV was significantly affected by the addition of the PBAT and CNTs.

9.5 Conclusion

The system described in this work was effectively used for the validation of biodegradation study according to ASTM D 5338-98 (2003) with the use of cellulose as a reference material. The system is used to investigate the effect of the addition PBAT and CNTs on the biodegradability behavior of PHBV. The mineralization result suggested that the overall biodegradability (i.e. rate, degree and ease of degradation) of the biopolymer PHBV was significantly affected by the addition of PHBV and CNTs. Indeed, under the same controlled composting test conditions, the incorporation of 10 wt% CNTs into PHBV/PBAT blend matrix yielded composite with significantly improved biodegradability with respect to the PHBV/PBAT system.

9.6 References

[1] Mohanty AK, Misra M, Hinrichsen G. Macromol. Mater. Eng 2000;1(24):276.

[2] Shimao M. Current Opinion in Biotechnology 2001;12(3):242-247.

[3] Lopes WS, Leite VD, Prasad S. Bioresource Technology 2004;94(3):261-266.

[4] Davidssona A, Gruvbergerb C, Christensenc TH, Hansenc TL, Cour J. Jansen Waste Management 2007;27(3):406-414.

[5] Kale G, Auras R, Singh RP, Narayan R. Polymer Testing 2007;26:1049.

[6] Du YL, Cao Y, Lu F, Li F, Cao Y, Wang XL, Wang YZ. Polymer Testing 2008;27:924.

[7] ASTM D 5338-98 (2003), American Society for Testing and Materials standard test method for determining aerobic biodegradation of plastic materials under controlled composting conditions, 2003.

[8] National Oceanic and Atomospheric Administration. Trends in Carbon Dioxide. http://www.esrl.noaa.gov/gmd/ccgg/trends/ (accessed August 17, 2009).

[9] Li-COR Biosciences; Li-820 CO2 Gas Analyzer Instruction Manual; Lincoln, NE: LI-COR, Inc., 2002.

[10] Dagnon Koffi. PhD Dissertation 2009. Chapter 6.

[11] Thitisilp Kijchavengkul T, Auras R, Rubino M, Selke S, Ngouajio M, Fernandez RT. Polymer Degradation and Stability 2010;95:2641-2647.

CHAPTER 10

SUMMARY

The objective of this dissertation was to establish the viability of carbon nanotube dispersed multi-functional, biodegradable PHBV and PHBV/PBAT blend system as piezoresponsive materials for potential use in structural health monitoring.

Effect of CNT Nucleation on PHBV Matrix

Poly(hydroxy butyrate-co-valerate) (PHBV) is a biodegradable polymer which is highly crystalline and difficult to process due to slow crystallization rate, and shows cold crystallization behavior. The above limitations of this bio-polymer were solved by the addition of multi wall carbon nanotubes (MWCNT) by conventional melt blending method. MWCNT acted as nucleating agent for pure PHBV matrix. The increase in recrystallization temperature and rate of nucleation with eliminating cold crystallization temperature resulted from the addition of MWCNT. An increase in crystallite thickness was observed by wide angle X-ray diffraction (WAXD). Transmission electron microscopy showed good dispersion of MWCNTs in PHBV.

Piezoresistive Behavior of MWCNT Filled PHBV Composites

Thermal, mechanical, and electrical properties of PHBV were improved by CNT filler. The piezoresistive behavior of these composites was investigated under transient, quasi-static, and cyclic loading. The effect of CNTs on the gauge factor of PHBV showed values of 6.25 – 8.5 which are significantly higher than PVDF/CNT composite at the same concentration. The long term constant loading on PHBV/CNT composites showed time independent piezoresistive response. When the load was removed the PHBVCNT5 composite had a gradually increasing resistance while the PHBVCNT10

had a time independent recovery. Under cyclic loading condition, the stress–time and resistance–time were synchronous. These results showed that these composites were viable candidates for biomedical and environmental applications.

PHBV/PBAT Blend

In non-isothermal and isothermal crystallization melting study a rare phenomena of melting point elevation was observed when more of PBAT (up to 50 wt. %) was added to the blend. Nishi Wang and Hoffman Weeks equations were used to describe the experimentally observed melting point elevation in binary crystalline/crystalline blends in terms of thermodynamic melting elevation and changes in the lamellar thickness. DSC and SAXS results indicated increased thickness and crystal perfection as the degree of supercooling decreased with the addition of PBAT in PHBV. This resulted in an elevation of melting point of the blends. Thus, by controlling the crystallization kinetics and selecting the proper blend compositions one can control the microstructure and ultimate material properties of the blend. Decreased surface energy in the blend compositions indicated better adhesion between the two phases. Morphological structures of PHBV/PBAT blends were observed by polarized optical microscopy and scanning electron microscopy and correlated to resultant thermo mechanical properties. Concentration dependent mechanical properties were observed for PHBV/PBAT blends.

Rheological Behavior of PHBV/PBAT Blends

Rheological study showed increased viscosity, elastic moduli, and loss moduli with increase in concentration of PBAT. The viscosity of PHBV30, 20, and 10

compositions showed higher viscosity values than the individual components that indicated the miscibility of the two phases at these compositions.

Piezoresistive Behavior of CNT Filled PHBV/PBAT Blend

The presence of PBAT phase caused increased CNT-CNT distance and therefore electrical resistance was increased for PHBVPBATCNT10 and MBCNT10 compositions. The observed gauge factors for PHBVPBATCNT10, and MBCNT10 were 3.75 and 1.5 respectively. SEM results indicated that CNT has more affinity towards PHBV and dispersed well in PHBV phase. Thus, from results it was concluded that by selecting the particular composition and choosing the particular melt compounding approach the electrical response of the material can be controlled.

Biodegradable Multifunctional Approach

The effect of PBAT and CNT on degradation of PHBV was studied. The results indicated PBAT and CNT acted as a controlling factor Summary of overall dissertation is illustrated in following Figure

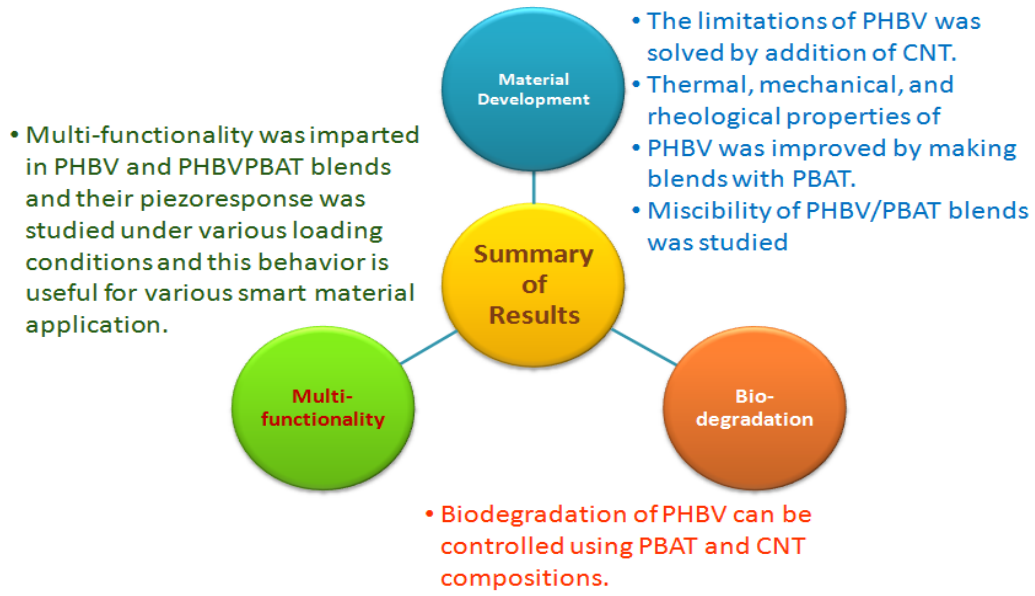

Figure 10.1 Summary